The $^3\mathrm{He}(d,p)^4\mathrm{He}$ Reaction at Low Energies

by

William H. Geist

A dissertation submitted to the faculty of the University of North Carolina at Chapel Hill in partial fulfillment of the requirements for the degree of Doctor of Philosophy in the Department of Physics & Astronomy.

Chapel Hill

1998

Approved:

E. J. Ludwig

E. J. Ludwig, Advisor

H. J. Karwowski

H. J. Karwowski, Reader

W. J. Thompson

W. J. Thompson, Reader

ABSTRACT

WILLIAM H. GEIST: The ^{3}He$(d,p)^4$He Reaction at Low Energies
(Under the Direction of E. J. Ludwig)

Angular distributions of cross sections and complete sets of analyzing powers have been measured for the ^{3}He$(d,p)^4$He reaction at laboratory energies of 60, 99, 199, 424, and 641 keV. Also, an excitation function of the cross section was measured from 245 to 685 keV, along with an absolute determination of the total cross section at 426 keV. These measurements are useful to reveal the mechanism of this surprisingly complex reaction, for use in beam polarimetry measurements, and to provide additional information for an R-matrix analysis of the ^{5}Li system. In the process of obtaining these data, ion-implanted ^{3}He targets were developed, the minitandem accelerator was upgraded, the high-voltage chamber was made operational, and two polarimeters were calibrated for low-energy deuteron beams. The data reveal that both P and D waves are necessary to describe the data and that the P waves are most likely due to a direct process. These measurements are compared to previous measurements, an R-matrix prediction, and the R-matrix parameterization which includes the current data. Also, calculations for the electron-screening potential were performed using a bare-nuclear cross section calculated from the R-matrix parameterization.

ACKNOWLEDGMENTS

Research projects in nuclear physics tend to involve a lot of people because of the complex experimental equipment and the time limits that are placed on the experiments. I was very lucky to be able to work with an enjoyable group of people. The experience and usually sound advice from Professors Ed Ludwig and Hugon Karwowski have added greatly to my graduate education and I am very thankful for that. Also, I am thankful for discussions with Dr. William Thompson about this project.

Many people worked long hours, especially Dr. Ludwig, Dr. Karwowski, and Kevin Veal, on the experimental runs while collecting data. Other people who contributed to this work are Dr. Carl Brune, Mike Wood, Denise Powell, Steve Hale, Dr. Ben Crowe, Dr. Zeid Ayer, Dr. Lijun Ma, Dr. Jeff Blackmon, and Dr. Tim Black. I would like to thank these people for their time, energy, and friendship.

I consider myself lucky to have had the opportunity to work with Dr. Gerry Hale on the R-matrix parameterization. I was treated very nicely by the members of the T2 group during my trip to Los Alamos. I am very thankful for Gerry's efforts on this project both while I was at Los Alamos and after I left.

The initial developmental work on the ion-implanted ^{3}He targets done by Dr. Kurt Fletcher and Andy Hird contributed to my early experimental success.

The success of this work is also partly due to the efforts of the technical staff at TUNL: Paul Carter, Richard O'Quinn, John Dunham, Sidney Edwards, Pat Mulkey, and Robert Timberlake. The long hours that these people put into fixing problems and constructing equipment, often at odd hours, is greatly appreciated.

Last but certainly not least I would like to thank my family and friends who encouraged me throughout my graduate career. I greatly appreciate the support and encouragement from my parents, the friendship and "home away from home" from my sister Christine, and time off spent with my friend Dug.

William H. Geist

July 1998

CONTENTS

LIST OF TABLES

LIST OF FIGURES

Chapter 1

Introduction

The ^{3}He$(d,p)^4$He reaction has been studied[1] for the past few decades. At first look, a description of the reaction would seem trivial because at low energies the reaction proceeds through a known level in ^{5}Li. In this type of reaction mechanism the deuteron and ^{3}He form a compound nucleus in a known excited state in ^{5}Li before decaying into a proton and alpha particle. For a situation like this all the observables are easily calculated [Con84]. The description of observables of this and other similar reactions tend to be much more complicated and they do not follow simple relations. In fact, to describe the reaction one needs to consider higher partial waves that in principle can contribute to the reaction through both a resonant and direct mechanism. The picture of a direct mechanism is that a compound nucleus is not formed but rather nucleon(s) are transferred directly between the projectile and the target nucleus; in this case a neutron is transferred to the ^{3}He.

Understanding the interplay between these mechanisms is an important yet formidable task. For example, nuclear astrophysics can benefit from an understanding of these effects because often the cross section for a reaction needs to be known at very-low energies where measurements in the laboratory are not prac-

[1] A review of the previous work below 1 MeV, both experimental and theoretical, is given in Section 1.2.

tical. To get a value for the cross section, an extrapolation is made from data measured at higher energies. When a resonance is present at low energies, often only properties of this resonance are used in the extrapolation and direct contributions are neglected. Perhaps by understanding the reaction mechanism of the ^{3}He$(d,p)^4$He reaction this can be applied to other reactions of astrophysical significance. Unfortunately, inclusion of a direct mechanism greatly complicates the description of the reaction because there are now many more reaction channels that can interact.

The ^{3}He$(d,p)^4$He reaction is dominated by a broad resonance in ^{5}Li at low energy but values of observables indicate that other reaction channels interfere with this resonance. It is unclear whether these other channels proceed by a resonant process or a direct process or even a combination of both. The ^{3}He$(d,p)^4$He reaction is good case to study the interplay between different reaction processes because it has favorable characteristics, such as a large cross section and easily detected reaction products, which make the measurement of many different types of observables possible. Investigation of the ^{3}He$(d,p)^4$He reaction can also lead to a better understanding of the level structure of ^{5}Li using an R-matrix analysis. This reaction has a very large electron screening effect at energies in the low keV range making it an excellent test case for screening calculations but, only if the bare nuclear cross section is known well. With the R-matrix analysis an extrapolation of the bare nuclear cross section to the energy range of interest can be made.

Precise measurements of the cross section and polarization observables are used in several different types of applications. Knowledge of analyzing powers for this reaction is important for polarimetry while cross-section measurements are used in primordial nucleosynthesis calculations. Also there have been several papers [Dab88, Mil88, Mom88] describing the possibility of a $d-{}^3$He fusion reactor, which has been stimulated by the discovery of large quantities of ^{3}He on the lunar surface.

To study the ^{3}He$(d,p)^4$He reaction, measurements were taken using the Low-Energy Beam Facility (LEBF) at the Triangle Universities Nuclear Laboratory (TUNL). Complete sets of analyzing powers and cross section angular distributions were taken at five energies[2]; 60, 99, 199, 424, and 641 keV. Also, an excitation function was measured over an energy range from 245 to 685 keV and was normalized to an absolute cross section determination at 426 keV.

In this chapter the motivation will be discussed along with a review of the previous experimental and theoretical work. Chapter 2 discusses the developmental work that was necessary for these measurements. In Chapters 3 and 4 the experimental procedure and data analysis are reviewed. The data and results of Legendre function fits are given in Chapter 5. In Chapter 6 the R-matrix calculations are presented and in Chapter 7 is a discussion of the conclusions from this work.

1.1 Motivation

1.1.1 The reaction mechanism

The ^{3}He$(d,p)^4$He reaction is dominated below a deuteron energy of 1 MeV by a $\frac{3}{2}^+$ S-wave resonance in ^{5}Li at $E_d = 430$ keV [Ajz88]. Assuming the reaction proceeds only through the resonance, the analyzing powers follow relationships given by

$$A_y(\theta) = 0 \tag{1.1}$$

$$A_{yy}(\theta) = \frac{1}{2} \tag{1.2}$$

$$A_{xz}(\theta) = -\frac{3}{2}\cos\theta\sin\theta \tag{1.3}$$

$$A_{zz}(\theta) = \frac{1}{2}(1 - 3\cos^2\theta) \tag{1.4}$$

[2]All energies will be given in the laboratory frame unless otherwise noted.

and $\sigma(\theta)$ is isotropic. Previous experiments [Lee71, Gar74] show that these relationships do not hold true even on the resonance. The cross section angular distributions and tensor analyzing power A_{yy} are not isotropic, while the vector analyzing power A_y is non-zero. Measurement of discrepancies between these observables and the resonance relationships, equations 1.1 to 1.4, are useful in determining the reaction mechanism and the validity of the dominant-resonant assumption.

The first suggestion [Bro66, McI67] for the discrepancy between the measured analyzing powers and the resonance relationships is that it is due to an interference of the resonance channel with another S-wave entrance channel. For this reaction there are only two possible S-wave entrance channels, the ${}^4S_{\frac{3}{2}}$ channel corresponding to the resonant contribution, and the ${}^2S_{\frac{1}{2}}$ channel (the notation used for the channel ${}^{2S+1}L_J$ is that S is the coupled channel spin, which is either $\frac{1}{2}$ or $\frac{3}{2}$, L is the orbital angular momentum, and $\vec{J} = \vec{L} + \vec{S}$). With only S waves in the incident channel, the tensor analyzing powers should differ from the resonance relationships only by a scale factor which is dependent on the magnitude of the interference between the two channels and the vector analyzing power should still be zero.

A more realistic approach [Gar74] includes contributions from channels with $L \leq 2$. The higher-order partial waves greatly increase the number of matrix elements from 2 (corresponding to incident S waves) to 13, see Table 1.1. An analysis using this assumption is much more complicated and can be used to derive linear combinations of the matrix elements [Sei70] when complete sets of analyzing powers are measured. Measurements of the analyzing powers used in conjunction with other spin observable measurements, for example, polarization transfer, spin correlation coefficients, etc., can be used to derive values for individual matrix elements. When certain combinations of spin observables are combined, all the matrix elements [Sei70] for this reaction can be uniquely determined.

Matrix elements, M_i			
i	entrance channel	J^π	exit channel
1	${}^4S_{\frac{3}{2}}$	$\frac{3}{2}^+$	${}^2D_{\frac{3}{2}}$
2	${}^2S_{\frac{1}{2}}$	$\frac{1}{2}^+$	${}^2S_{\frac{1}{2}}$
3	${}^2P_{\frac{1}{2}}$	$\frac{1}{2}^-$	${}^2P_{\frac{1}{2}}$
4	${}^2P_{\frac{3}{2}}$	$\frac{3}{2}^-$	${}^2P_{\frac{3}{2}}$
5	${}^4P_{\frac{1}{2}}$	$\frac{1}{2}^-$	${}^2P_{\frac{1}{2}}$
6	${}^4P_{\frac{3}{2}}$	$\frac{3}{2}^-$	${}^2P_{\frac{3}{2}}$
7	${}^4P_{\frac{5}{2}}$	$\frac{5}{2}^-$	${}^2F_{\frac{5}{2}}$
8	${}^2D_{\frac{3}{2}}$	$\frac{3}{2}^+$	${}^2D_{\frac{3}{2}}$
9	${}^2D_{\frac{5}{2}}$	$\frac{5}{2}^+$	${}^2D_{\frac{5}{2}}$
10	${}^4D_{\frac{1}{2}}$	$\frac{1}{2}^+$	${}^2S_{\frac{1}{2}}$
11	${}^4D_{\frac{3}{2}}$	$\frac{3}{2}^+$	${}^2D_{\frac{3}{2}}$
12	${}^4D_{\frac{5}{2}}$	$\frac{5}{2}^+$	${}^2D_{\frac{5}{2}}$
13	${}^4D_{\frac{7}{2}}$	$\frac{7}{2}^+$	${}^2G_{\frac{7}{2}}$

Table 1.1: Matrix elements that can contribute to the ${}^3\mathrm{He}(d,p){}^4\mathrm{He}$ reaction for entrance channel angular momentum up to $L = 2$.

Accurate measurements of the analyzing powers can also be used to differentiate between a resonance and a direct mechanism. Evidence for entrance channels which proceed through a direct process interfering with the dominant resonant channel may be obtained from the shape of the angular distributions [San96]. For a low-energy deuteron beam, Santos makes the assumption that partial waves of $L \leq 2$ are involved in the description of the reactions. Under these conditions it is easy to separate the possible transitions into two groups, a positive-parity group and a negative-parity group. The positive-parity group contains the transitions 1, 2, and 8 through 12 from Table 1.1 and include possible resonances with J^π of $\frac{1}{2}^+$, $\frac{3}{2}^+$, and $\frac{5}{2}^+$. The negative-parity group contains elements 3 through 6 and comprises possible resonances with J^π of $\frac{1}{2}^-$ and $\frac{3}{2}^-$. Elements 7 and 13

are omitted because $L > 2$ in the exit channel. Assuming there are no other resonances than the $J^\pi = \frac{3}{2}^+$ resonance in this energy region, then the presence of transitions involving the negative-parity group are evidence for a direct-type process. In this case, the need for odd Legendre functions to fit the data is evidence for these negative-parity-group transitions.

Understanding the reaction mechanism of a case like this is not only an interesting case of fundamental nuclear physics but is important for being able to calculate observables accurately. For example, the ^{6}Li$(d,\alpha)^4$He reaction is dominated at low energies by broad 2^+ resonance in the compound nucleus, ^{8}Be. In this case it was found that both a direct mechanism and a resonant contribution were needed to describe the cross section at low energies [Cze97]. The ^{11}B$(p,\alpha)^8$Be reaction is another case where both resonant and direct processes are used to describe the data [Ang93].

1.1.2 *R*-matrix parameterization of the ^{5}Li system

The *R*-matrix parameterization of the ^{3}He$(d,p)^4$He reaction provides information about the level structure of ^{5}Li. The specific technique and application are discussed in detail in Chapter 6. A global fit is obtained to all measured observables for the various channels in the ^{5}Li system up to a chosen excitation energy in ^{5}Li. The *R*-matrix parameters for each channel are varied to get the best fit to the data and then can be used to predict unknown quantities. Measurement of the analyzing powers and cross sections at low energies should improve the parameterization so that one will get more accurate predictions of low-energy observables.

From the *R*-matrix parameterization a prediction of the bare nuclear cross section can be made at very low energies (< 20 keV) where it is important for electron-screening calculations, as follows. When measuring reactions in the laboratory the target is usually in the form of neutral atoms or molecules. In this case the electrons of the struck atom will screen the positively charged projectile

from feeling the repulsive force from the nucleus in the target. The projectile will effectively see a reduced Coulomb barrier. This will lead to an enhancement of the measured laboratory cross section, $\sigma_{exp}(E)$, than for the bare nuclear, $\sigma_{bn}(E)$, case. The enhancement factor [Ass87] is defined as.

$$f(E) = \frac{\sigma_{exp}(E)}{\sigma_{bn}(E)} \approx exp(\pi\eta(E)U_e/E) \tag{1.5}$$

where U_e is the screening potential, E is the energy in the center-of-mass system, and $\eta(E)$ is the Sommerfeld parameter defined by $2\pi\eta(E) = 2\pi Z_1 Z_2 e^2/\hbar v \approx 31.29 Z_1 Z_2 \sqrt{\mu/E}$ for the initial nuclei with charges Z_1 and Z_2 and reduced mass μ. The screening potential can be approximated by $U_e \approx Z_1 Z_2 e^2/R_a$ where R_a is the atomic radius [Eng88]. The enhancement factor, $f(E)$, tends to unity at high energies and, in this case, the laboratory measurements can be assumed to represent $\sigma_{bn}(E)$. The value of $\sigma_{bn}(E)$ must be known at low energies where screening effects are important for calculations of astrophysical interest. In this case the reaction takes place in a stellar electron plasma which is different than in a laboratory situation [Ric95].

To correct for measured enhancements of σ_{bn} in a laboratory a good understanding of the electron screening effect is needed. Several studies of reactions involving light nuclei show the experimental enhancement of the cross section at low energies [Gre95, Lan96, Pra94, Cze97, Eng92, Ang93, Jun98]. The observed values of U_e obtained from these studies were close to or higher than the adiabatic limit [Bra90] which corresponds to the theoretical maximum screening potential. For the ^{3}He$(d,p)^4$He reaction the quoted screening potential is slightly higher [Lan96] than allowed by the adiabatic limit. One possible explanation for this discrepancy could be due to errors in the extrapolation of σ_{bn} from the higher-energy data. The R-matrix parameterization should produce an accurate prediction of σ_{bn} down to zero energy.

1.1.3 Polarimetry

The ^{3}He$(d,p)^4$He reaction has many characteristics that make it an excellent choice for determining the polarization of low-energy tensor-polarized deuteron beams. For a polarimeter to be efficient, the figure of merit (defined as the product of σA^2, where σ is the cross section and A is the analyzing power) should be large. The ^{3}He$(d,p)^4$He reaction has a large cross section at low energies due to a resonance, and all the tensor analyzing powers are large at certain angles and smoothly varying with both energy and angle. This makes the figure of merit larger than the D(d,p)T reaction at energies greater than 100 keV and comparable to the T$(d,n)^4$He reaction at energies greater than 400 keV. Other advantages to using the ^{3}He$(d,p)^4$He reaction are that the protons emerge with a large energy, making them easy to detect and ^{3}He is a much safer target to work with than tritium.

Both the ^{3}He$(d,p)^4$He and T$(d,n)^4$He reactions have been used in the past to determine beam polarizations [McI67, Gar74] and in these experiments the analyzing powers were calculated from the assumption that the reaction proceeds only through a $\frac{3}{2}^+$ S-wave resonance with values given by equations 1.1 to 1.4. McIntyre and Haeberli [McI67] used the ^{3}He$(d,p)^4$He reaction at $E_d = 500$ keV for polarimetry and Garrett and Lindstrom [Gar74] used the T$(d,n)^4$He reaction at $E_d = 130$ keV. Precise measurements of the analyzing powers as a function of both energy and angle are very useful for determining tensor polarization accurately at low energies.

1.1.4 Primordial nucleosynthesis

The ^{3}He$(d,p)^4$He reaction, along with the T$(d,n)^4$He reaction, are responsible for most of the production of ^{4}He in the early universe [Smi93]. The cross section data of the ^{3}He$(d,p)^4$He reaction shows some scatter at low energies [Chu93]. Accurate measurements of the total cross section at Big Bang energies (T $\approx$ 0.01

to 0.1 MeV) would therefore be useful for primordial nucleosynthesis calculations.

1.2 Previous work

1.2.1 Theoretical work

There have been many theoretical papers whose focus is to understand the ^{3}He$(d,p)^4$He and T$(d,n)^4$He reactions. Since these are mirror isobaric-analog reactions the calculations are very similar for both. Papers were first written assuming that only S waves contributed to the reaction. Then more complicated approaches involving higher-order partial waves were considered. Calculations within the framework of the Resonating Group Method and R-matrix were also carried out.

McIntyre *et al.* [McI67] were the first to investigate on the analyzing powers the effect of a $^2S_{\frac{1}{2}}$ channel interfering with the resonance. The vector analyzing power was found to be unaffected, while the terms describing the tensor analyzing powers are all found to be affected by the same combination of matrix elements. This results in all of the tensor analyzing powers changing by the same factor if an S-wave, $J = \frac{1}{2}$ contribution exists.

Seiler and Baumgartner [Sei70] outline the possibility of an analysis of the reaction including up to $L = 2$ in the entrance channel. This results in the possibility of 13 matrix elements (listed in Table 1.1) contributing to the reaction. Some of these matrix elements will be negligible and this can be determined by examining the outgoing channel (the $p - \alpha$ system). The first two matrix elements are for S waves in the entrance channel, with the first matrix element forming the $\frac{3}{2}^+$ resonant state in ^{5}Li. Elements 3 thru 7 comprise the P-wave matrix elements. In this paper element 7 was neglected because the exit channel is $^2F_{\frac{5}{2}}$ which has a small elastic scattering phase shift [Pla72]. Of the six elements formed by D waves only elements 8 and 11 (from which the resonant

$\frac{3}{2}^+$ state is formed) and element 10 (which decays by an S wave) are retained. The other matrix elements are discarded because of very small or non-existing phase shifts, as determined from elastic scattering experiments [Pla72]. Seiler and Baumgartner consider only these 9 matrix elements. As a further simplification, since the first matrix element is dominant, only interference terms involving the resonant matrix element with the others are retained. Seiler and Baumgartner derive relationships for several different matrix elements and obtain sets of linear relationships in terms of Legendre function expansion coefficients. Comparison of these relationships with the experimental data provides evidence that this description of the reaction is valid.

Conzett [Con84] did calculations to determine the enhancement of the fusion reaction rate by using both polarized projectiles and targets. An enhancement factor of $\frac{3}{2}$ was calculated using only a contribution from the S-wave $\frac{3}{2}^+$ resonance. In a subsequent paper [Con85] the enhancement was calculated assuming a contribution from the ${}^2S_{\frac{1}{2}}$ entrance channel in addition to the ${}^4S_{\frac{3}{2}}$ channel. For this case the enhancement factor was found to depend on the ratio of the reaction amplitudes, which can be determined experimentally by measurements of both A_{yy} and the polarization transfer coefficient, K_y^y. With only S-waves in the incoming channel, both of these observables are isotropic and measurement at any angle will determine the ratio.

Blüge *et al.* [Blü89, Blü90a, Blü90b] performed calculations describing the ${}^3\mathrm{He}(d,p){}^4\mathrm{He}$ reaction within the framework of the microscopic resonating group model. In Blüge's first paper [Blü89] the focus was on the ${}^3\mathrm{He}(d,p){}^4\mathrm{He}$ reaction at astrophysical energies. Conclusions reached were that the low-energy cross section data can be described by a single Breit-Wigner resonance and that this results in a good extrapolation to astrophysically important energies. Using this extrapolation calculations of electron screening were undertaken.

Blüge *et al.* also investigated the low-energy ${}^5\mathrm{Li}$ spectrum [Blü90a]. A multichannel resonating group calculation based on many-body configurations and

pseudostates was undertaken. Good agreement between the experiment and theory was obtained. No evidence of the $J^\pi = \frac{1}{2}^+$ resonant state in ^{5}Li at $E_d \approx 1 - 3$ MeV as suggested by [McI67] was found. Also, in disagreement with their previous paper [Blü89], contributions from other partial waves were found to interfere with the resonance and these cannot be neglected at very-low energies ($E_R < 20$ keV).

In another paper, Blüge *et al.* [Blü90b] studied both the ^{3}He$(d,p)^4$He and T$(d,n)^4$He reactions with polarized deuterons. Calculations were carried out within the multichannel resonating group model. Again there was no evidence for a $J^\pi = \frac{1}{2}^+$ resonance in ^{5}Li at E_d between 1 and 3 MeV. The calculations show that interference with other partial waves is necessary to describe the analyzing powers. In particular, the calculations indicate that the $^2S_{\frac{1}{2}}$, $^2P_{\frac{1}{2}}$, and $^2P_{\frac{3}{2}}$ channels contribute most to the deviations from a pure resonance calculation. These conclusions are flawed by the fact that they were compared to vector analyzing power data with incorrect sign assignment [Blü90b].

1.2.2 Experimental work

There has been a large body of data obtained for the ^{3}He$(d,p)^4$He reaction. The measurements of the total cross section on the resonance shows a scatter by as much as 30%, Table 1.2. High-precision measurements of complete sets of analyzing powers were made from $E_d = 1$ to 13 MeV [Bit90, Grü71b]. There are also several experiments [Dri80, Har73, Cla73, Grü71a, Kön71, Kli71, Sch76] in which individual data points and excitation functions of observables were measured. Below $E_d = 1$ MeV the polarization data are scarce; only three experiments [Gar74, Lee71, Roh71] have measured complete angular distributions.

Rohrer *et al.* [Roh71] measured the vector analyzing power using a polarized ^{3}He target, $A_y(^3\vec{H}e)$, from 300 keV to 2.5 MeV, while Leemann *et al.* [Lee71] measured analyzing powers and spin-correlation coefficients at 430 keV. Both of these experiments used a gas-cell target and measured beam polarization with

σ_{Tot}(mb)	Author
690	Bonner *et al.* [Bon52]
900 ± 90	Yarnell *et al.* [Yar53]
940 ± 75	Freier and Holmgren [Fre54]
695 ± 35	Kunz [Kun55]
828 ± 41	Möller and Besenbacher [Möl80]
819 ± 26	Davies and Norton [Dav80]

Table 1.2: The value of the total cross section for the ^{3}He$(d,p)^4$He reaction on the resonance, $E_d = 430$ keV.

the T$(d,n)^4$He reaction. The data were expanded in terms of Legendre functions and the values of linear combination of matrix elements were extracted by the procedure of [Sei70]. Evidence was found to suggest that a small part of the reaction proceeds through P- and D-wave channels. The P waves appear to proceed through a direct mechanism, while the D-wave contribution appears to be dominated by the $^4D_{\frac{3}{2}}$ entrance channel.

Garrett and Lindstrom [Gar74] measured complete sets of analyzing powers at 344, 465, and 727 keV, using a gas-cell target. Since they did not have a calibrated polarimeter for this energy range, the mirror reaction, T$(d,n)^4$He, was used to determine the beam polarization at $E_d = 130$ keV assuming that only the $^4S_{\frac{3}{2}}$ entrance channel contributes. The experimental results were analyzed by the method given by Seiler and Baumgartner [Sei70]. They conclude that A_y is due to a mixture of P and D waves, that D waves contribute most strongly through the $^4D_{\frac{3}{2}}$ entrance channel, and that all the P-wave contributions are roughly equal and appear to increase monotonically with energy.

Several experiments have measured angular distributions of the cross section. The measurements are listed in Table 1.3. All these measurements involved the use of a gas cell. The measurements performed below the resonance, $E_d = 430$ keV, yielded isotropic distributions, while at higher energies anisotropic

Author	Reaction	Energies (keV)
Bonner *et al.* [Bon52]	^{3}He$(d,p)^4$He	E_d = 430, 1140, 1600
Kunz [Kun55]	D$(^3$He$,p)^4$He	E_{He} = 200, 290, 350
Yarnell *et al.* [Yar53]	^{3}He$(d,p)^4$He	E_d = 260, 455, 978, and higher
Krauss *et al.* [Kra87]	^{3}He$(d,p)^4$He	E_d = 25, 80, 176, 237

Table 1.3: Summary of angular distribution cross section measurements below 1 MeV beam energy for the ^{3}He + D system.

angular distributions were observed.

1.3 Present work

The sensitivity of analyzing powers to the reaction mechanism makes them a reasonable observable to use in understanding some of the problems discussed in Section 1.1. Due to the scarcity of polarization data at low energies, precision measurements of complete sets of analyzing powers were taken around the resonance and also extended to lower energies than previously been measured. Also, measurements of angular distributions of the cross section and of an excitation function are necessary to clear up the discrepancies between previous measurements.

Our measurements are used in a R-matrix parameterization of the ^{5}Li system (Chapter 6) and also in calculations to describe the reaction with both a resonant and direct contribution. From the R-matrix analysis, the level structure of ^{5}Li is investigated and also cross section calculations from the parameterization are used in electron-screening calculations.

Chapter 2

Beams, Transport, and Targets

To measure cross sections and analyzing powers, one needs a source of polarized ions, a beam transport system, a scattering chamber, and targets. Considerable time was invested in developing both ^{3}He and deuterium targets suitable for these measurements. Completion of the development of the high-voltage target chamber and an upgrade to the beam-transport system were crucial to obtain the beam energies necessary for this experiment.

2.1 Atomic beam polarized ion source

The Atomic Beam Polarized Ion Source (ABPIS) [Cle95a] developed at TUNL is able to produce positive or negative beams of polarized or unpolarized protons and deuterons. The source is also able to produce unpolarized ^{3}He and ^{4}He beams. A diagram of the ABPIS is shown in Figure 2.1. For this project deuteron and ^{3}He beams were used. The more-intense positive beams were used for energies that could be reached without using the minitandem accelerator, see section 2.2.4.

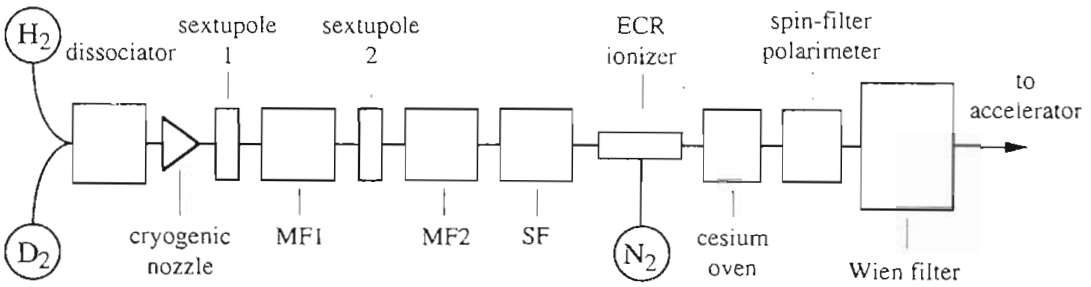

Figure 2.1: Diagram of the atomic beam polarized ion source.

2.1.1 Source operation

The polarized ion source contains five sections. The dissociator section is used to make a neutral atomic beam by breaking molecular gas with a radio-frequency field. The beam next passes into a region where it is polarized [Din95]. This is accomplished with two sextupole magnets and several radio-frequency transition units (medium field units (MF1 and MF2) and the strong field unit (SF)). Next comes a section that contains an electron-cyclotron-resonance (ECR) ionizer and a cesium oven [Cle95b]. The ECR ionizer produces a positive beam. When needed, the cesium oven produces a negative beam by charge exchange in a cesium vapor. The spin-filter region [Men96] is used to measure the beam polarization by use of a Lamb shift polarimeter. Finally, the beam passes through the Wien filter which orients the spin-quantization axis so that it is in the proper direction when it reaches the target.

2.1.2 Transitions used

The two sets of transitions units used in this experiment are summarized in Table 2.1; one set for the tensor polarized beam and one set for the vector polarized beam. A sequence of three states was cycled through for measurements performed with either the vector or tensor beam polarizations. The first state was an unpolarized state made with all the transition units off and the second

Beam		States		States		States		
State	MF1	Left	SF	Left	MF2	Left	P_z	P_{zz}
1	off	1,2,3	off	1,2,3	off	1,2,3	0	0
Deuteron Vector Polarized States								
2	off	1,2,3	$3 \leftrightarrow 6$	1,2,6	off	1,2,6	$\frac{2}{3}$	0
3	off	1,2,3	off	1,2,3	$1 \leftrightarrow 4$	2,3,4	$-\frac{2}{3}$	0
Deuteron Tensor Polarized States								
2	off	1,2,3	$3 \leftrightarrow 5$	1,2,5	off	1,2,5	$\frac{1}{3}$	-1
3	off	1,2,3	off	1,2,3	$2 \leftrightarrow 4$	1,3,4	$-\frac{1}{3}$	1

Table 2.1: Transition units used and the maximum theoretical beam polarization. Listed in the columns under each transition unit (MF1, SF, or MF2) is either the transition that is made or "off" indicating that the unit was not used.

and third states were polarized states. The states were switched by spin-flip tansitions, using electronics set up in the control room. All three states were cycled through once a second by turning on and off the rf power supplies to the transition units.

2.2 Low-energy beam facility

The main components of the low-energy beam facility (LEBF) at TUNL are the minitandem accelerator [Bla93], the high-voltage target chamber [Lud97], and a smaller scattering chamber [Fle92]. The minitandem accelerator was upgraded during the summer of 1995 for a maximum voltage on the terminal of 200 keV. The development of the high-voltage chamber was completed in the spring of 1995 with the chamber successfully holding 200 keV of positive potential. Both of these devices were crucial to obtaining the measurements over the energy range of interest.

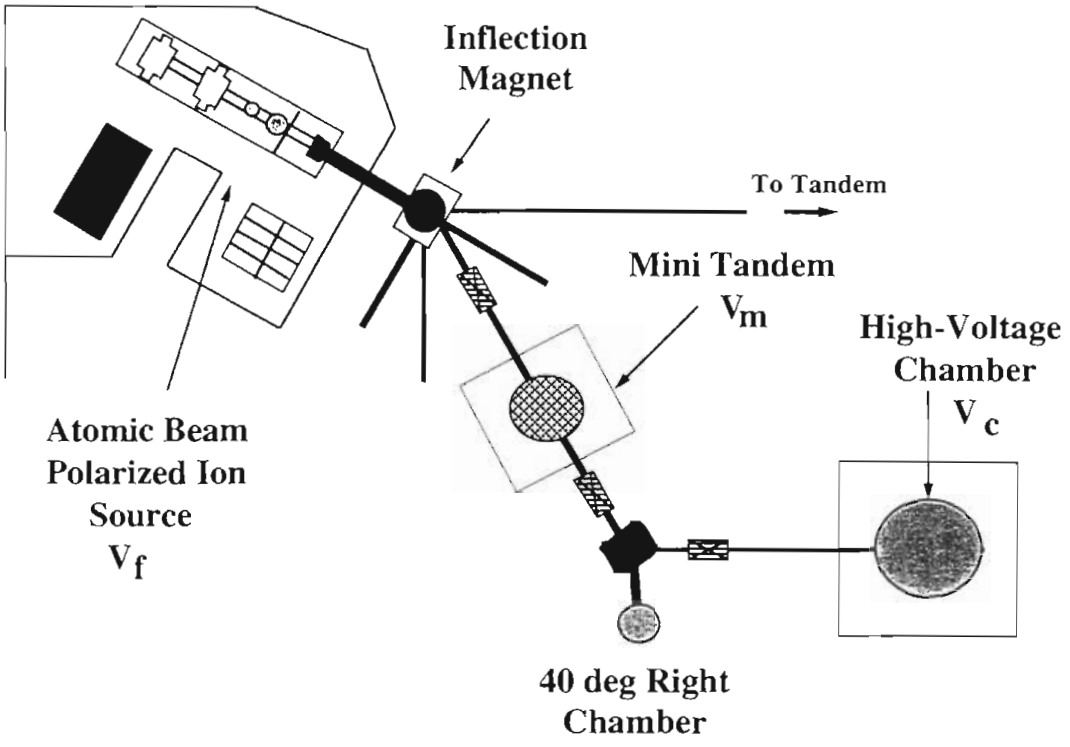

Figure 2.2: Diagram of the low-energy beam facility. V_f, V_m, and V_c refers to the potential applied to the source, minitandem, and high-voltage chamber respectively.

2.2.1 Beam transport

A view of LEBF is shown in Figure 2.2. The ABPIS injects beam into the inflection magnet which is used to steer the beam into various beam lines. Either positive or negative beam can be directed into LEBF, which is located 30° to the right (facing downstream) of the ABPIS line.

The layout of the components on the LEBF beam line before and after the minitandem upgrade is shown in Figure 2.3. The major changes were the installation of longer accelerator tubes and the replacement of the electrostatic quadrupoles with compact magnetic quadrupoles. The magnetic quadrupole is the first focusing device the beam encounters in the LEBF, followed by an electrostatic steerer. A set of slits allows for control of the amount of beam sent into the minitandem and an air operated Faraday cup measures the beam current at

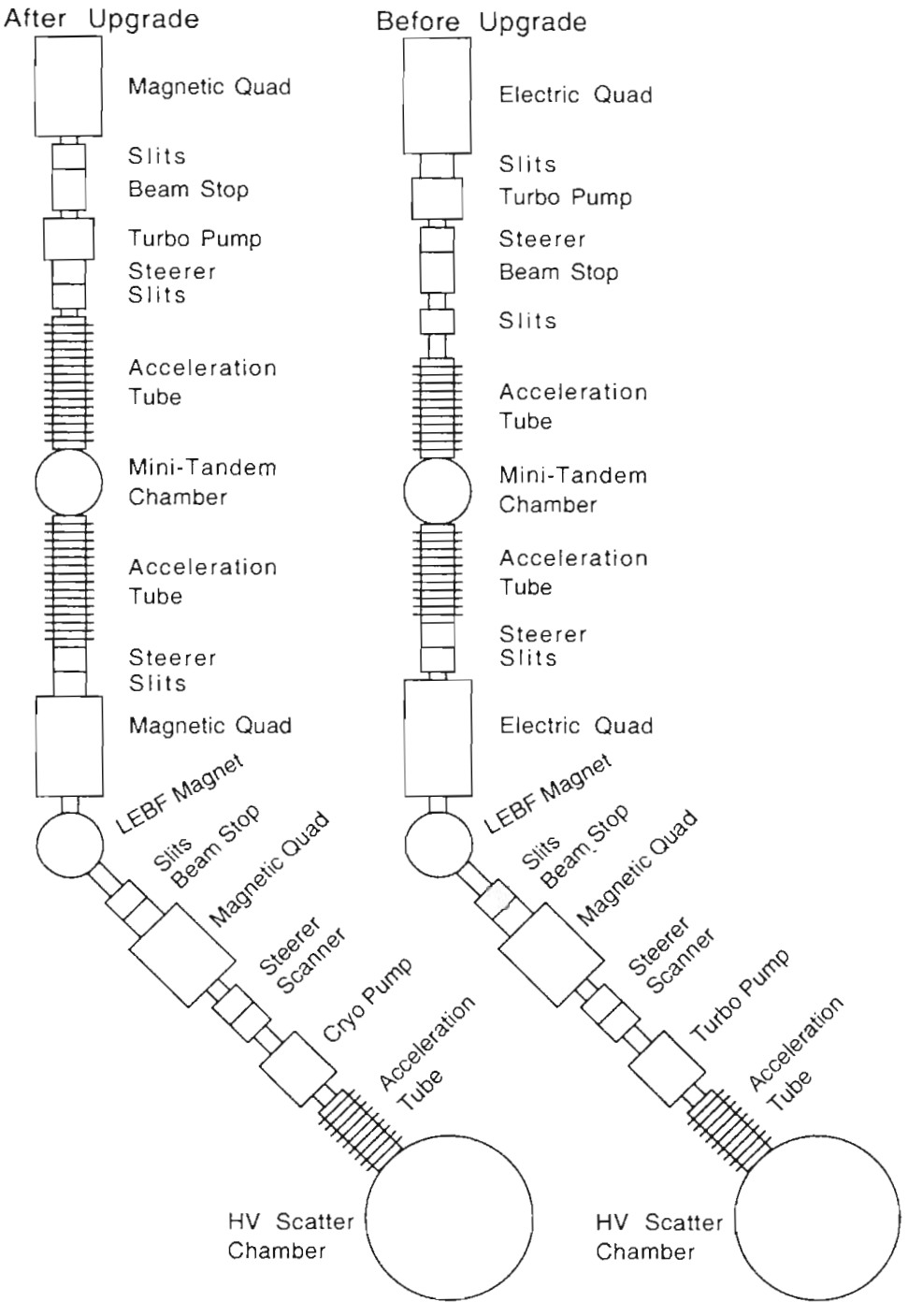

Figure 2.3: Diagram of the low-energy beam facility (LEBF) transport system before (right side) and after (left side) the minitandem upgrade.

this point. The beam passes through the minitandem accelerator which can be operated with or without a terminal potential. Following the minitandem is a steerer - slit - quadrupole combination to control the beam going into the LEBF inflection magnet. The LEBF inflection magnet can be set to bend the beam toward either the high-voltage chamber located 45° to the left or another scattering chamber located 40° to the right. The 40° chamber is described in [Fle92] and, since this work was done in the high-voltage chamber, only the 45° left leg components are discussed here. The beam exiting the LEBF magnet at 45° left will encounter another slit - quadrupole - steerer combination to focus the beam into the high-voltage chamber. There is also another beam stop located along this leg to measure the beam current before entering the high-voltage chamber. A scanner is located in this region to observe the profile of the beam and to help when steering the beam into the high-voltage chamber.

The low-energy beam facility has three pumping stations that maintain the vacuum in the 10^{-6} Torr range. The first station is located before the minitandem and is a 500-ℓ/s turbo pump. There is a 60-ℓ/s turbo pump mounted on the rotating-slit box between the minitandem and the LEBF magnet. The final pumping station is located between the LEBF magnet and the high-voltage chamber and uses a 1500-ℓ/s cryo-pump.

2.2.2 Minitandem accelerator

The minitandem accelerator [Bla93] is shown in Figure 2.4. It consists of a 51-cm-diameter vacuum chamber with a rotating carousel inside. The carousel can hold 12 carbon foils. The vacuum chamber is supported by a ceramic insulator and connected to the beam line by two 55-cm-long acceleration tubes. When in operation, polished aluminum hemispheres are placed below and above the chamber to reduce corona discharge and sparking. The minitandem is capable of being biased to a positive potential of $V_m = 200$ kV. A negative beam entering the minitandem will be accelerated to the terminal potential and then stripped

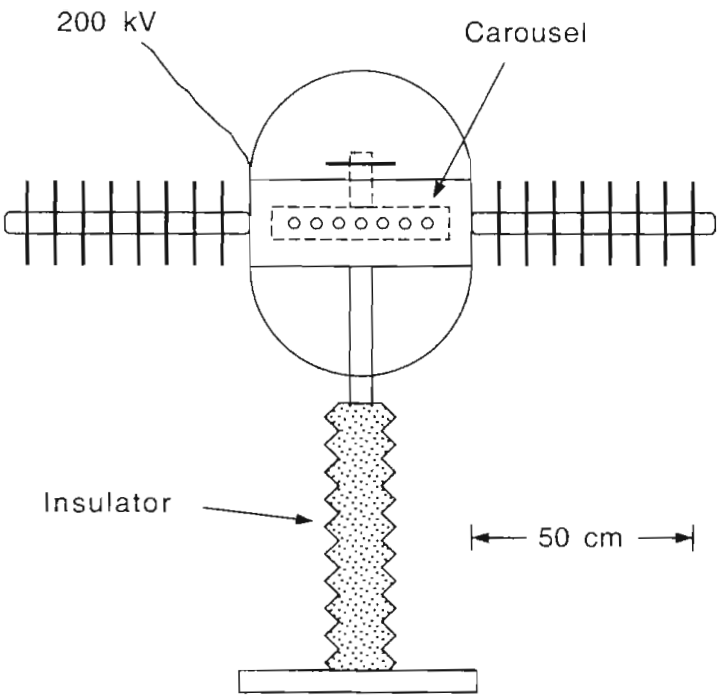

Figure 2.4: Schematic view of the minitandem accelerator.

of its electrons in a carbon foil. The positive beam will then be repelled by the positive potential on the minitandem, resulting in a gain in energy equal to twice the terminal potential.

The upgrade to the minitandem increased the maximum terminal potential from $V_m = 125$ to 200 kV. This was done by replacing the acceleration tubes with new ones that are rated for 200 kV. Also the insulator supporting the minitandem had to be replaced with a longer one and the fence was redesigned so that it is at a sufficient distance to prevent sparking when the minitandem is operated at the maximum potential.

2.2.3 High-voltage target chamber

The high-voltage chamber [Lud97] is shown in Figure 2.5. This is a large 107-cm-diameter scattering chamber. The chamber is supported by three ceramic insulators and connected to the beam line by a 76-cm-long acceleration tube.

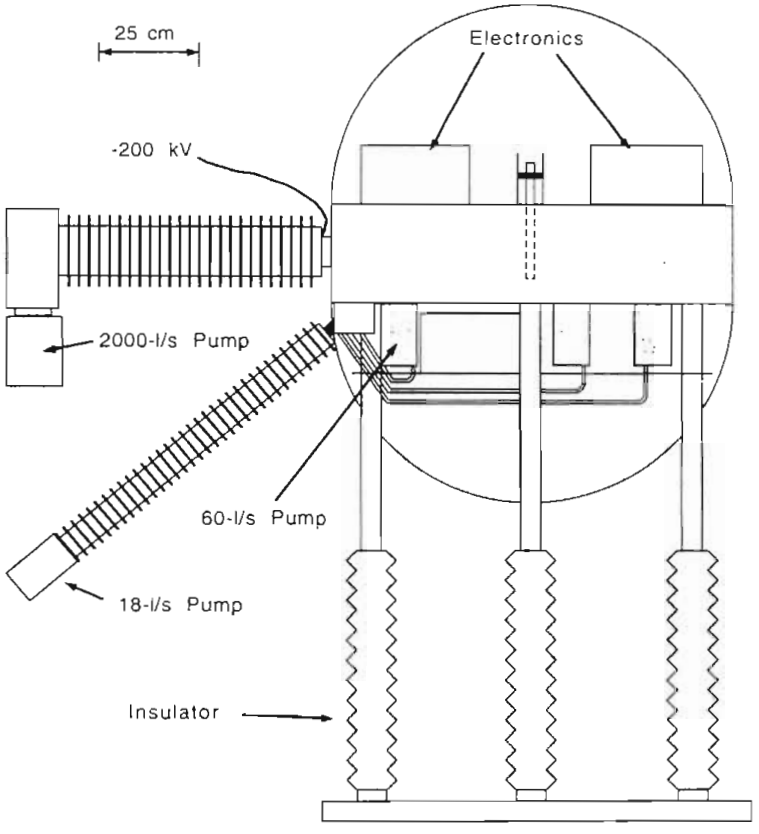

Figure 2.5: External view of the high-voltage chamber.

Two aluminum hemispheres are attached to the top and bottom of the chamber to minimize large potential gradients, which can cause sparking. The chamber can be biased by a maximum of $V_c = 200$ kV. Signal processing NIM electronics are placed in mini bins both above and below the scattering chamber inside the domes and fiber-optic links are used to send the signals from high voltage to ground. Three 60-ℓ/s turbo pumps are attached to the chamber to keep the vacuum in the 10^{-6} Torr range. Because the turbo pumps operate at high voltage, the vacuum backing is accomplished through an acceleration tube by a 18-ℓ/s molecular-drag pump placed at ground potential. The molecular-drag pump maintains a sufficient vacuum to prevent electrical discharge down the backing line. Attempts were made to use other materials for the backing line, such as PCV and glass, but electrical discharges occurred as the chamber was

biased. The only way to prevent these discharges was to maintain a potential gradient along this line, just as in an acceleration tube. An isolation transformer supplies the necessary power to run pumps and electronics at high voltage.

The spatial characteristics of the chamber make it ideal for measurements using silicon surface barrier detectors. An internal diagram of the high-voltage target chamber is shown in Figure 2.6. A set of isolated horizontal and vertical slits which define the beam geometry is located in an adjustable cylindrical tube at the entrance of the chamber. Detectors can be positioned on 66-cm-diameter plates located on the top and bottom of the chamber. These plates are free to rotate independently and are used to maintain detectors at equal angles to the left and right of the beam. Detector holders can be positioned at any distance up to 25 cm from the target on tracks located on the plates. Each plate has four tracks that can be positioned independently to set angles. Fixed monitor detectors can be positioned in the back of the chamber out of the reaction plane so that they are not blocked by detectors on the rotating plate. A target rod capable of holding up to five targets is located in the center of the chamber and is isolated from the chamber to allow measurement of beam current. A Faraday cup or polarimeter can be inserted into a port in the rear of the chamber to measure beam current or beam polarization respectively.

2.2.4 Running modes

Two modes of running with the deuteron beam were used, depending on the beam energy needed. Positive beam from the source was used when the required beam energy was less than 280 keV and negative beam was used for beam energies greater than 280 keV. In the positive-beam mode the minitandem was not used and the beam energy is $E_d = V_f + V_c$, where V_f is the frame voltage of the source and V_c is the voltage of the chamber. In this case, E_d can have a maximum value of 280 keV. In the negative-beam mode a voltage V_m was applied to the terminal of the minitandem. The beam energy for this case is equal to $E_d = V_f + 2V_m + V_c$

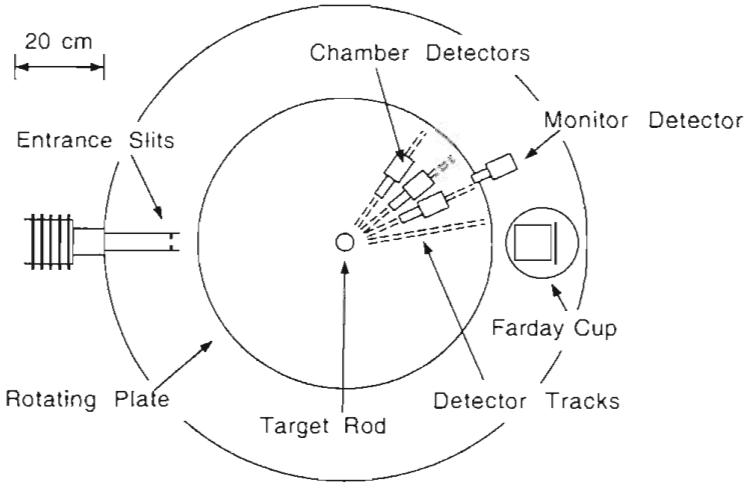

Figure 2.6: Internal diagram of the high-voltage chamber.

and can reach a maximum value of 680 keV. It is advantageous to use positive beam when possible because ten times more beam is then available on target than with negative beam. This is due to the fact that beam is not lost in the source from the charge-exchange process.

2.3 Targets

Making a helium target for low-energy beams is difficult because traditional methods for fabricating targets will not work. Since helium is a noble gas, the target cannot be formed as one of the constituents of a molecule that could be incorporated into a target. The traditional gas-cell approach is not applicable here because a low-energy deuteron beam will lose most of its energy in the entrance foil. A gas-jet target was also ruled out because of the large cost of development and the impractibility of biasing it to the required potential.

As a solution, ion-implanted ^{3}He targets [Gei96] were developed. These targets worked well for this experiment because the deuteron beam loses only a minimal energy in the implanted region, resulting in small range of sampled reaction energies. Also, the large Q-value for the $^3\mathrm{He}(d,p)^4\mathrm{He}$ reaction means that

the outgoing protons lose little energy passing through the substrate and can be easily detected. Deuterated carbon targets [Bla95] were also used in this research to measure cross sections for the D(^{3}He, p)^{4}He reaction.

2.3.1 Ion-implanted ^{3}He targets

Since at low beam energies the cross sections are very small we wanted to maximize the amount of ^{3}He in the target. In order to do this, the mechanisms that limit the thickness of implanted ions must be considered. The mechanism of ion implantation in foils has been studied previously [Alm61] and has been described for hydrogen and helium [Sch83]. They conclude that the thickness of implanted ions is dependent on the sputtering yield of the substrate, the range and mobility of the ions in the substrate, the fluence, and the temperature of the substrate. To maximize the target thickness, a substrate that has a low sputtering yield should be used. Sigmund [Sig81] gives a description of the sputtering process, and comparisons between experimental results and theory are given by Anderson [And81]. Based on these data, tantalum was chosen as the main substrate because of its low sputtering yield and easy availability. Aluminum substrates were also studied for comparison.

The ion-implanted targets were developed and produced in the thin-film laboratory at UNC. A General Ionex Sputterbell system [Gen] was used to produce ^{3}He ion beams of energies up to 20 keV and intensities of up to 8 mA. The ion beam was accelerated out of the ion source and focussed onto the substrate with an Einzel lens. The ions traveled approximately 14 cm before implanting into the substrate at normal incidence angle. The substrate was mounted on an isolated liquid-nitrogen-cooled cold finger where the beam current was collected. In order to get an accurate measurement of the fluence, the substrate was biased positively to suppress the emission of electrons.

Target thicknesses were measured at TUNL using the low-energy beam facility. These measurements were made with several different batches of targets.

Implant Energy (keV)	Thickness (10^{17} ^{3}He/cm^2)
7	0.63
17	1.04
20	2.10

Table 2.2: The dependence of the target thickness on the implant energy.

The typical setup consisted of using two 1000-μm-thick silicon surface-barrier detectors placed at forward angles symmetrically about the beam to measure protons from the ^{3}He$(d,p)^4$He reaction. The solid angle for these measurements was on the order of 10 msr and the tests were conducted at an energy near the resonance, E_d = 430 keV, to maximize the proton yield. With knowledge of the differential cross section[3] and solid angle, the target thickness, N_t, was determined by

$$N_t = \frac{N_p}{(N_d)(\partial\sigma/\partial\Omega)(\Delta\Omega)} \tag{2.1}$$

where N_p is the number of detected protons, N_d is the number of incident deuterons, $\partial\sigma/\partial\Omega$ is the differential cross section, and $\Delta\Omega$ is the solid angle.

In order to determine how to make the thickest targets, the effect of several parameters on the target thickness was tested. Several targets were made at different implant energies with about the same fluence and the results showed that the targets with the higher implant energies were thicker, see Table 2.2. The dependence of the target thickness for different fluences was tested at the same implant energy. The thickness was found (see Figure 2.7) to be constant after an initial increase. Sputtering is believed to be one of the limiting factors in achieving greater thickness. At the start of target production, all the ions will be implanted into the substrate, but after some time the newly implanted ^{3}He ions will sputter away ions that were previously implanted. Once this equilibrium is reached, the substrate will not hold any more ions. Sputtering damage to the

[3]The first measurements were taken at E_d = 330 keV and an isotropic differential cross section of 56 $\pm$ 2.8 mb/sr from [Kra87] was assumed.

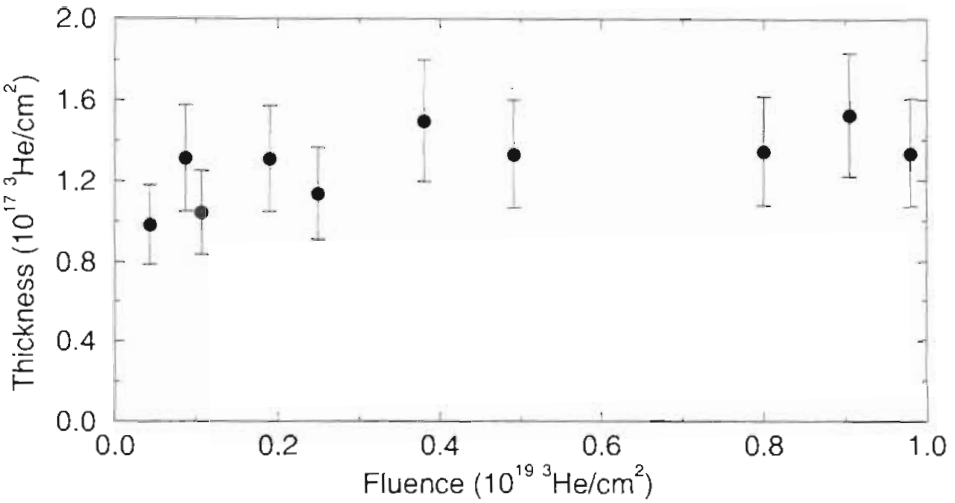

Figure 2.7: The dependence of the target thickness on the fluence at an implant energy of 17 keV.

	Thickness (10^{17} ^{3}He/cm^2)	
Energy (keV)	Cool Area	Hot Area
13	1.7	1.0
17	2.2	1.8

Table 2.3: The dependence of the target thickness on the temperature of the substrate.

substrate can be seen using an atomic force microscope [Fal95], see Figure 2.8.

The effect of substrate temperature on the thickness was also investigated. Even though the targets were cooled during implantation, some areas still began to glow due to beam heating. These hot areas were isolated from the cooler areas and, as seen in Table 2.3, the cooler areas yielded a larger target thickness. The stability of these targets in a beam was tested by bombarding a target with a 322-keV, 320-nA beam. Only a slow decrease in thickness was observed (see Figure 2.9) although experience with beam currents on the order of 1 μA show much faster loss of target thickness. No depletion of thickness during storage was observed.

Figure 2.8: Atomic force microscope image of the surface of the tantalum substrate before (a) and after (b) implantation with a fluence of 1.6×10^{19} ions/cm^2.

2.3.2 Deuterated carbon targets

Deuterated carbon targets were used to measure the absolute cross section as well as an excitation function of the cross section for the D(^{3}He, p)^{4}He reaction. These targets were well suited for this purpose because the energy loss in the target is much easier to determine than for ion-implanted targets.

In the first attempts to make deuterium targets, self-supporting deuterated carbon targets were used [Bla95]. The self-supporting targets broke when exposed to the ^{3}He beam. This occurred even when beam currents as low as 2 nA were used. Subsequent targets were made with an aluminum backing and these targets did not break with either the deuteron or ^{3}He beams.

The targets were fabricated in a very similar process to that described in [Bla95]. They were made with the plasma-assisted-chemical-vapor-deposition chamber. Aluminum foil of about $\approx$ 0.015-mm thickness was glued to target rings and placed between two electrodes within the chamber. A small amount of deuterated methane gas was flowed into the chamber while also being pumped by a mechanical pump. Once the pressure equalizes a high potential is applied between the electrodes until a plasma ignites. The current is then read from the plates until the desired thickness (collected charge) is reached.

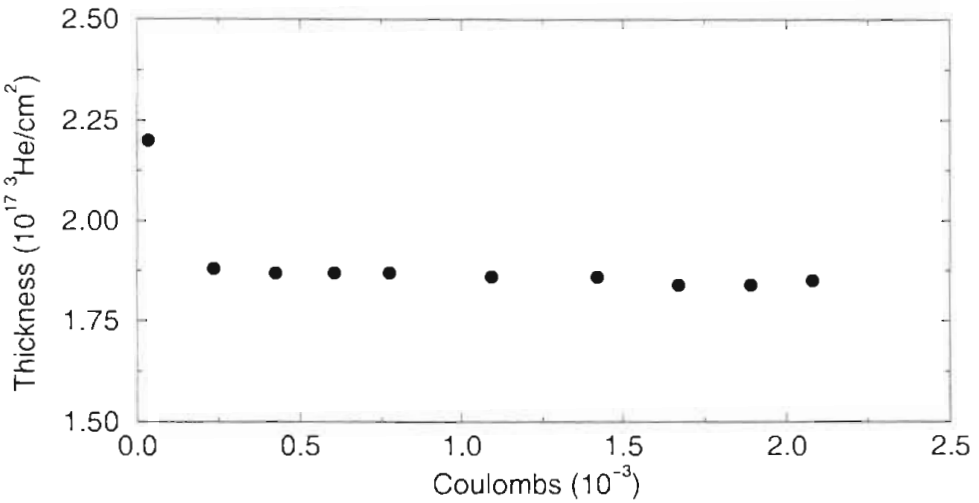

Figure 2.9: Ion-implanted ^{3}He target stability under bombardment of a 322-keV, 320-nA deuteron beam.

Charge (C)	Thickness (10^{17} D/cm^2)
7	1.5
14	3.2
21	4.4

Table 2.4: Average deuterium thickness for the deuterated carbon targets.

The targets were tested with a deuteron beam to determine both the deuterium thickness and target stability. These tests were carried out at the same time that the measurement of the total cross for the ^{3}He$(d,p)^4$He reaction was done. The experimental setup is described in Section 3.3.3. Listed in Table 2.4 is the target thickness for three different amounts of charge collected while making the targets; the thickness is roughly proportional to the collected charge. The stability of the targets was tested at a beam energy of 480 keV and with 700 nA of beam current. As seen in Figure 2.10, the deuterium thickness drops quickly at the start of the beam bombardment and then levels off, while the carbon thickness increases slowly.

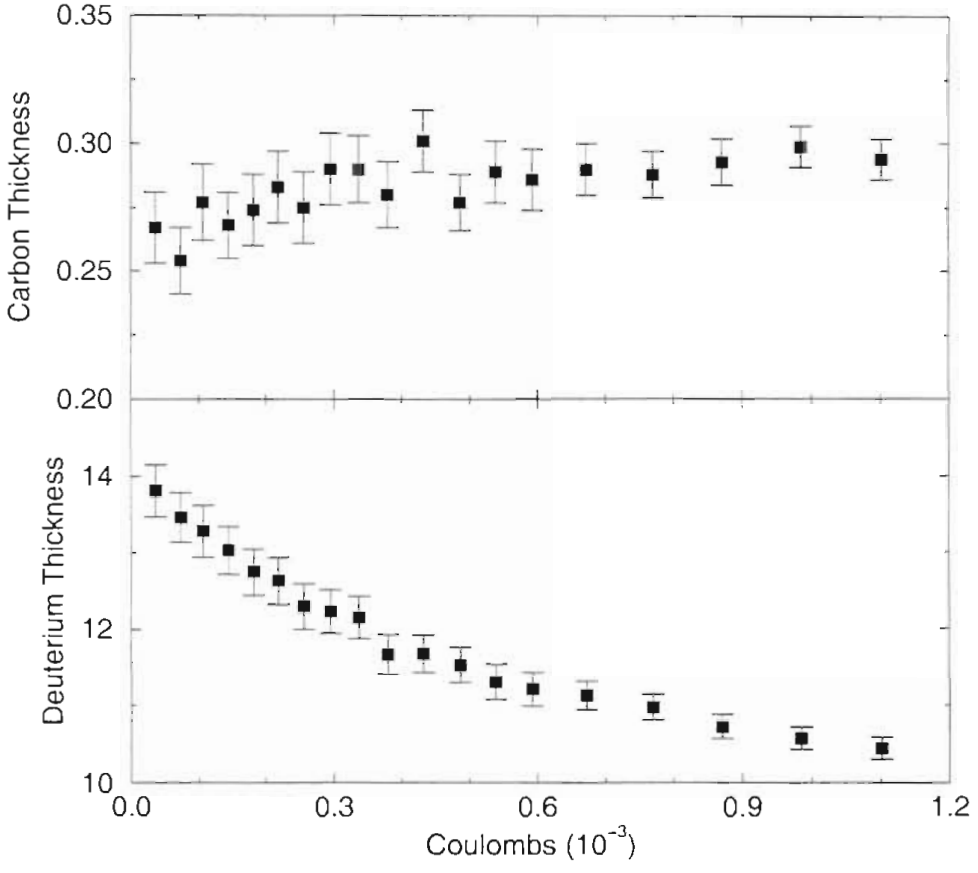

Figure 2.10: Deuterated carbon target stability under bombardment by a 480-keV, 700-nA deuteron beam.

Chapter 3

Experimentation

The design of an experimental setup is influenced by several factors. These factors may include consideration of count rates, presence of contaminant peaks, angular dependence of observable, and magnitude of measured observable. Additionally, the measurements of analyzing powers require more sophisticated setups to extract the observables with the smallest error. The analyzing-power formalism is first reviewed, then the experimental setup and procedure for the different measurements is discussed.

3.1 Analyzing-power formalism

Measurements involving a polarized beam of spin-1 particles are described in detail by Ohlsen [Ohl73]. The intensity of counts deposited in a detector, $I(\theta,\phi)$, placed at angles θ and ϕ can be represented by

$$\begin{aligned} I(\theta,\phi) &= I_o(\theta)\Big\{1+\frac{3}{2}p_z A_y(\theta)\sin\beta\cos\phi - p_{zz}A_{xz}(\theta)\sin\beta\cos\beta\sin\phi \\ &\quad +\frac{1}{2}p_{zz}A_{yy}(\theta)\sin^2\beta\cos 2\phi \\ &\quad +\frac{1}{4}p_{zz}A_{zz}(\theta)\Big[3\cos^2\beta-1+\sin^2\beta\cos 2\phi\Big]\Big\} \end{aligned} \tag{3.1}$$

where $I_o(\theta)$ is the intensity of counts deposited in the detector with the same amount of an unpolarized beam, p_z and p_{zz} are the vector and tensor polarization

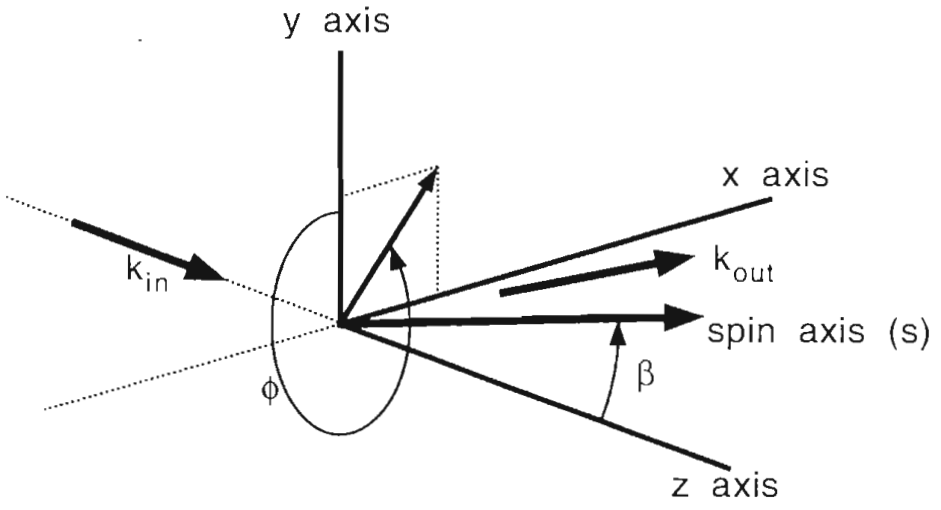

Figure 3.1: The Madison Convention coordinate system [Mad71]. The z-axis is defined to be along the momentum of the incident particles. The y-axis is formed by $k_{in} \times k_{out}$ and the x-axis is chosen to form a right handed coordinate system. The angle β is the angle between the z-axis and the spin axis, S, and ϕ is the angle from the y-axis to the projection of S in the x-y plane.

of the beam, and A_y, A_{yy}, A_{xz}, and A_{zz} are the analyzing powers for the reaction. The angle θ is the angle between k_{in} and k_{out} while the angles ϕ and β are determined in the Madison Convention [Mad71] by the detector location and the direction of the spin-quantization axis of the polarized particles, see Figure 3.1.

3.1.1 Formalism for A_y and A_{yy}

For the measurement of A_y and A_{yy} the spin-quantization axis is set perpendicular to the reaction plane, corresponding to $\beta = 90°$. The expression for the intensity in the detectors, after substituting β in equation 3.1, is given by

$$I(\theta,\phi) = I_o(\theta)\Big\{1 + \frac{3}{2}p_z A_y(\theta)\cos\phi + \frac{1}{2}p_{zz}A_{yy}(\theta)\cos 2\phi + \frac{1}{4}p_{zz}A_{zz}(\theta)\Big[\cos 2\phi - 1\Big]\Big\}. \quad (3.2)$$

According to the Madison Convention, the left and right detectors will have $\phi = 0°$ and $\phi = 180°$ respectively. Substituting these values into equation 3.2

yields

$$L = 1 + \frac{3}{2}p_z A_y + \frac{1}{2}p_{zz}A_{yy}$$
$$R = 1 - \frac{3}{2}p_z A_y + \frac{1}{2}p_{zz}A_{yy} \tag{3.3}$$

where $L = I(\theta, 0°)/I_o(\theta)$ and $R = I(\theta, 180°)/I_o(\theta)$. Taking the combination of $L - R$ yields an equation for A_y

$$A_y = \frac{L - R}{3p_z} \tag{3.4}$$

and the combination of $L + R$ yields an equation for A_{yy}

$$A_{yy} = \frac{L + R - 2}{p_{zz}}. \tag{3.5}$$

Taking the ratio of polarized counts over unpolarized counts cancels errors due to different efficiencies and solid angles between left and right detectors. Also, taking the proper combinations of the counts in left and right detectors cancels contributions from the other analyzing powers that influence the observed yields. This technique allows the measurement of the analyzing powers to high accuracy by reducing other errors, such as spin-quantization-axis misalignments. However, it does require accurate measurements of the beam current for the different beam states.

3.1.2 Formalism for A_{zz}

For the measurement of the tensor-polarization component A_{zz} the spin quantization axis is in the reaction plane and along the beam momentum direction, corresponding to $\beta = 0°$. Substituting this into equation 3.1 yields

$$I(\theta, \phi) = I_o(\theta)\Big\{1 + \frac{1}{2}p_{zz}A_{zz}(\theta)\Big\}. \tag{3.6}$$

In this case the angle ϕ is undefined and the L and R ratios are equal,

$$L = R = 1 + \frac{1}{2}p_{zz}A_{zz}. \tag{3.7}$$

The combination of $L + R$ yields an equation for A_{zz}

$$A_{zz} = \frac{L + R - 2}{p_{zz}}. \tag{3.8}$$

Also note that A_{zz} can be solved by using the individual detectors

$$\begin{aligned} A_{zz} &= \frac{2(L-1)}{p_{zz}} \\ A_{zz} &= \frac{2(R-1)}{p_{zz}}. \end{aligned} \tag{3.9}$$

3.1.3 Formalism for A_{xz}

For measuring A_{xz}, the spin quantization axis is set in the reaction plane, corresponding to $\beta = 45°$. Substituting into equation 3.1 yields

$$\begin{aligned} I(\theta,\phi) &= I_o(\theta)\Big\{1 + \frac{3\sqrt{2}}{4}p_z A_y(\theta)\cos\phi - \frac{1}{2}p_{zz}A_{xz}(\theta)\sin\phi \\ &\quad + \frac{1}{4}p_{zz}A_{yy}(\theta)\cos 2\phi + \frac{1}{8}p_{zz}A_{zz}(\theta)\Big[1 + \cos 2\phi\Big]\Big\}. \end{aligned} \tag{3.10}$$

For the left and right detectors $\phi = 270°$ and $\phi = 90°$ respectively, and substituting into equation 3.10 yields

$$\begin{aligned} L &= 1 + \frac{1}{2}p_{zz}A_{xz} - \frac{1}{4}p_{zz}A_{yy} \\ R &= 1 - \frac{1}{2}p_{zz}A_{xz} - \frac{1}{4}p_{zz}A_{yy} \end{aligned} \tag{3.11}$$

where $R = I(\theta, 90°)/I_o(\theta)$ and $L = I(\theta, 270°)/I_o(\theta)$. The combination of $L - R$ gives

$$A_{xz} = \frac{L - R}{p_{zz}}. \tag{3.12}$$

An interesting point to note is that by taking the combination of $L + R$ with $\beta = 45°$ one can obtain an equation for A_{yy} given by

$$A_{yy} = \frac{-2(L + R - 2)}{p_{zz}}. \tag{3.13}$$

As will be pointed out in Section 4.2.2, this is not the best way to measure A_{yy}. Any small spin quantization misalignments will cause a large error in the analyzing power. However, this information can be used to estimate the uncertainties in the spin-quantization direction.

E (keV)	Detector	Slit size (cm)	Solid angle (msr)
199,424,641	all	0.64 × 1.27 oval	4.95
60,99	pair 1 and 3	1.59 dia circle	19.2
60,99	pair 2	2.22 dia circle	29.7

Table 3.1: Summary of detector geometry for the analyzing power measurements.

3.2 Analyzing power measurements

Complete angular distributions for the ^{3}He$(d,p)^4$He reaction were taken for A_y, A_{yy}, A_{xz}, and A_{zz} at five energies. The measurements were made at TUNL using the low-energy beam facility described in Section 2.2, and the beam was produced with the atomic beam polarized ion source, see Section 2.1.

3.2.1 Chamber setup and experimental procedure

As discussed in Section 3.1, the most accurate way to measure analyzing powers (except A_{zz}) requires that the reaction be measured with detectors placed symmetrically about the beam direction. To meet these requirements, three pairs of 1000-μm-thick silicon detectors were placed in the high-voltage scattering chamber. A piece of 0.127-mm-thick Ta foil was placed in front of the detectors to slow the protons so they would be stopped in the detectors and to prevent scattered particles from entering the detectors. The smooth dependence of the analyzing powers on the scattering angle allows the use of large solid angles to maximize the count rate. A summary of the collimator slit sizes and solid angles for the analyzing power measurements is given in Table 3.1. The detectors were placed on the rotating tracks inside the high voltage chamber at a separation angle of 20°.

The target rod was loaded with four ion-implanted ^{3}He targets and one empty target ring and was biased by 90 V to attract electrons and thereby provide better beam integration. In the rear of the chamber either a deuteron tensor or vector

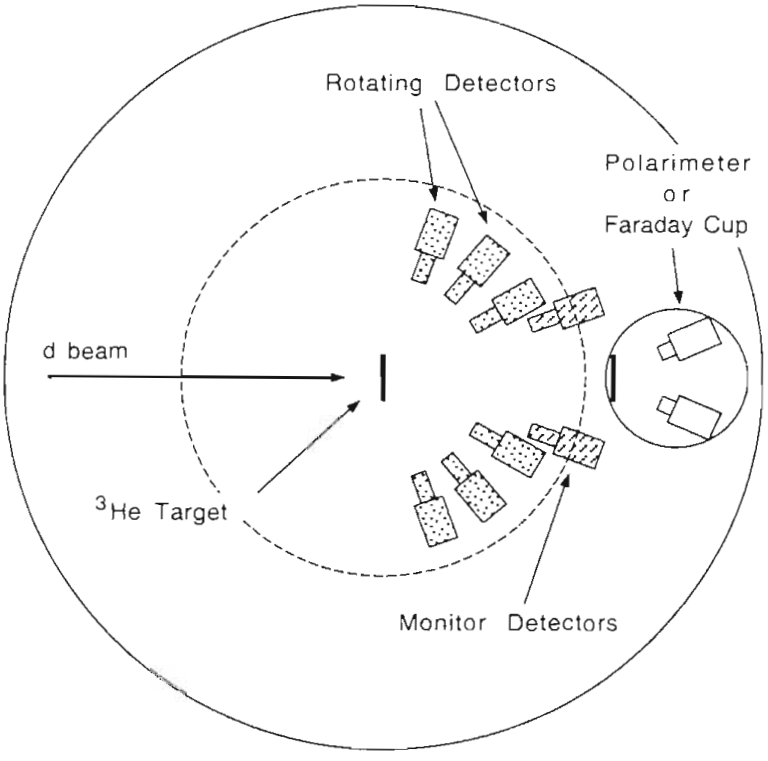

Figure 3.2: Chamber setup for the analyzing power and relative cross section measurements. The monitor detectors and a Faraday cup were used only for the cross section measurements.

polarimeter (see Appendix A) was placed. A drawing of the chamber setup is shown in Figure 3.2 and a typical spectrum is shown in Figure 3.3.

At the start of the measurements the beam was tuned through an empty target ring to maximize the current on the polarimeter while minimizing the current on the target ring. Once a good tune was reached, the beam polarization was measured in the polarimeter. A target was then placed in the beam and the detectors were rotated to symmetric angles in order to measure the analyzing powers.

The tensor analyzing power angular distributions were measured in 10° steps, except at the lowest energy where, due to the slower count rate, 20° steps were taken. For the vector analyzing powers 20° steps were taken at all energies. At the higher energies one run was taken until enough counts were in the spectrum

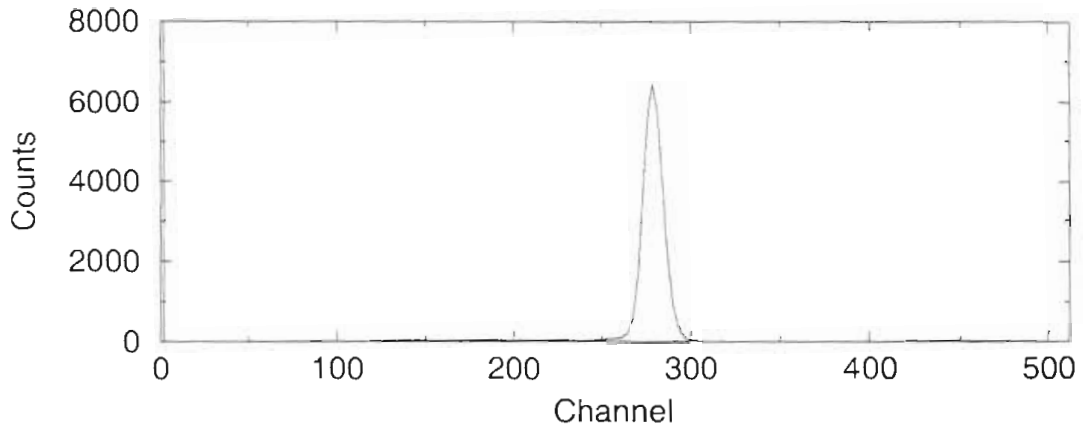

Figure 3.3: Typical spectrum taken with the chamber detectors from the ^{3}He$(d,p)^4$He reaction at $E_d = 429$ keV.

for acceptable statistics, but for the lower energies several runs at the same energy were often required. The beam polarization was checked every couple of hours by putting in the blank target ring and allowing the beam to pass directly into the polarimeter. At the lower energies ($E_d = 69$, 108, and 206 keV) the high-voltage chamber was biased to the maximum amount to increase the beam energy up to 270 keV, an energy where the polarimeter is more efficient.

3.2.2 Electronics

Signals from the detectors were processed in two different ways depending on whether the high-voltage chamber was biased or not as shown in Figures 3.4 and 3.5. The setups are very similar except that the signals had to be sent through the fiber optics and the pulser was fed into the electronics at ground potential when the high-voltage chamber was biased. For the high-voltage mode, one could run with the pulser output sent directly into the preamplifier but this would require one more fiber-optic line and more electronics on the chamber.

The spin-flip electronics, Figure 3.6, controls the three different spin states that are used, see Section 2.1.2, when running with a polarized beam. The spin-flip electronics sends the spin-state information to both the polarized-ion

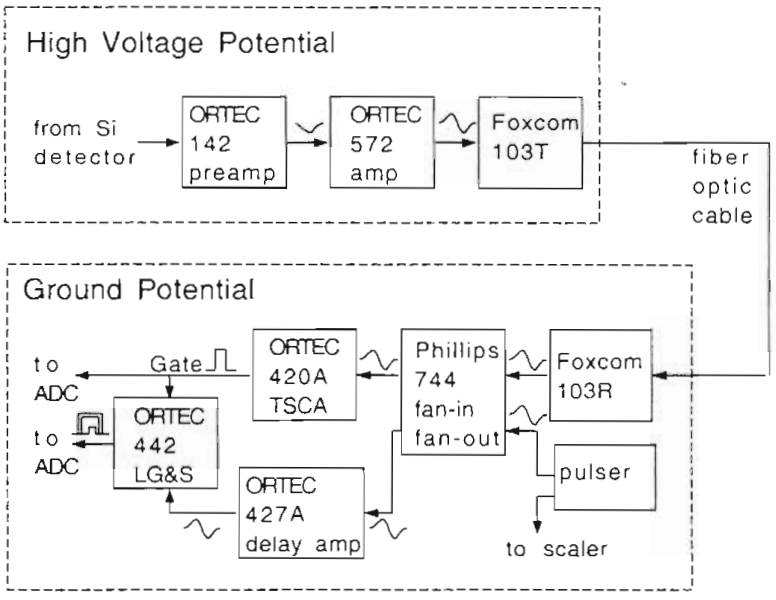

Figure 3.4: Detector electronics when running with the high-voltage chamber biased.

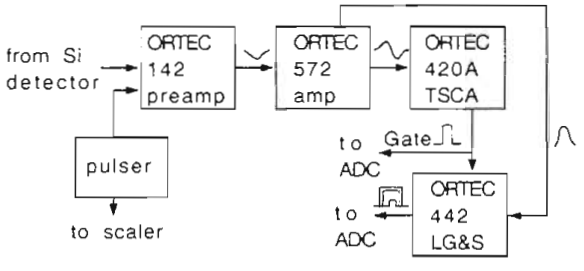

Figure 3.5: Detector electronics when running with the high-voltage chamber grounded.

source and the computer interface. The three spin-state signals are made using the TUNL spin-state controller which produces two opposite TTL levels in a repeating sequence of +−−+−++−, where + means the signal is TTL high (+5V) and - means the signal is TTL low (0V). By gating these two signals with another signal from a gate-and-delay generator, three mutually exclusive signals corresponding to different spin states are produced, as shown in the bottom left of Figure 3.6. These state signals are sent to the polarized-ion source forcing the appropriate transition units to be turned on and off. The signals received back from the source are used to drive the routing and scaler control bits on the

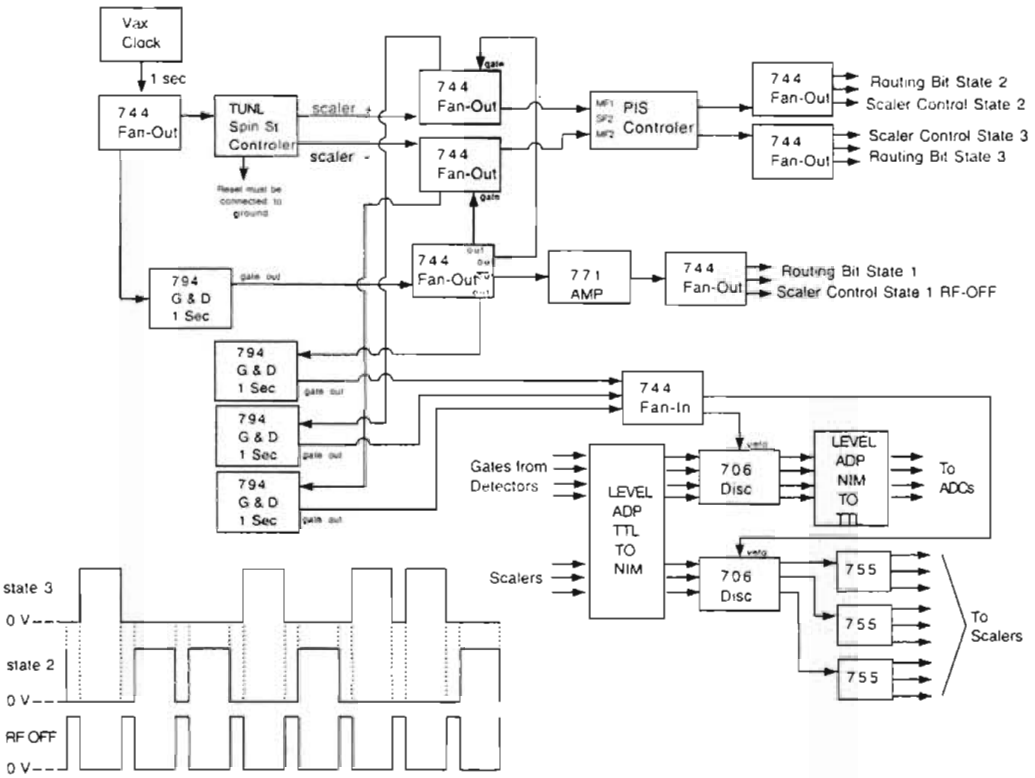

Figure 3.6: Diagram of the spin-flip electronics. The diagram in the lower left corner shows the time sequence of the three spin-state signals. Note that only one spin state is high at a time.

computer. A 12-ms-wide gate is used to veto the detector gates and scalers while the transition units are changing states. The duration of time in the unpolarized state (state 1) can be easily changed by adjusting the width of the state-1 gate on the gate-and-delay generator.

3.3 Cross section measurements

3.3.1 Relative angular distribution

The chamber setup and electronics were essentially the same as described in the analyzing power measurements (Section 3.2) except that the spin-flip electronics were not used and fixed-angle monitor detectors were placed in the cham-

E (keV)	Detector	Slit size (cm)	Solid angle (msr)
199,424,641	chamber	0.64 × 1.27 oval	2.86
199,424,641	monitor	1.27 dia circle	1.22
60,99	chamber	1.27 dia circle	21.8
60,99	monitor	2.41 dia circle	54.5

Table 3.2: Summary of detector geometry for the relative cross section measurements.

ber, see Figure 3.2. In some of the measurements the polarimeter was replaced by a Faraday cup. To obtain a relative cross section angular distribution, counts in the rotating detectors were normalized to counts in the monitor detectors and all the chamber detectors were cross normalized by measuring the relative cross section for each detector at 0°. The rotating detectors were placed at a greater distance from the target than for the analyzing power measurements in order to not block the fixed monitor detectors. A summary of the detector characteristics for the relative angular distributions is shown in Table 3.2.

3.3.2 Excitation function measurements

The excitation function was measured in two ways: one with a deuteron beam and a ^{3}He target and the other with a ^{3}He beam and a deuterium target. In both methods the target rod was biased to suppress electrons and the beam was tuned through an empty target ring to ensure accurate beam integration. The counts at each energy were normalized to the BCI[4] counts and several points were remeasured to allow for a correction due to a loss of target thickness.

[4]The acronym BCI stands for beam current integrator, but it often refers to the integrated beam current or similarly the number of integrator pulses received from the beam current integrator.

Deuteron beam measurement

The excitation function was measured by placing two detectors symmetrically about the beam at backward angles to measure the protons from the ^{3}He$(d,p)^4$He reaction. The deuteron beam was tuned onto an ion-implanted ^{3}He target and once a good tune was achieved the beam energy was changed over a range of 200 keV using the high-voltage chamber. This was done at several different minitandem voltages resulting in an excitation function over the range from 250 to 650 keV.

^{3}He beam measurement

A deuterated carbon film on an aluminum backing, as described in Section 2.3.2, was used as the target. Two pairs of detectors were placed at 20° and 160° and a pair of monitor detectors was placed at 140°. The monitor detectors were used to detect elastically-scattered particles in order to measure the energy loss in the deuterated carbon film. A diagram of the chamber setup is shown in Figure 3.7. The 160° detector detected the protons from the D$(^3$He$,p)^4$He reaction while the 20° detector detected both the protons and alpha particles. Typical spectra are shown in Figure 3.8. The broad proton peak in the $\theta = 20°$ and $\theta_R = 160°$ detectors is due to the fact that the protons were not stopped in the detectors. The $\theta_L = 160°$ detector was thicker (2000 μm) than the other detectors allowing all the energy of the proton to be deposited in the detector.

The excitation function was obtained by accelerating a ^{3}He beam through the minitandem and/or the high-voltage chamber. The double-charged ^{3}He ions were analyzed with the LEBF magnet and sent into the high-voltage chamber. The beam was tuned at one fixed minitandem voltage and then adjusted over a range of 400 keV with the high-voltage chamber to measure the cross section at several different energies. This procedure was repeated at several different minitandem voltages, resulting in measurements over an energy range corresponding to a

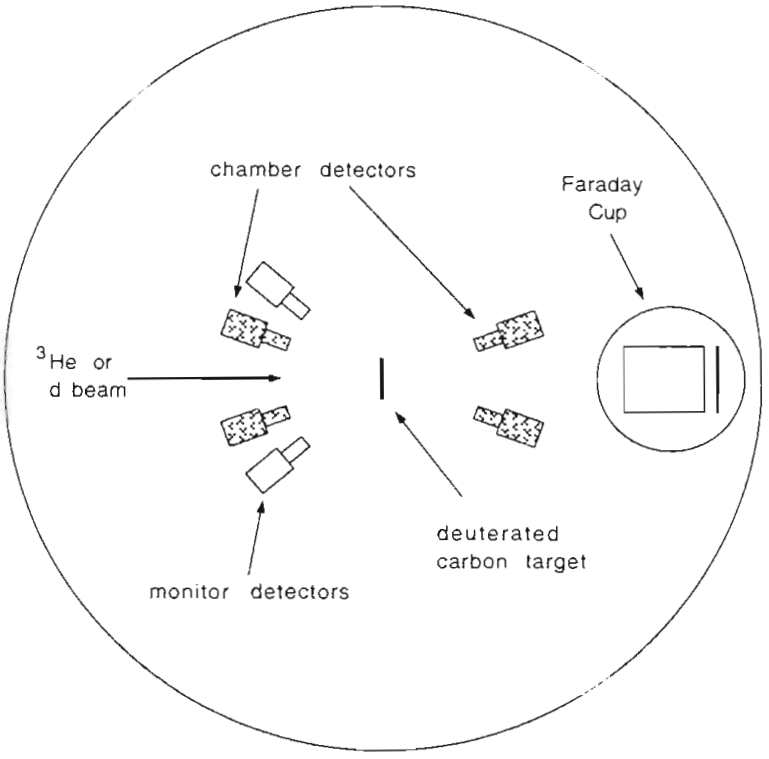

Figure 3.7: Chamber setup used for the excitation function measurements with a ^{3}He beam and the absolute cross section measurements.

deuteron energy in the ^{3}He$(d,p)^4$He reaction of 245 to 685 keV.

3.3.3 Absolute cross sections

The absolute cross section measurements used the deuterated carbon targets along with beams of both deuterons and ^{3}He. The deuteron beam was used to determine the deuterium thickness in the target, while the ^{3}He beam was used to determine the cross section for the ^{3}He$(d,p)^4$He reaction. The chamber setup is identical to that used to measure the excitation function with a ^{3}He beam, Figure 3.7.

First, a deuteron beam was tuned into the chamber at 116 keV where the cross section for the D(d,p)T reaction is known to better than 3% [Bro90]. A sample spectrum of the protons from the D(d,p)T reaction is shown in Figure 3.9. Measurements were made on several targets and the beam was kept on the targets

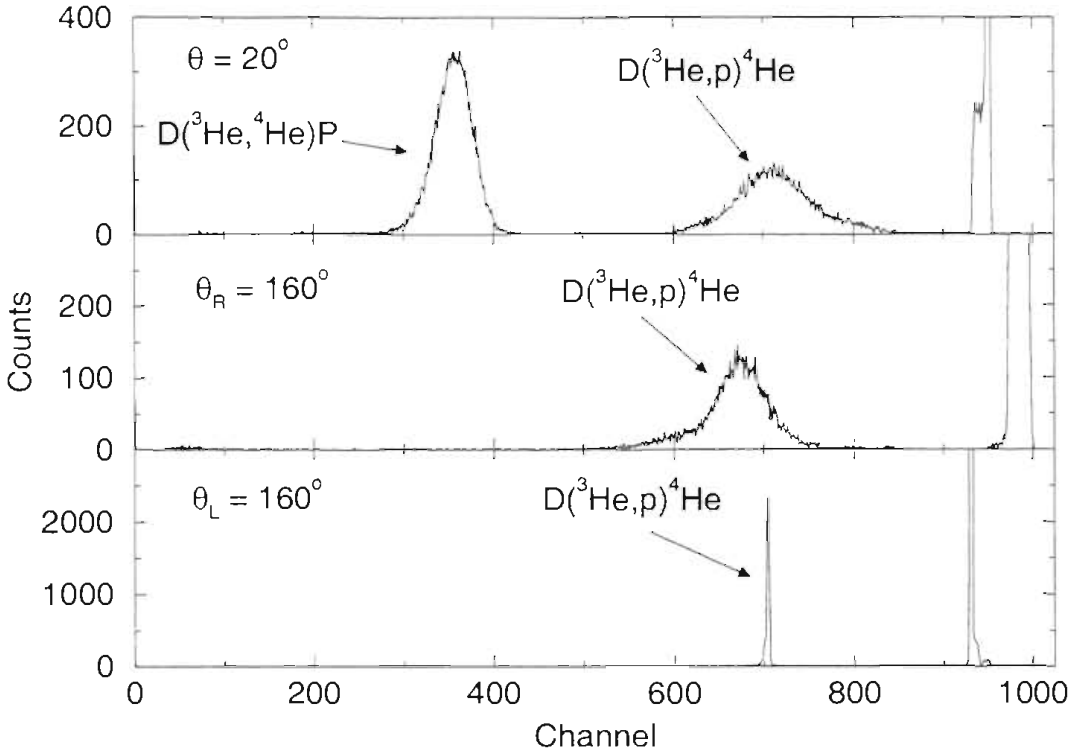

Figure 3.8: Typical spectra for the chamber detectors from the $D(^3He,p)^4He$ reaction. These spectra were taken with a ^3He beam energy of 651 keV. The peak located farthest to the right in all the spectra is due to the pulser.

only long enough to get good statistics in order to minimize the potential loss of deuterium from the target. Next, a ^3He beam was accelerated at the resonance energy, $E_{He} = 651$ keV, and measurements were made in the same way as with the deuteron beam. The spectra with the ^3He beam look the same as for the excitation function measurement, Figure 3.8. The target thickness was then measured again with the deuteron beam. In all of the measurements the target was biased by 90 V to ensure proper beam integration.

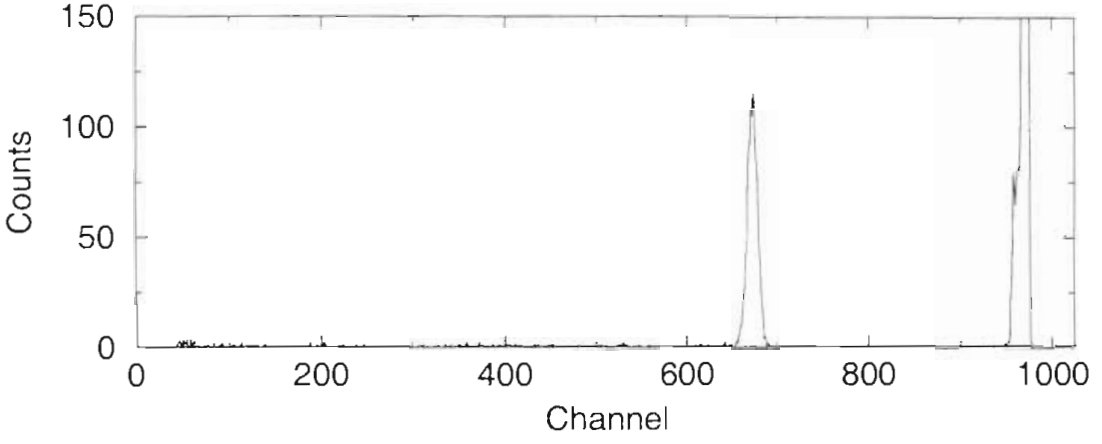

Figure 3.9: A typical spectrum resulting from the $D(d,p)T$ reaction in the chamber detectors at a beam energy of 116 keV. The protons are the only particles detected. The truncated peak located near channel 950 is due to the pulser.

Chapter 4

Data Reduction

The data reduction process leading from the number of counts in the detectors to values of observables can be a complicated and tedious task. In this chapter the process of determining the values and errors of experimental quantities will be discussed. When analyzing spectra this process involves extracting the number of counts in a peak of interest and then reducing these counts into useful quantities. Extracting counts from a peak can be very difficult if a background exists, but fortunately in this experiment the background under the peaks was negligible and was not considered. The lack of a background is due to the fact that the ^{3}He$(d,p)^4$He reaction has a large Q-value and the experiment was performed at low beam energies (well below the deuteron breakup threshold). All of the data reduction was done with the aid of a Micro-Vax computer. Programs were written to sum the counts in the spectra and manipulate these sums to determine useful quantities. Also discussed is the determination of the reaction energy and the Wien filter settings.

4.1 Analyzing powers

For the determination of the analyzing powers, the counts were first extracted from the spectra. Then ratios of counts in the polarized state to counts in the unpolarized state were taken and these ratios were corrected for both the collected

charge and dead time. The corrected ratio from the left, L, or right, R detector is given by

$$L \text{ or } R = \left(\frac{C_p}{C_\circ}\right)\left(\frac{BCI_\circ}{BCI_p}\right)\left(\frac{DTC_p}{DTC_\circ}\right) \tag{4.1}$$

where C is the number of particles detected in the left or right detectors, BCI is the number of integrated charge pulses, DTC[5] is the dead time correction, and the subscripts p and $\circ$ refer to polarized and unpolarized states respectively. The analyzing powers are then determined from these ratios using the equations given in Section 3.1.

4.2 Errors in the analyzing powers

4.2.1 Statistical errors

The standard deviation of a function of several variables f can be estimated by propagating the error using [Bev92]

$$\sigma_f^2 = \sum_i^n \left(\frac{\partial f}{\partial i}\right)^2 \sigma_i^2, \tag{4.2}$$

where the sum is over the number of variables in f. This is often the procedure used when finding the statistical error, even though it ignores the correlated error terms. The expression including the correlated errors is,

$$\sigma_F^2 = \sum_i^n \left(\frac{\partial f}{\partial i}\right)^2 \sigma_i^2 + 2\sum_i^n \sum_{j>i}^n \rho(j,i)\left(\frac{\partial f}{\partial i}\right)\left(\frac{\partial f}{\partial j}\right) \tag{4.3}$$

where the term $\rho(j,i)$ is the correlation coefficient between variables i and j. If, the correlation coefficients are small equation 4.2 will give a reasonable approximation to the error. In this work the correlation coefficients were not calculated, but are assumed to be small.

[5]The dead time correction is calculated by comparing the number of pulser signals that are seen the spectrum with the number of pulses sent to the detectors, determined by a scaler.

One can find the equations for the standard deviation of the analyzing powers by using equation 4.2. The analyzing powers are formed by taking ratios of counts and the expressions for the ratios are

$$\begin{aligned} R &= \frac{C_p^r}{C_o^r} \\ \Delta R &= R\sqrt{\left(\frac{\Delta C_p^r}{C_p^r}\right)^2 + \left(\frac{\Delta C_o^r}{C_o^r}\right)^2} \\ L &= \frac{C_p^l}{C_o^l} \\ \Delta L &= L\sqrt{\left(\frac{\Delta C_p^l}{C_p^l}\right)^2 + \left(\frac{\Delta C_o^l}{C_o^l}\right)^2} \end{aligned} \tag{4.4}$$

where C is the counts, the superscripts r and l refer to the right and left detectors respectively, the subscripts p and o refer to the polarized and unpolarized states respectively, and $\Delta C_i^j = \sqrt{C_i^j}$. Using these equations, one can easily get the equations for the standard deviations of the analyzing powers:

$$A_y = \frac{L-R}{3p_z} \tag{4.5}$$

$$\Delta A_y = \frac{1}{3p_z}\sqrt{(\Delta L)^2 + (\Delta R)^2 + (3A_y\Delta p_z)^2} \tag{4.6}$$

$$A_{yy} = \frac{L+R-2}{p_{zz}} \tag{4.7}$$

$$\Delta A_{yy} = \frac{1}{p_{zz}}\sqrt{(\Delta L)^2 + (\Delta R)^2 + (A_{yy}\Delta p_{zz})^2} \tag{4.8}$$

$$A_{zz} = \frac{L-R-2}{p_{zz}} \tag{4.9}$$

$$\Delta A_{zz} = \frac{1}{p_{zz}}\sqrt{(\Delta L)^2 + (\Delta R)^2 + (A_{zz}\Delta p_{zz})^2} \tag{4.10}$$

$$A_{zz} = \frac{2(L-1)}{p_{zz}} \tag{4.11}$$

$$\Delta A_{zz} = \frac{1}{p_{zz}}\sqrt{(2\Delta L)^2 + (A_{zz}\Delta p_{zz})^2} \tag{4.12}$$

$$A_{zz} = \frac{2(R-1)}{p_{zz}} \tag{4.13}$$

$$\Delta A_{zz} = \frac{1}{p_{zz}}\sqrt{(2\Delta R)^2 + (A_{zz}\Delta p_{zz})^2} \tag{4.14}$$

$$A_{xz} = \frac{L-R}{p_{zz}} \tag{4.15}$$

$$\Delta A_{xz} = \frac{1}{p_{zz}}\sqrt{(\Delta L)^2 + (\Delta R)^2 + (A_{xz}\Delta p_{zz})^2} \tag{4.16}$$

4.2.2 Error due to spin-axis misalignment

Improper setting of the rotation and the magnitude of the magnetic field in the Wien filter can lead to misalignments of the deuteron beam spin-quantization axis at the target. To get an idea of the effect this can have on the analyzing powers, the Taylor expansion of the trigonometric functions are evaluated about β and ϕ and inserted into our general equation for the counts in the detectors, equation 3.1. This results in an expression for the number of counts in a detector as a function of $\Delta\beta$ and $\Delta\phi$, the uncertainties in β and ϕ, respectively:

$$\begin{aligned}
&I(\theta,\phi) + \Delta I(\theta,\phi) = \\
&\quad I_o(\theta)\Big\{1 + \frac{3}{2}p_z A_y(\theta)(\sin\beta + \Delta\beta\cos\beta)(\cos\phi - \Delta\phi\sin\phi) \\
&\qquad - p_{zz}A_{xz}(\theta)(\sin\beta + \Delta\beta\cos\beta)(\cos\beta - \Delta\beta\sin\beta)(\sin\phi + \Delta\phi\cos\phi) \\
&\qquad - \frac{1}{2}p_{zz}A_{yy}(\sin^2\beta + 2\Delta\beta\cos\beta\sin\beta)(\cos 2\phi - 2\Delta\phi\sin 2\phi) \\
&\qquad + \frac{1}{4}p_{zz}A_{zz}(\theta)\Big[3(\cos^2\beta - 2\Delta\beta\cos\beta\sin\beta) - 1 \\
&\qquad\quad + (\sin^2\beta + 2\Delta\beta\cos\beta\sin\beta)(\cos 2\phi - 2\Delta\phi\sin 2\phi)\Big]\Big\}.
\end{aligned} \tag{4.17}$$

In order to evaluate this effect on the analyzing powers, one needs an estimate of $\Delta\beta$ and $\Delta\phi$. By analyzing A_{yy} when β is set to 45°, the value for $\Delta\beta$ is estimated to be at most 3° as will be discussed later. The error in ϕ is due to the detectors being placed out of the reaction plane (horizontal plane in this case) and this is estimated to be no more than a degree. The detector angular acceptance, shown in Table 4.1, is a source of much greater uncertainty.

E (keV)	Detector	$\Delta\theta$	$\Delta\phi$
199,424.641	All	1.5°	3.0°
60.99	pairs 1,3	4.5°	4.5°
	pair 2	5.6°	5.6°

Table 4.1: Summary of the angular acceptance. The angular opening in the plane of the detectors is $2\Delta\theta$ and out of the plane is $2\Delta\phi$.

Effects in A_y and A_{yy}

For measurement of A_y and A_{yy}, $\beta = 90°$. $\phi = 0°$ for the left detector, and $\phi = 180°$ for the right detector is substituted into equation 4.17 and results in

$$\begin{aligned} L + \Delta L &= 1 + \frac{3}{2} p_z A_y + p_{zz} A_{xz} \Delta\beta\Delta\phi + \frac{1}{2} p_{zz} A_{yy} \\ R + \Delta R &= 1 - \frac{3}{2} p_z A_y - p_{zz} A_{xz} \Delta\beta\Delta\phi + \frac{1}{2} p_{zz} A_{yy}. \end{aligned} \tag{4.18}$$

The combination $L - R$ gives a solution of A_y,

$$A_y + \Delta A_y = \frac{L - R - 2 p_{zz} A_{xz} \Delta\beta\Delta\phi}{3 p_z}. \tag{4.19}$$

The vector analyzing power can be seen to have only a second-order error effect due to spin-direction misalignment. But, for the ^{3}He$(d,p)^4$He reaction this could cause problems because A_y is very small while A_{xz} is large at some angles. The polarization states were chosen at the source such that there is no tensor polarization[6] (see Table 2.1), and this results in A_y free from errors due to spin misalignment. Taking the combination $L + R$ results in

$$A_{yy} + \Delta A_{yy} = \frac{L + R - 2}{p_{zz}} \tag{4.20}$$

and the tensor analyzing power A_{yy} is free from error due to first-order spin misalignments.

[6]From measurements done at tandem energies with a ^{3}He$(d,p)^4$He deuteron polarimeter [Ton81] with these spin states, the tensor polarization was found to be less than 5%.

Effects in A_{xz}

For measurement of A_{xz}, β is set to 45°, $\phi = 270°$ for the left detector, and $\phi = 90°$ for the right detector. Substituting these values into equation 4.17 yields

$$\begin{aligned} L + \Delta L &= 1 + \frac{3\sqrt{2}}{4} p_z A_y(\theta)(1 + \Delta\beta)\Delta\phi + \frac{1}{2} p_{zz} A_{xz}(\theta)(1 - \Delta\beta^2) \\ &\quad - \frac{1}{2} p_{zz} A_{yy}(\frac{1}{2} + \Delta\beta) - p_{zz} A_{zz}(\theta)\Delta\beta \\ R + \Delta R &= 1 - \frac{3\sqrt{2}}{4} p_z A_y(\theta)(1 + \Delta\beta)\Delta\phi - \frac{1}{2} p_{zz} A_{xz}(\theta)(1 - \Delta\beta^2) \\ &\quad - \frac{1}{2} p_{zz} A_{yy}(\frac{1}{2} + \Delta\beta) - p_{zz} A_{zz}(\theta)\Delta\beta. \end{aligned} \tag{4.21}$$

Taking the combination $L - R$ yields

$$A_{xz} + \Delta A_{xz} = \frac{L - R - \frac{3\sqrt{2}}{2} p_z A_y(\theta)(1 + \Delta\beta)\Delta\phi}{p_{zz}(1 - \Delta\beta^2)}. \tag{4.22}$$

For this experiment A_y is small (≈ 0.03) compared to the other analyzing powers, so the term $\frac{3\sqrt{2}}{2} p_z A_y(\theta)(1 + \Delta\beta)\Delta\phi$ is very small (<0.001) and can be neglected. The remaining expression has an error in the second order in β, so errors due to spin misalignment can be neglected for A_{xz} measurements.

With the proper combination of the L and R counts, as noted in Section 3.1.3, one can determine A_{yy} from measurements at $\beta = 45°$, as seen in equation 3.13. The effects of spin misalignment on A_{yy} are obtained by taking the combination of $L + R$,

$$A_{yy} + \Delta A_{yy} = -\Big(\frac{L + R - 2}{p_{zz}(\frac{1}{2} + \Delta\beta)} + \frac{2A_{zz}\Delta\beta}{(\frac{1}{2} + \Delta\beta)}\Big). \tag{4.23}$$

It is clear from inspection of equation 4.23 that one should not measure A_{yy} in this scheme because any small-spin quantization misalignment will cause a large error. For example, using a $\Delta\beta = 3°$ and $A_{zz} = \frac{1}{2}$ will result in an error of 20% in A_{yy}. This sensitivity of A_{yy} to $\Delta\beta$ allows one to estimate a value for $\Delta\beta$ using known values of the analyzing powers A_{yy} and A_{zz}. This was obtained by varying $\Delta Beta$ until A_{yy} calculated from equation 4.23 agreed with A_{yy} values measured with $\beta = 90°$. This technique yielded $\Delta\beta \leq 3°$.

Effects in A_{zz}

For measurement of A_{zz}, β is set to 0° and equation 4.17 yields:

$$\begin{aligned} I(\theta,\phi)+\Delta I(\theta,\phi) &= I_o(\theta)\Big\{1+\frac{3}{2}p_z A_y(\theta)\Delta\beta(\cos\phi-\Delta\phi\sin\phi) \\ &\quad -p_{zz}A_{xz}(\theta)\Delta\beta(\sin\phi-\Delta\phi\cos\phi) \\ &\quad +\frac{1}{2}p_{zz}A_{zz}\Big\}. \end{aligned} \tag{4.24}$$

When $\beta = 0°$, ϕ is undefined and does not enter into the equation but when β differs from 0° the angle ϕ will differ by 180° for the left and right detector. Substituting $\phi = \phi'$ for the left detector and $\phi = \phi' - 180°$ for the right detector, yields:

$$\begin{aligned} L+\Delta L &= 1+\frac{3}{2}p_z A_y(\theta)\Delta\beta(\cos\phi'-\Delta\phi\sin\phi') \\ &\quad -p_{zz}A_{xz}(\theta)\Delta\beta(\sin\phi'-\Delta\phi\cos\phi')+\frac{1}{2}p_{zz}A_{zz} \\ R+\Delta R &= 1+\frac{3}{2}p_z A_y(\theta)\Delta\beta(\cos(\phi'-180°)-\Delta\phi\sin(\phi'-180°)) \\ &\quad -p_{zz}A_{xz}(\theta)\Delta\beta(\sin(\phi'-180°)-\Delta\phi\cos(\phi'-180°))+\frac{1}{2}p_{zz}A_{zz} \\ &= 1-\frac{3}{2}p_z A_y(\theta)\Delta\beta(\cos\phi'-\Delta\phi\sin\phi') \\ &\quad +p_{zz}A_{xz}(\theta)\Delta\beta(\sin\phi'-\Delta\phi\cos\phi')+\frac{1}{2}p_{zz}A_{zz} \end{aligned} \tag{4.25}$$

Taking the combination $L + R$ gives

$$A_{zz}+\Delta A_{zz} = \frac{L+R-2}{p_{zz}} \tag{4.26}$$

which is free from the effect of the first-order spin misalignments. The analyzing power A_{zz} can also be calculated using only one detector,

$$\begin{aligned} A_{zz}-\Delta A_{zz} &= \frac{1}{p_{zz}}\Big(R-1-3p_z A_y\Delta\beta(\cos\phi'-\Delta\phi\sin\phi') \\ &\quad +2p_{zz}A_{xz}\Delta\beta(\cos\phi'-\Delta\phi\sin\phi')\Big) \\ A_{zz}+\Delta A_{zz} &= \frac{1}{p_{zz}}\Big(L-1+3p_z A_y\Delta\beta(\cos\phi'-\Delta\phi\sin\phi') \\ &\quad -2p_{zz}A_{xz}\Delta\beta(\cos\phi'-\Delta\phi\sin\phi')\Big). \end{aligned} \tag{4.27}$$

Expressions for A_{zz} calculated from individual detectors will have errors due to the spin misalignment, but by averaging the left and right detectors spin misalignments will cancel.

4.2.3 Finite-solid-angle corrections

The angular opening of the detector apertures can lead to a blurring effect on the shape of the angular distribution which will be most sensitive to distributions that depend strongly on angle. To estimate this effect, the angular distribution was calculated by taking into account the finite geometry of the detector collimators and using the known relationships for a pure $\frac{3}{2}^+$ S-wave resonance in the ^{3}He$(d,p)^4$He reaction. The setup used for the different measurements is summarized in Table 4.1 where $\Delta\theta$ corresponds to half of the angular acceptance of the detector. The calculations show that the angular opening has a negligible effect on these analyzing powers ($\leq 0.3\%$).

4.2.4 Other sources of error

An error arises from the detectors being placed asymmetrically about the beam direction. The misplacement of the detectors is estimated to be no larger than 2° , based on zero-crossing measurements [Bla95] done in the high-voltage chamber while studying the D(p,p)D reaction. This error is found to be small for all the analyzing powers and can be neglected.

There is also a systematic error due to uncertainty in the determination of the beam polarization. This error is due to the fact that the polarimeters used in these measurements were calibrated based on measurement made at tandem energies with a ^{3}He$(d,p)^4$He polarimeter [Ton81]. The errors are estimated to be 4.3% for the tensor polarimeter and 3.7% for the vector polarimeter, as discussed in Appendix A.

4.3 Cross section

4.3.1 Relative angular distributions

The measurement of the relative angular distributions consisted of taking a ratio of the counts in the movable detectors to the counts in the fixed-angle monitor detectors. Corrections were taken into account for problems such as the rotating detectors having different solid angles and, for some angle settings when the target rod was rotated, one of the fixed-angle monitor detectors was blocked. To correct for the different solid angles of the rotating detectors, the yield $Y(0°)$ defined as the ratio of the counts at 0° to the monitor counts was measured for each detector. The corrected relative yield $Y_c(\theta)$ was then computed as

$$Y_c(\theta) = \left(\frac{N(\theta)}{R_m + L_m}\right)\left(\frac{1}{Y(0°)}\right) \tag{4.28}$$

where $N(\theta)$ is the number of counts measured at θ and R_m and L_m are the counts in the right and left fixed-angle monitor detectors respectively. To correct for angles were one of the fixed-angle monitor detectors was blocked, the number of counts in the blocked detector was reconstructed using the ratio of counts between the right and left monitor detectors (a value previously determined) and the counts in the unblocked detector. Statistical errors were calculated which take these corrections into account.

4.3.2 Excitation function

The excitation function was made by taking the ratio of the counts in the detectors to the collected charge as determined by the BCI. This assumes that the target thickness did not change and that the beam integration is accurate at all energies. To correct for the target thickness loss, the ratio was remeasured several times throughout the experiment at the same beam energy. The loss of target thickness was determined as a function of the cumulative collected charge, which is the sum of the collected charge from all the previous runs including the

present run. The corrected yield $Y_c(E)$ at energy E is calculated by

$$Y_c(E) = \frac{N(E)}{P} + \left(\frac{N(E)}{P}\right) \times P_{cum} \times F \tag{4.29}$$

where $N(E)$ is the number of particles detected at energy E, P is the number of integrator pulses from the BCI for one run, P_{cum} is the sum of all the integrator pulses from all the previous runs including the present run, and F is a factor that depends on the loss of target thickness. The value of F is obtained by plotting P_{cum} versus the uncorrected yield, $N(E)/P$ for the measurements taken at the same energy throughout the experiment. The slope of this graph is just the F factor and is related to the thickness loss per integrator pulse.

The differential cross sections were converted to center-of-mass values so that the total cross section could be calculated by integrating the differential cross section data. Since the excitation function data was measured at only one angle, the previously measured relative angular distributions were used to calculate the shape of the angular distributions at the energies where the excitation function was measured. Each distribution was fit with Legendre polynomials and the expansion coefficients were fit versus energy. This allows one to easily calculate the shape of the relative angular cross section at any energy. The relative angular cross section calculations were scaled to the corrected-yield measurements and then integrated over the angular distribution to determine the total cross section. All the excitation function cross sections were then scaled to the absolute cross section measurement described in the next section.

4.3.3 Absolute cross section

In order to determine an absolute cross section, the target thickness needs to be known. The target thickness was found using the D(d,p)T reaction at an energy where the cross section is known with good accuracy from measurements by Brown and Jarmie [Bro90]. In this work coefficients from a least-squares fit to the data from [Bro90] were used to determine the differential cross section at

the reaction energy. Using the known $\partial\sigma/\partial\Omega$, the number of detected protons from the D(d,p)T reaction N_p, and the number of incident deuterons N_i, the target thickness times solid angle $t\Delta\Omega$ is easily determined from

$$t\Delta\Omega = \frac{N_p}{(N_i)(\partial\sigma/\partial\Omega)}. \tag{4.30}$$

Once the target thickness is determined, the absolute cross section for both the D(^{3}He,p)^{4}He and D(^{3}He,^{4}He)p reactions can be found from

$$\frac{\partial\sigma}{\partial\Omega} = \frac{N_p}{(N_i)(t\Delta\Omega)} \tag{4.31}$$

where N_p is the number of detected particles, N_i is the number of incident ^{3}He particles, and $t\Delta\Omega$ is already determined from equation 4.30. Since the statistical error is very small ($< 0.2\%$) the uncertainty is due exclusively to systematic errors. This is estimated to be 4.3% by adding the following errors in quadrature. There is a 1.3% scale error in the D(d,p)T cross section data as quoted by [Bro90]. A 3.0% error arises in the calculation of the D(d,p)T cross section due to uncertainties in interpolating in energy and angle from the least-squares fit to the data. An uncertainty of the reaction energy leads to a 2% error. A 2% error is estimated in the beam integration because effects such as the beam hitting different spots on the target and/or leakage current from the battery used for electron suppression.

4.4 Reaction energies

To determine the average reaction energy, one needs to know both the beam energy and the loss of beam energy in the target. Both the minitandem and high-voltage chamber potentials were calibrated to the digital volt meter (DVM) readings in the TUNL control room [Bru95a, Bru95b]. The high-voltage chamber was calibrated with several resonances in the ^{19}F$(p,\alpha\gamma)$ reaction and the minitandem was calibrated using resonances in both the ^{19}F$(p,\alpha\gamma)$ and ^{27}Al(p,γ)

E_d (keV)	E_{loss} (keV)	E (keV)
69	9	60
108	9	99
206	7	199
429	5	424
645	4	641

Table 4.2: Summary of beam energy, energy loss, and average reaction energy for ion-implanted ^{3}He targets. The error on E is 2.2 keV

reactions. The beam energy is easily calculated to 1 keV using the DVM readings of both the minitandem and high-voltage chamber, the source and cesium oven voltages, and the minitandem-foil thickness. Details of the calibration are given in [Bru95a, Bru95b]. To calculate the average reaction energy, one needs to subtract any energy lost in the ion-implanted ^{3}He target or in the deuterated carbon target.

4.4.1 Energy loss in ion-implanted ^{3}He targets

To calculate the energy loss in the ion-implanted targets, the Monte Carlo simulation code TRIM (Transport and Ranges of Ions in Matter [Bie80]) was used. First, the average implant depth had to be determined. This was calculated for 17-keV ^{3}He ions in Ta and was found to be 0.044 μm. Next, the average energy that a deuteron would lose in 0.044 μm of tantalum[7] was calculated using stopping powers from Anderson [And77] and also TRIM calculations. The two calculations agreed reasonably well and the results for the five energies that data were taken are given in Table 4.2. The TRIM calculations also indicate that the energy straggling over the implant range is around 2 keV.

[7] A deuteron beam traveling through these targets will also encounter an energy loss due to the ^{3}He implanted in the target. From TRIM calculations this energy loss is negligible compared to the energy loss in tantalum.

4.4.2 Energy loss in deuterated carbon targets

The energy loss in the deuterated carbon targets was determined experimentally. This was accomplished by measuring deuteron or ^{3}He elastic scattering from the aluminum backing using back-angle monitor detectors. An energy calibration for the monitor detector spectra was obtained by measuring elastic scattering off of a plain aluminum target at several different beam energies. The energy loss in a deuterated carbon layer was determined by measuring the end point energy of the elastically scattered particles for a plain aluminum target and a deuterated carbon target at the same energy. The difference in this energy is the sum of the beam losing energy traveling through the deuterated carbon layer and the elastically scattered particles losing energy traveling out. A typical spectrum for both a plain aluminum target and an aluminum target with a deuterated carbon layer is shown in figure 4.1. The average energy loss is taken to be one fourth of the energy difference. This procedure assumes that the stopping power is the same for the incoming particle as for the scattered particle, an approximation that does not result in a significant error. For a deuteron beam at $E_d = 116$ keV the energy loss is between 2 and 5 keV and for a ^{3}He beam at $E_{\mathrm{He}} = 651$ keV the energy loss is between 6 and 15 keV, depending on the target thickness.

4.5 Wien filter calibration

A Wien filter calibration was done for A_{xz} and A_{zz} measurements, which required the spin-quantization axis in the reaction plane. The settings of the Wien filter for the spin perpendicular to the reaction plane (A_y and A_{yy} measurements) were already calibrated for the 52° chamber and are the same for the high-voltage chamber. The calibration was done by scanning the magnetic field in the Wien filter while monitoring the quantity $L - R$. The magnitude of this quantity will be maximum for $\beta = \pm 45°$ and will be zero for $\beta = 0°$. The measured values

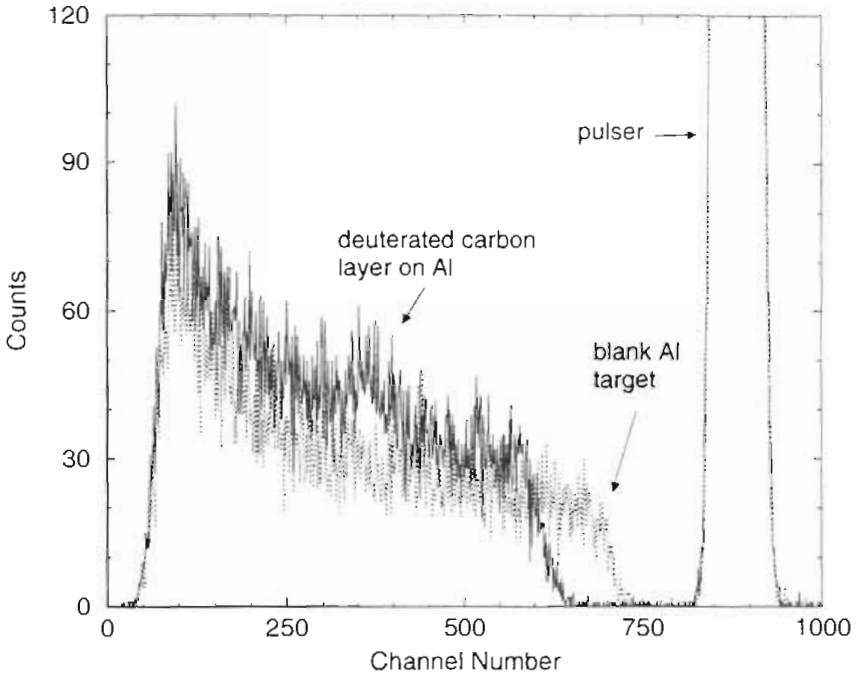

Figure 4.1: Typical monitor spectrum of deuteron elastic scattering off a deuterated carbon target on an aluminum backing (solid line) and off an aluminum target (dotted line). The difference between the end points of the two spectra is due to the energy loss of the particle traveling through the deuterated carbon layer. The peak near channel 375 is due to the deuterated carbon layer.

were fit following the relationship

$$L - R = A \sin(a_0 I - a_1) \cos(a_0 I - a_1) \tag{4.32}$$

where A is a scale factor, I is the Wien filter current, and $\beta = a_0 I - a_1$. The Wien filter scan and fit to the data are shown in Figure 4.2 and the Wien filter settings are shown in Table 4.3.

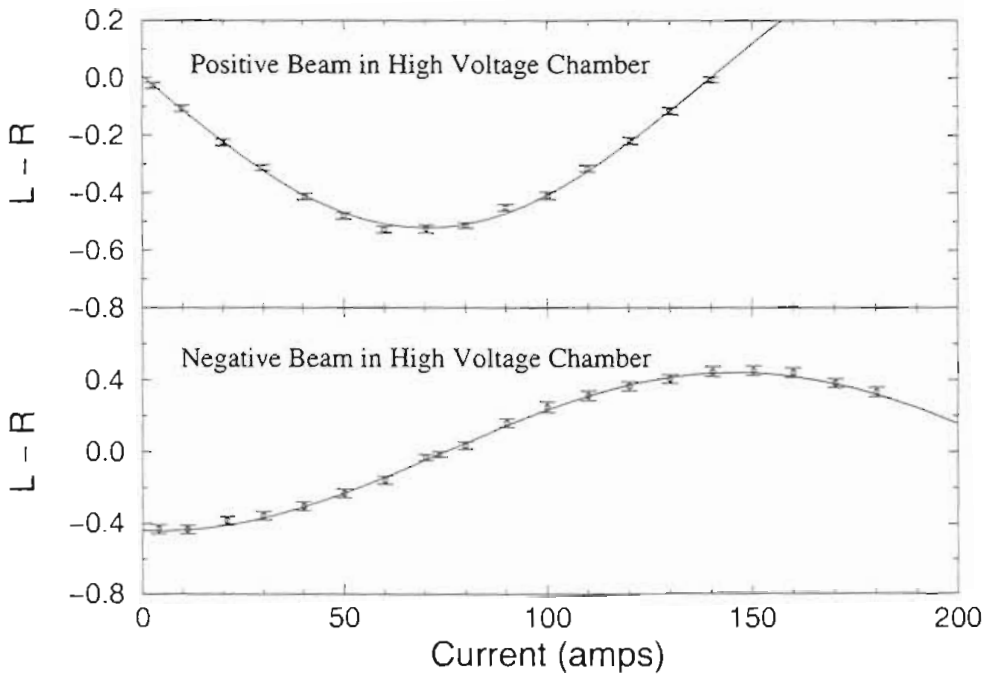

Figure 4.2: Wien filter calibration for both positive and negative beams in the high-voltage chamber. The solid line is the best fit to the data using equation 4.32.

β	I (A)	B (G)
positive beam		
-45°	-69.23	-963.1
0°	0.46	-5.2
+45°	70.15	952.7
negative beam		
-45°	145.71	-1971.2
0°	74.95	-1011.4
45°	4.20	-51.66

Table 4.3: Wien filter settings for both positive and negative beams in the high-voltage chamber.

Chapter 5

Results

5.1 Analyzing power measurements

The angular distributions of A_y, A_{yy}, A_{xz}, and A_{zz} are shown in Figures 5.1 to 5.4, along with the calculations derived from the assumption of a $\frac{3}{2}^+$ S-wave resonance, equations 1.1 to 1.4. The data are tabulated in Appendix B. The vector analyzing power, A_y, which should be equal to zero for a pure S-wave resonance, is very small and slightly backward peaked at all measured energies. The analyzing power A_{yy} has some angular dependence and is closest to being isotropic and equal to $\frac{1}{2}$ near the resonance and deviates from this value by no more than 10%. The analyzing power A_{xz} has slightly different magnitudes at all energies and is of a different shape at the highest energy, while A_{zz} appears to have a tilt and deviates from the single resonance calculations at forward and backward angles. All the analyzing powers deviate from the pure S-wave resonance relationships and this is an indication that contributions from other entrance channels are important.

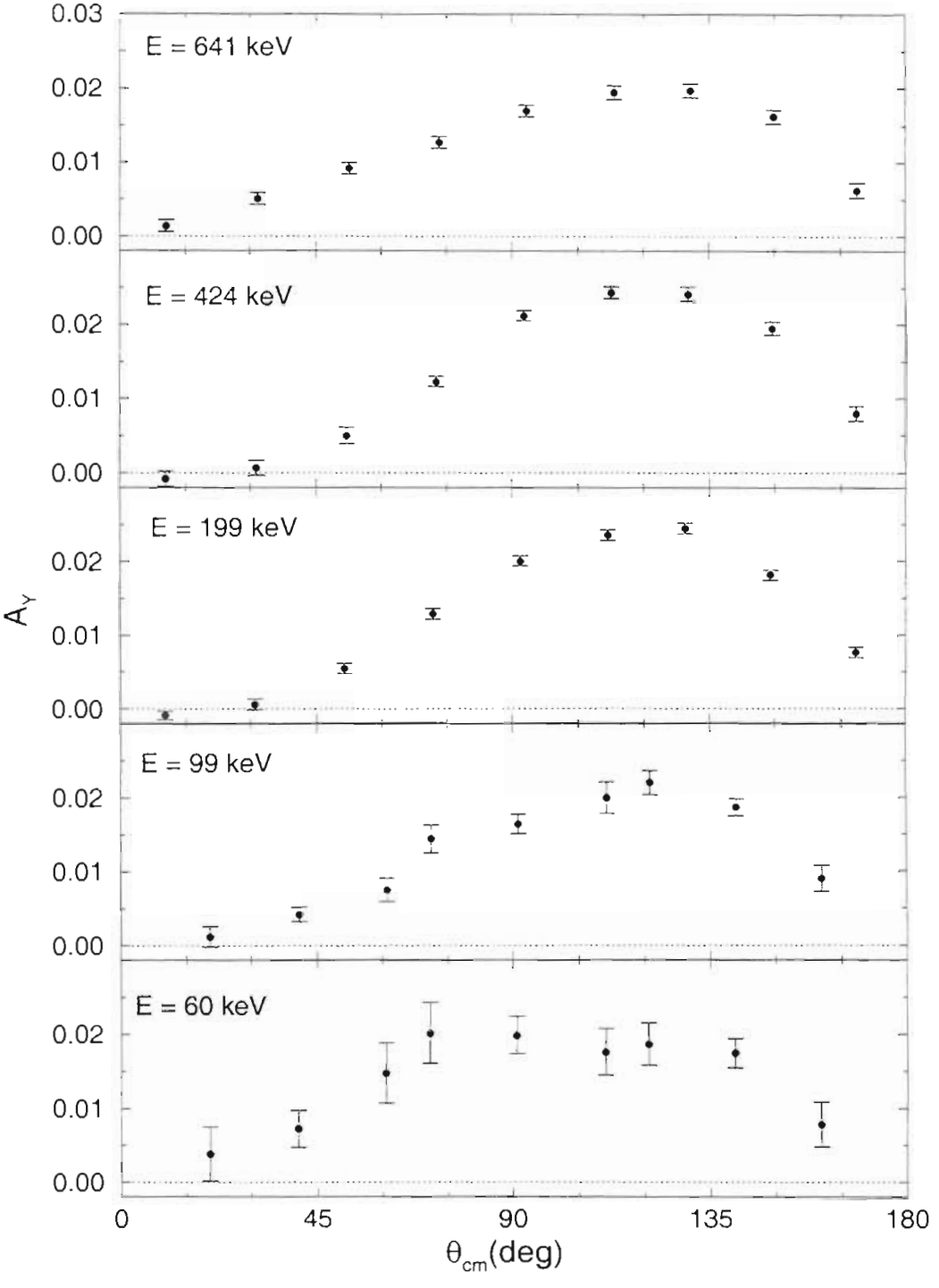

Figure 5.1: Graph of the A_y data (circles) and the assumption of a $\frac{3}{2}^+$ S-wave resonance (dotted line) given by equation 1.1. The error bars shown include statistical errors only.

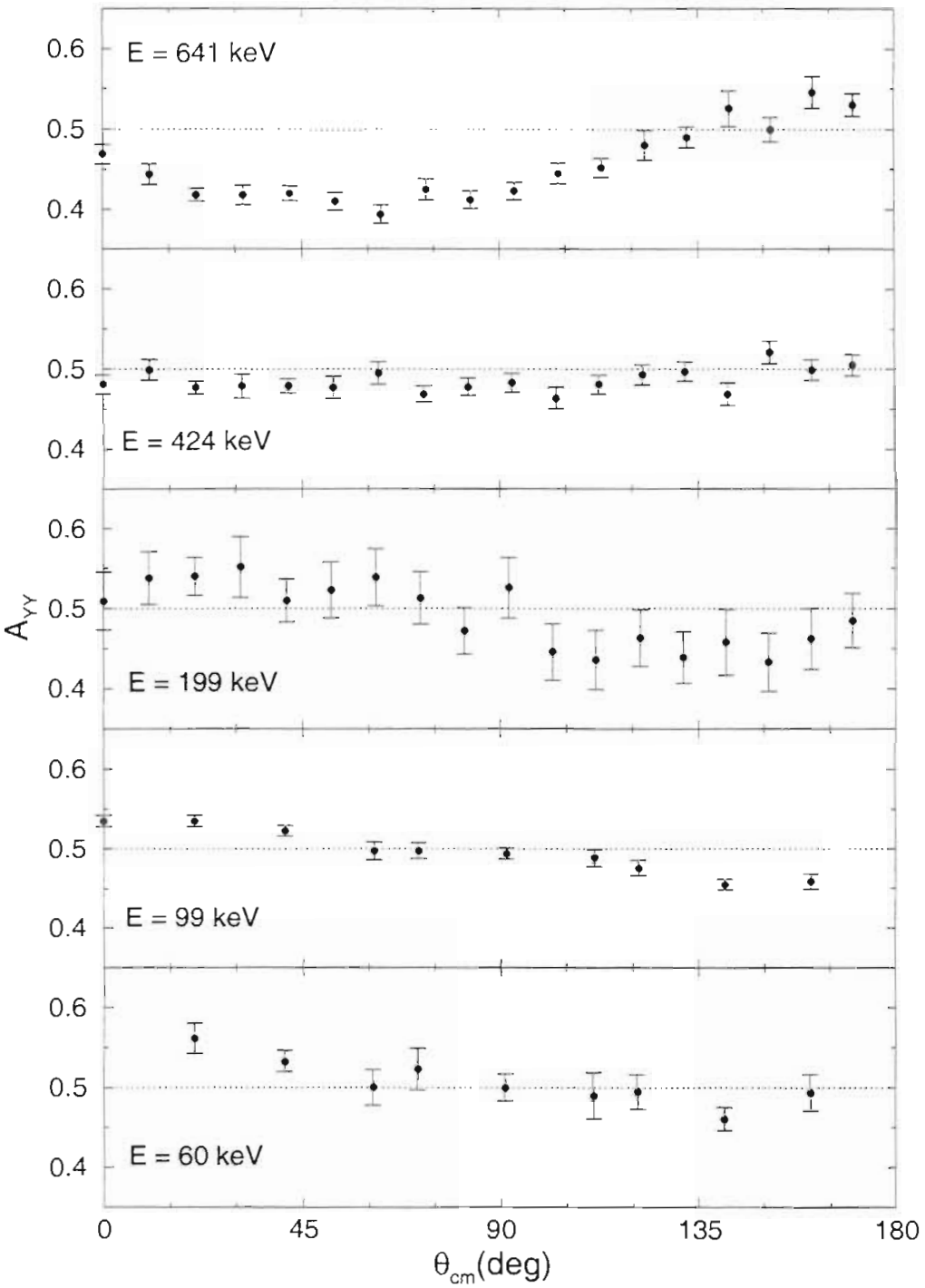

Figure 5.2: Graph of the A_{yy} data (circles) and the assumption of a $\frac{3}{2}^+$ S-wave relationship (dotted line) given by equation 1.2. The error bars shown include statistical errors only.

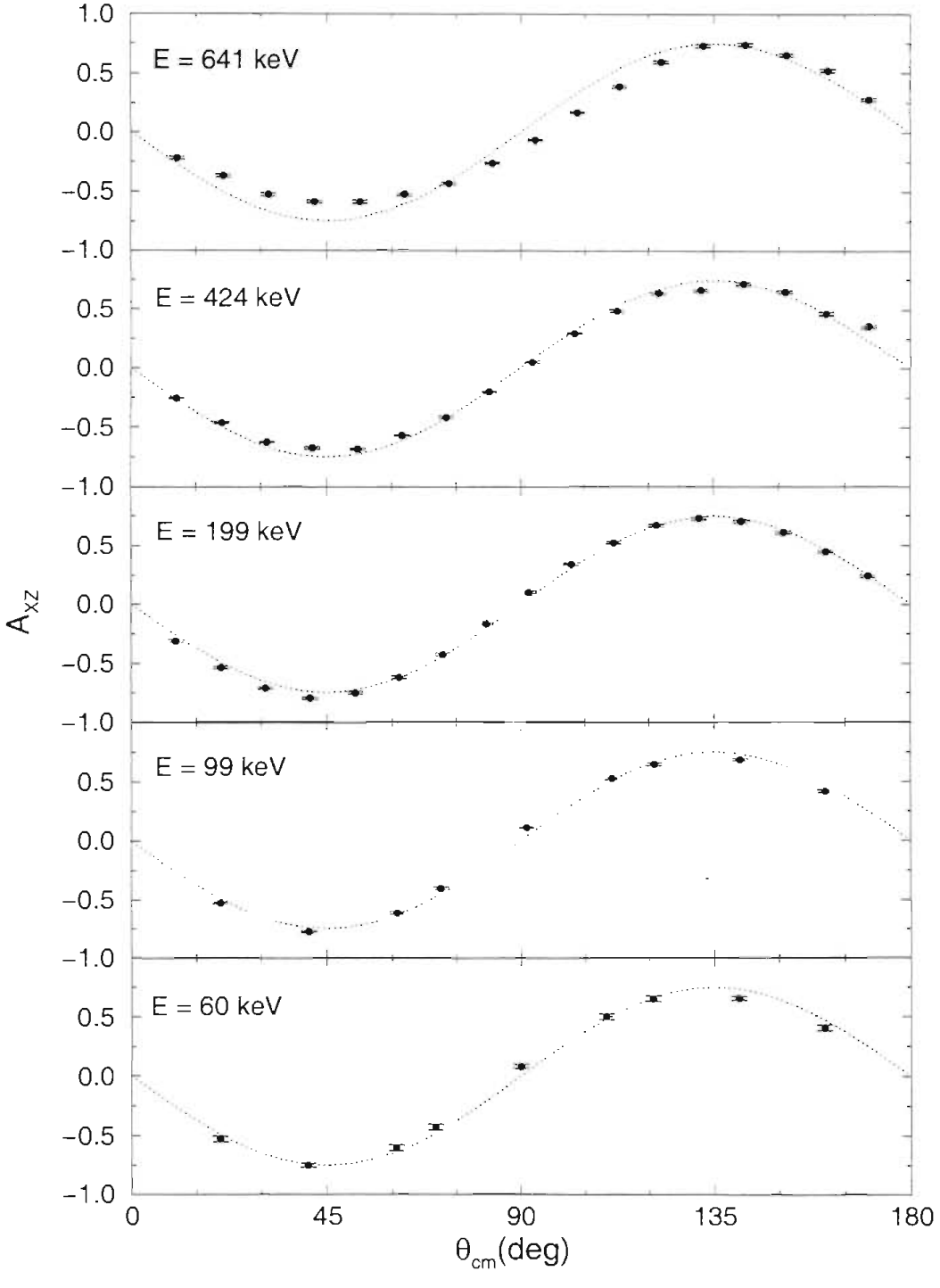

Figure 5.3: Graph of the A_{xz} data (circles) and the assumption of a $\frac{3}{2}^+$ S-wave relationship (dotted line) given by equation 1.3. The error bars shown include statistical errors only.

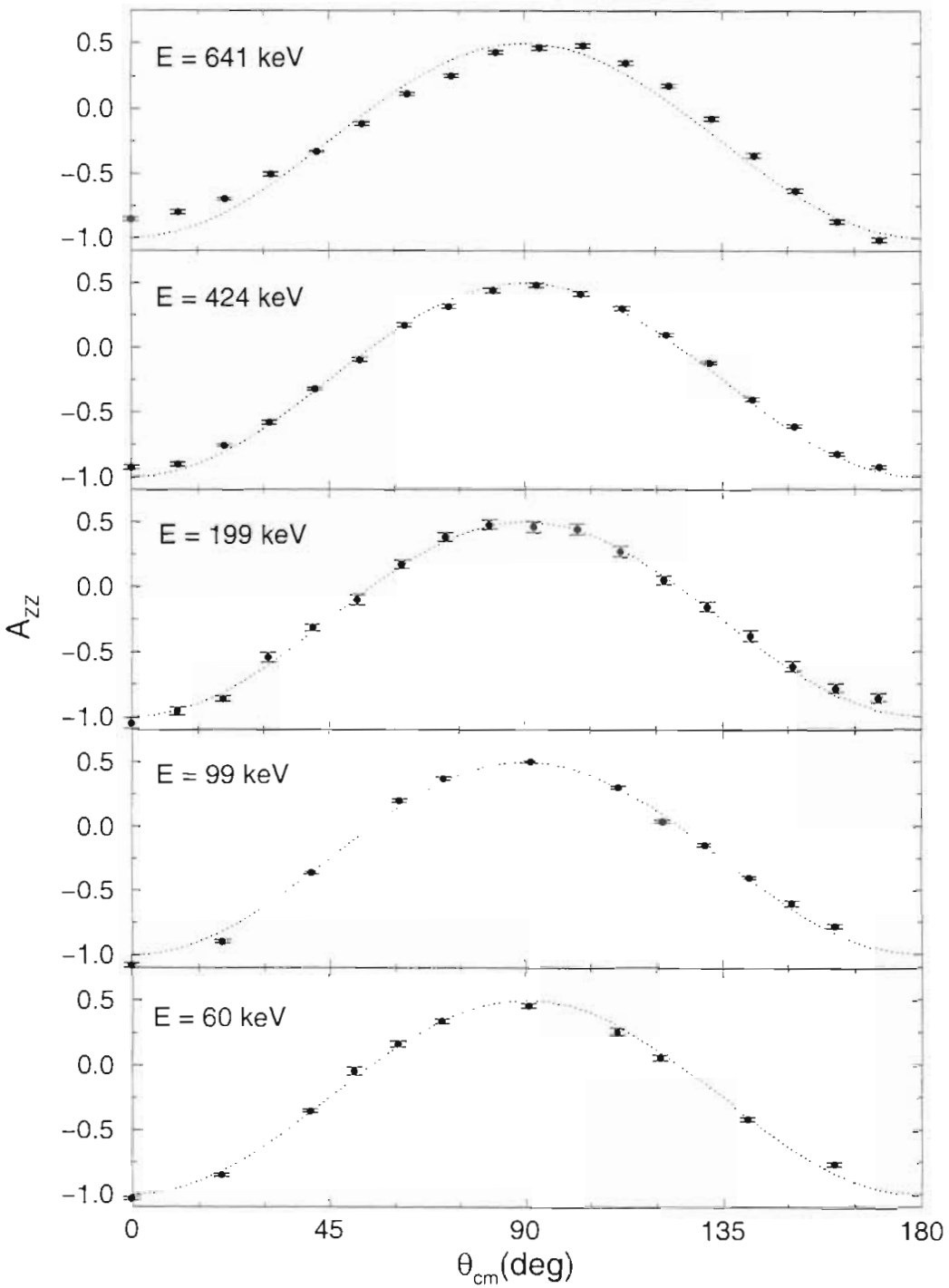

Figure 5.4: Graph of the A_{zz} data (circles) and the assumption of a $\frac{3}{2}^+$ S-wave relationship (dotted line) given by equation 1.4. The error bars shown include statistical errors only.

5.2 Cross section measurements

The results of the relative cross section measurements are shown in Figure 5.5. The differential cross sections are nearly isotropic at the lowest energies and become forward peaked at the higher energies. The excitation function, which was normalized at the resonance to the absolute cross section measurement, is shown in Figure 5.6 and the absolute cross section result is shown in figure 5.7 along with the normalized cross section angular distributions taken at $E = 424$ keV. The total cross section, which was calculated by integrating over angle the differential cross section, is 777 ± 33 mb. This error contains the systematic errors discussed in Section 4.3.3.

5.3 Comparison of the present data with previous data

5.3.1 Comparison of analyzing powers

Garrett and Lindstrom [Gar74] measured complete sets of analyzing powers at three energies, $E = 344$, 465, and 727 keV. Since none of these energies matches the current measurements, comparison is not straight forward, but clear trends in the data can be seen in Figures 5.8 to 5.11. The figures show the data plotted in order of increasing energy. The solid lines are obtained assuming a $\frac{3}{2}^+$ S-wave resonance, equations 1.1 to 1.4, and are included to guide the eye to the trends of the data. Also included is the $E = 1$ MeV data obtained by Bittcher *et al.* [Bit90].

These figures reveal some interesting points about the data. The A_y data of the present work have been measured to a much greater precision than any of the existing data. Also, the magnitude of the A_y data at the lower energies is smaller by about 15% than the previously obtained data. The A_{yy} data are consistent

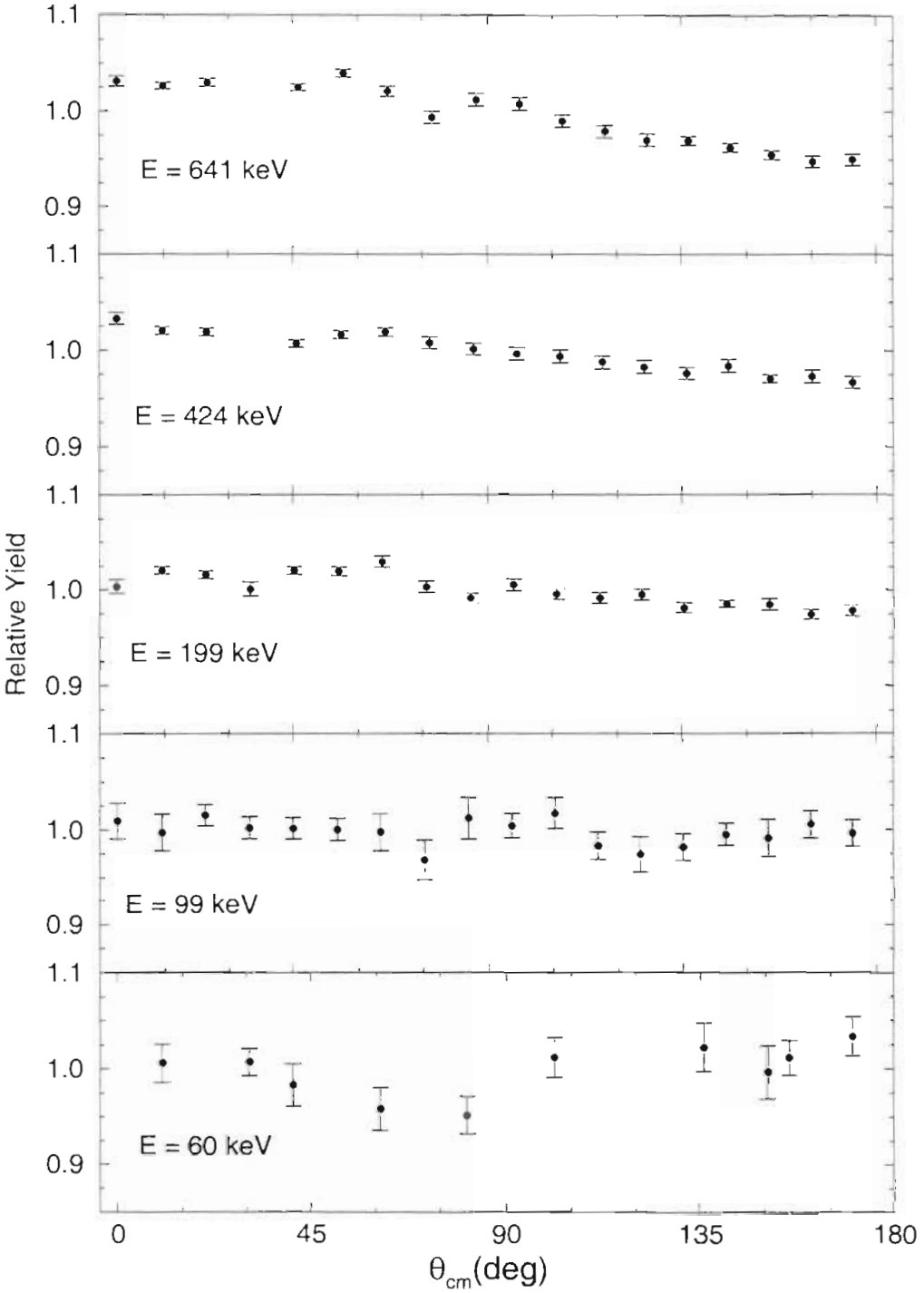

Figure 5.5: Graph of the relative cross section data (circles). For a reaction proceeding through a $\frac{3}{2}^+$ S-wave resonance the cross section should be isotropic. The error bars shown include statistical errors only.

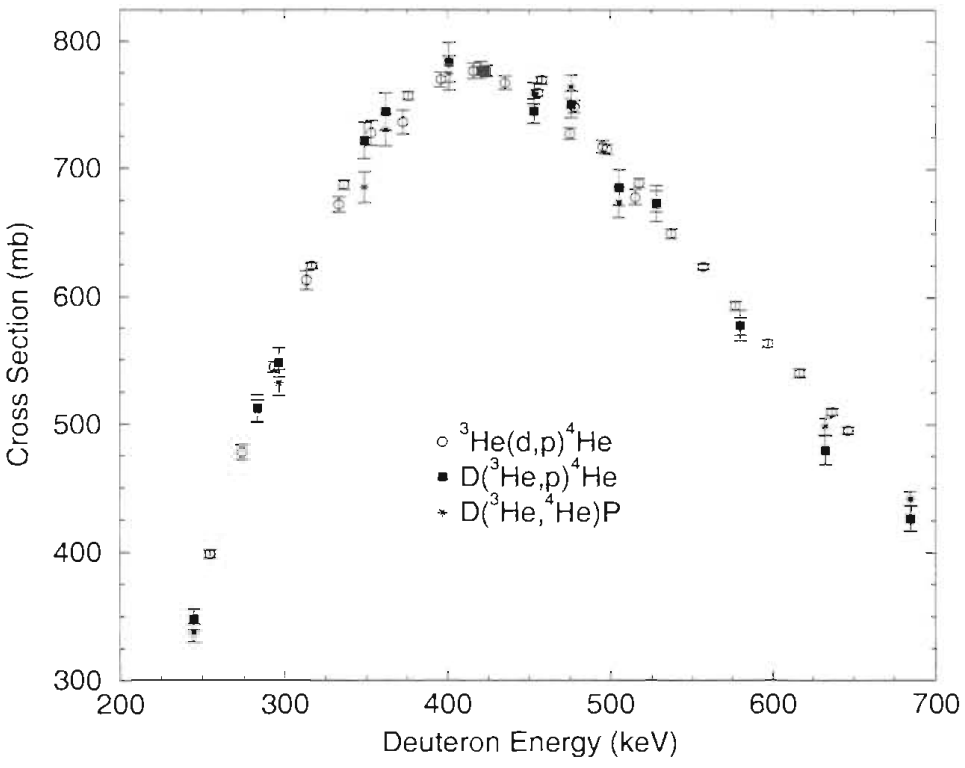

Figure 5.6: Excitation function of the cross section using the ^{3}He$(d,p)^4$He reaction (open circles), D$(^3$He$,p)^4$He reaction (solid squares), and the D$(^3$He$,^4$He)p reaction (stars). All data is in the ^{3}He$(d,p)^4$He reaction frame. Note that both axes are offset. The error bars shown include statistical errors only.

with the previous data. The A_{xz} data also look consistent with the exception of the $E = 465$ keV data set. The minimum in these data near 45° appears to dip lower than the trend and the maximum near 135° appears to be larger than the trend of the other data sets. The A_{zz} data at $E = 465$ and 727 keV appear to be inconsistent with the trend of the data. At these energies the data at backward angles appear to drop off much faster than the other data sets.

Leemann *et al.* [Lee71] measured a complete set of analyzing powers at $E =$ 430 keV. In Figure 5.12 the analyzing powers taken at $E = 424$ keV are shown along with the data of Leemann *et al.* The data sets agree well, with the exception

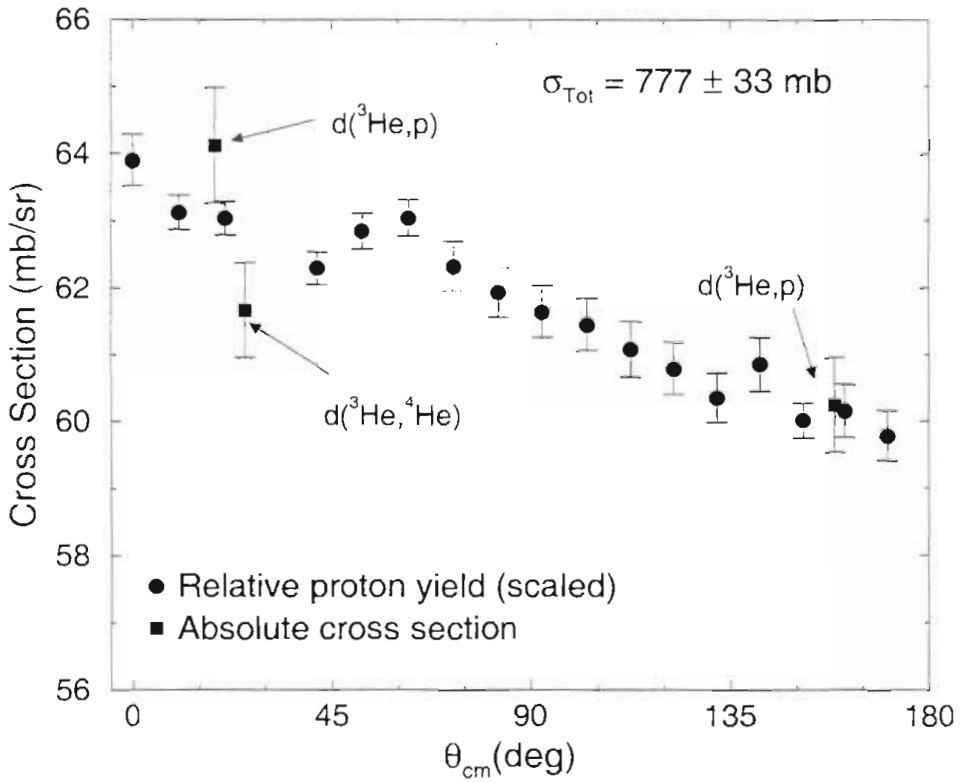

Figure 5.7: Graph of the absolute cross section data (squares) at an energy $E_d = 426$ keV corresponding to the ^{3}He$(d,p)^4$He reaction and the relative cross section data (circles) at $E_d = 424$ keV normalized to the absolute cross section data. Note that the y axis is offset from zero.

that the present A_{yy} data appear to be lower in magnitude and the A_{xz} data have a different minimum value around 45°.

5.3.2 Comparison of the cross-section data

There have been many measurements of relative angular cross section distributions at energies below 1 MeV, see Table 1.3. These have been made to an energy as low as 25 keV and are compared with the current measurement in Figures 5.13 and 5.14. The data show that the cross section is isotropic at the very low energies and becomes forward peaked at the higher energies.

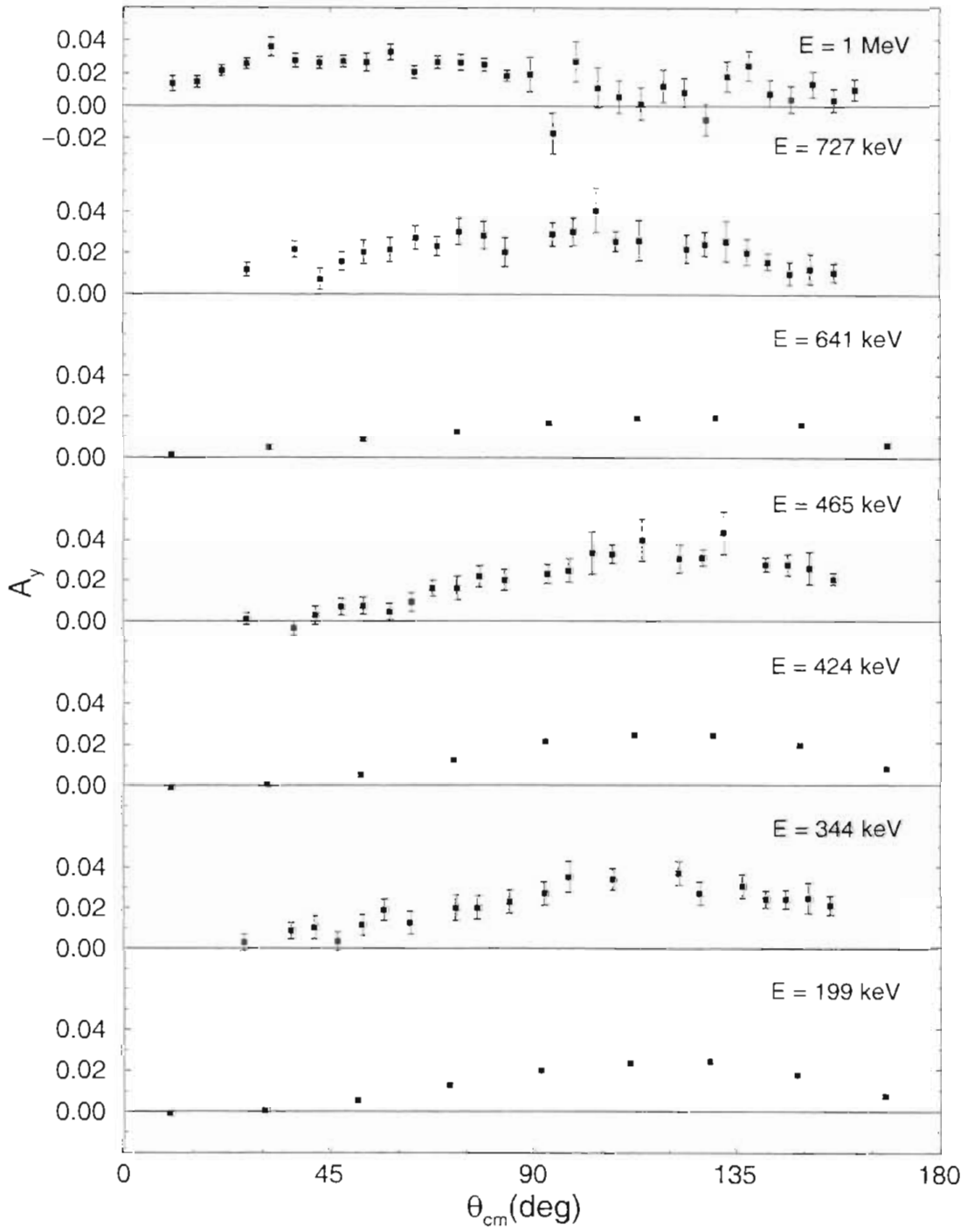

Figure 5.8: Comparison of the A_y data at 199, 424, and 641 keV with the data of Garrett [Gar74] at 344, 465, and 727 keV and the data of Bittcher [Bit90] at 1 MeV. The solid line is obtained assuming a $\frac{3}{2}^+$ S-wave resonance, equation 1.1, and is included to guide the eye to the trends of the data.

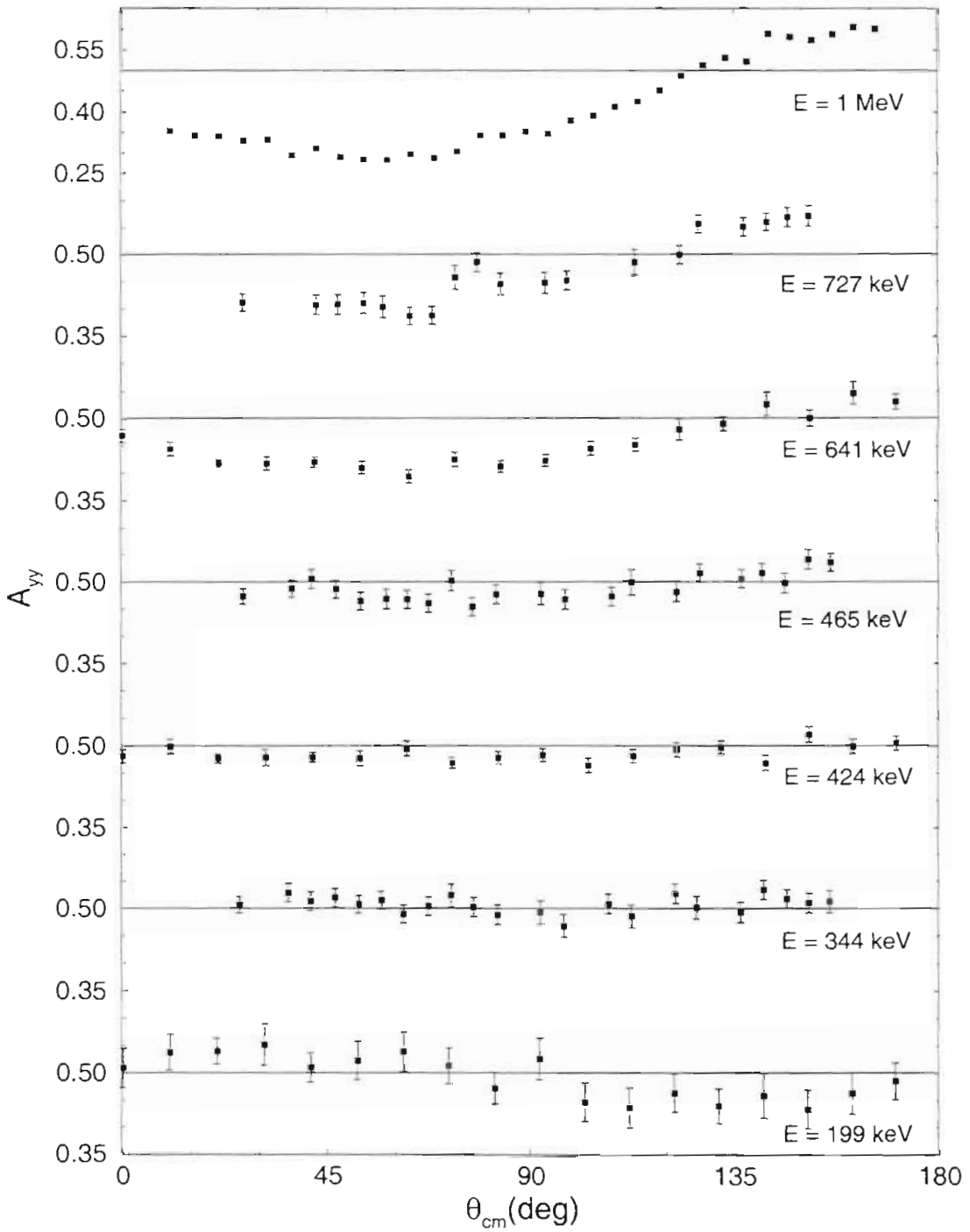

Figure 5.9: Comparison of the A_{yy} data at 199, 424, and 641 keV with the data of Garrett [Gar74] at 344, 465, and 727 keV and the data of Bittcher [Bit90] at 1 MeV. The solid line is obtained assuming a $\frac{3}{2}^+$ S-wave resonance, equation 1.2, and is included to guide the eye to the trends of the data.

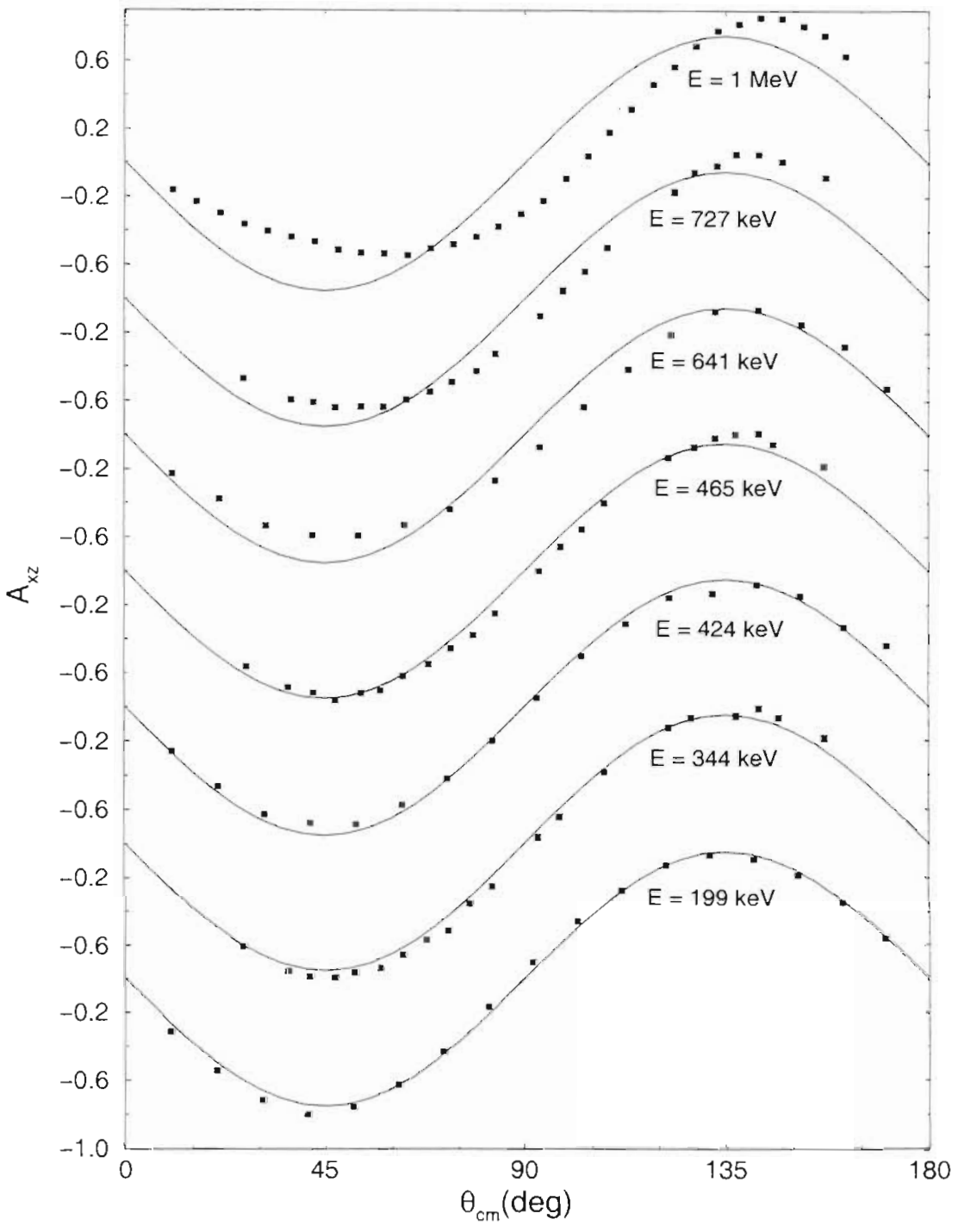

Figure 5.10: Comparison of the A_{xz} data at 199, 424, and 641 keV with the data of Garrett [Gar74] at 344, 465, and 727 keV and the data of Bittcher [Bit90] at 1 MeV. The solid line is obtained assuming a $\frac{3}{2}^+$ S-wave resonance, equation 1.3, and is included to guide the eye to the trends of the data.

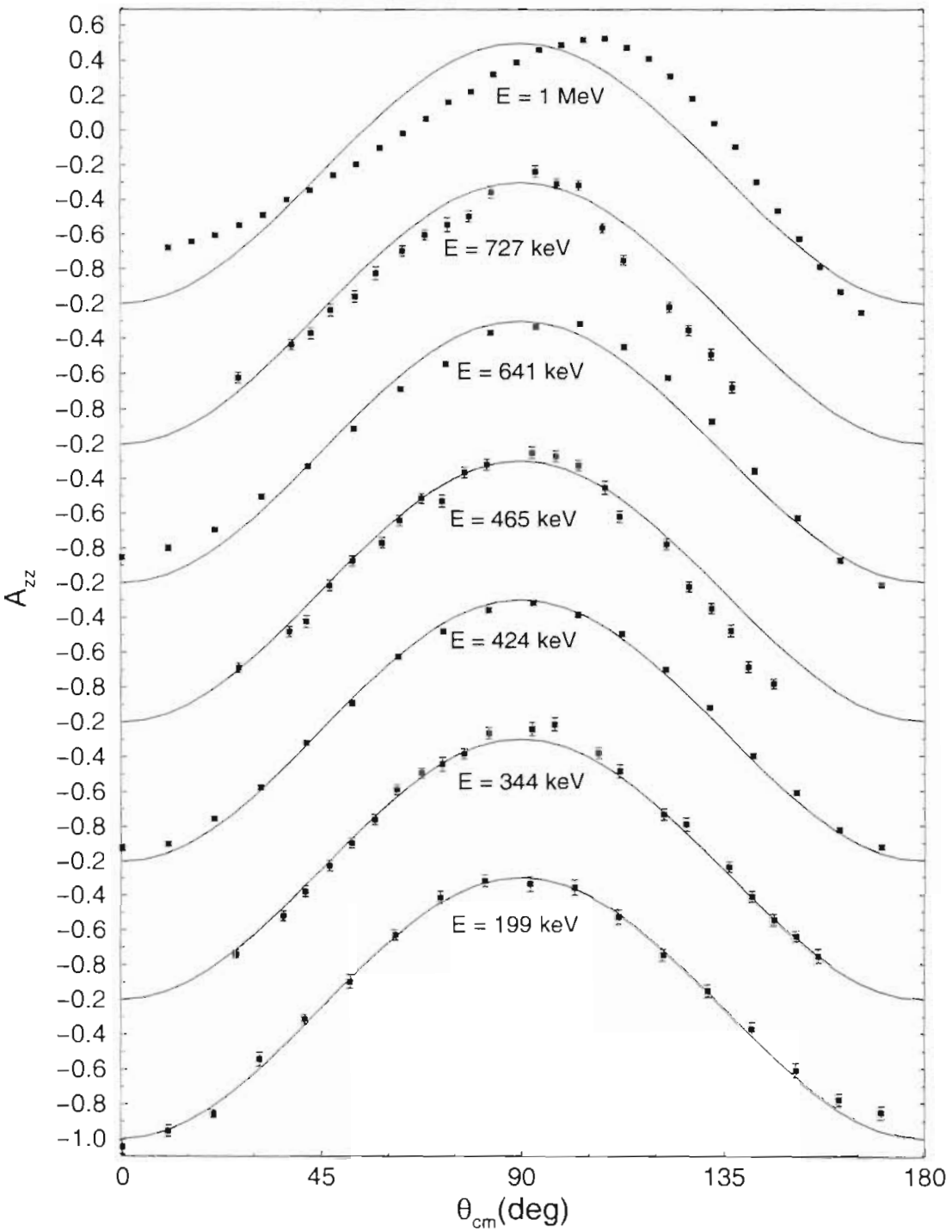

Figure 5.11: Comparison of the A_{zz} data at 199, 424, and 641 keV with the data of Garrett [Gar74] at 344, 465, and 727 keV and the data of Bittcher [Bit90] at 1 MeV. The solid line is obtained assuming a $\frac{3}{2}^+$ S-wave resonance, equation 1.4, and is included to guide the eye to the trends of the data.

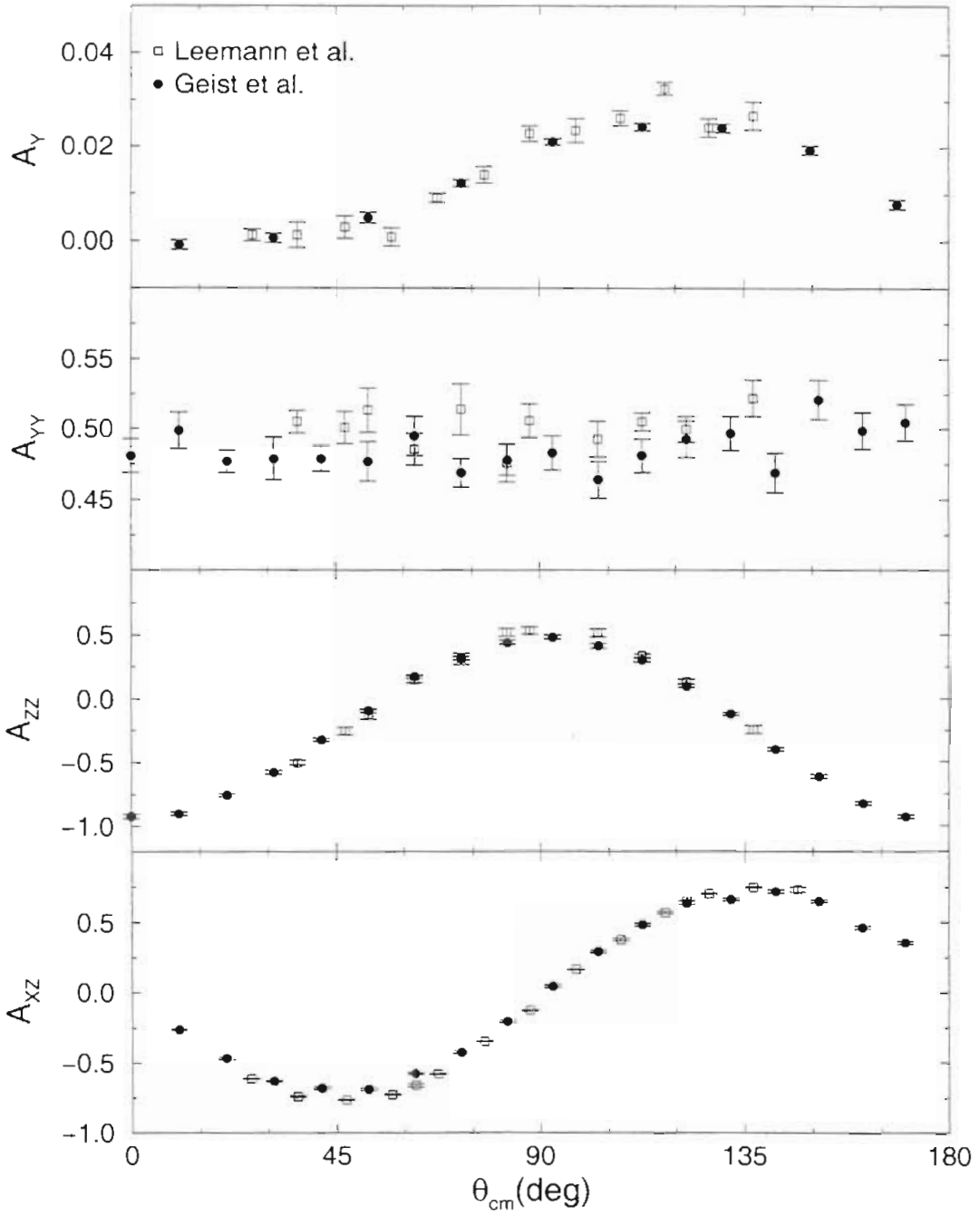

Figure 5.12: Comparison of the analyzing powers (solid circles) for this work at $E = 424$ keV with the data of Leemann *el al.* [Lee71] (open squares) at $E = 430$ keV.

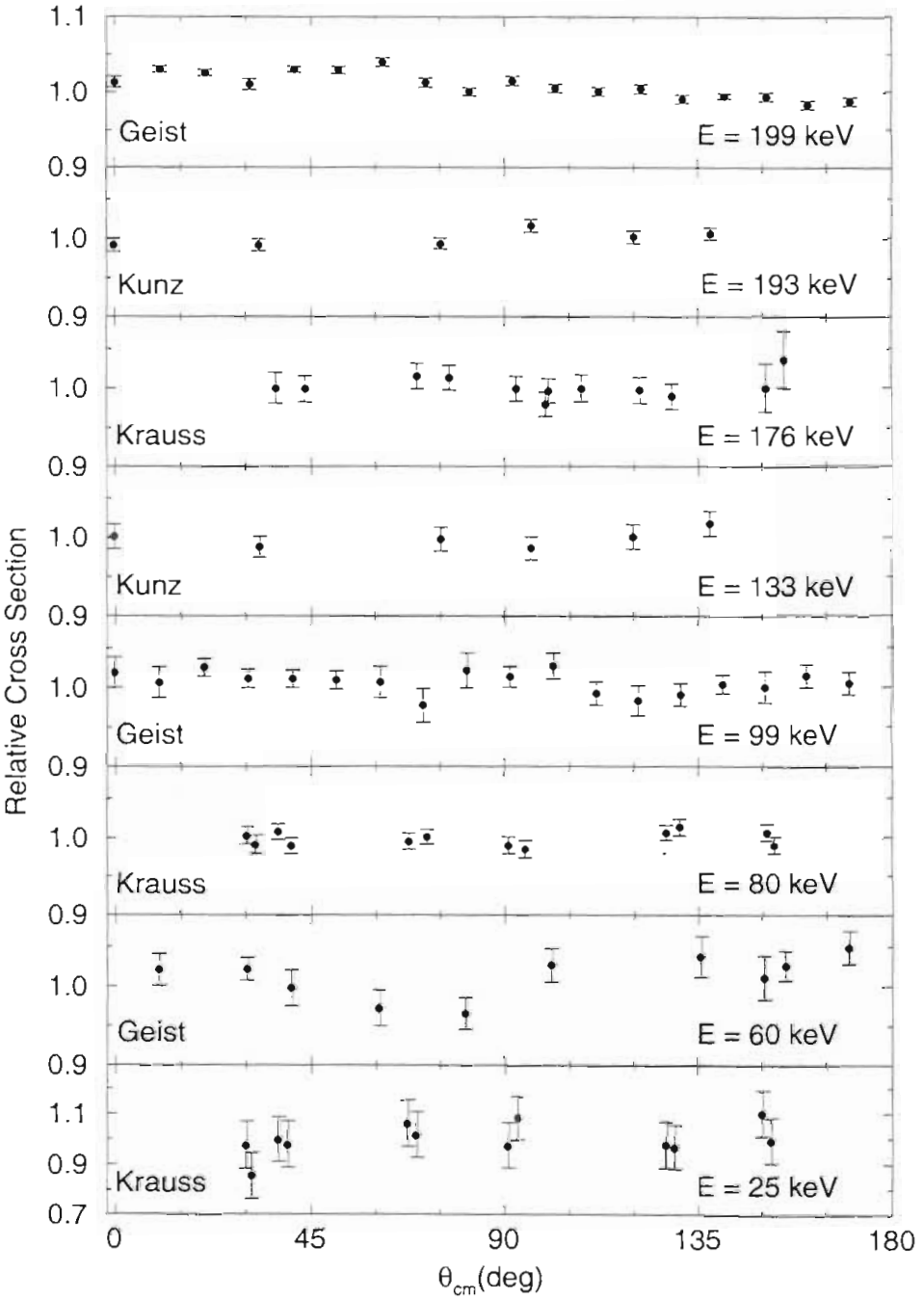

Figure 5.13: Comparison of the cross section angular distributions from 25 to 200 keV.

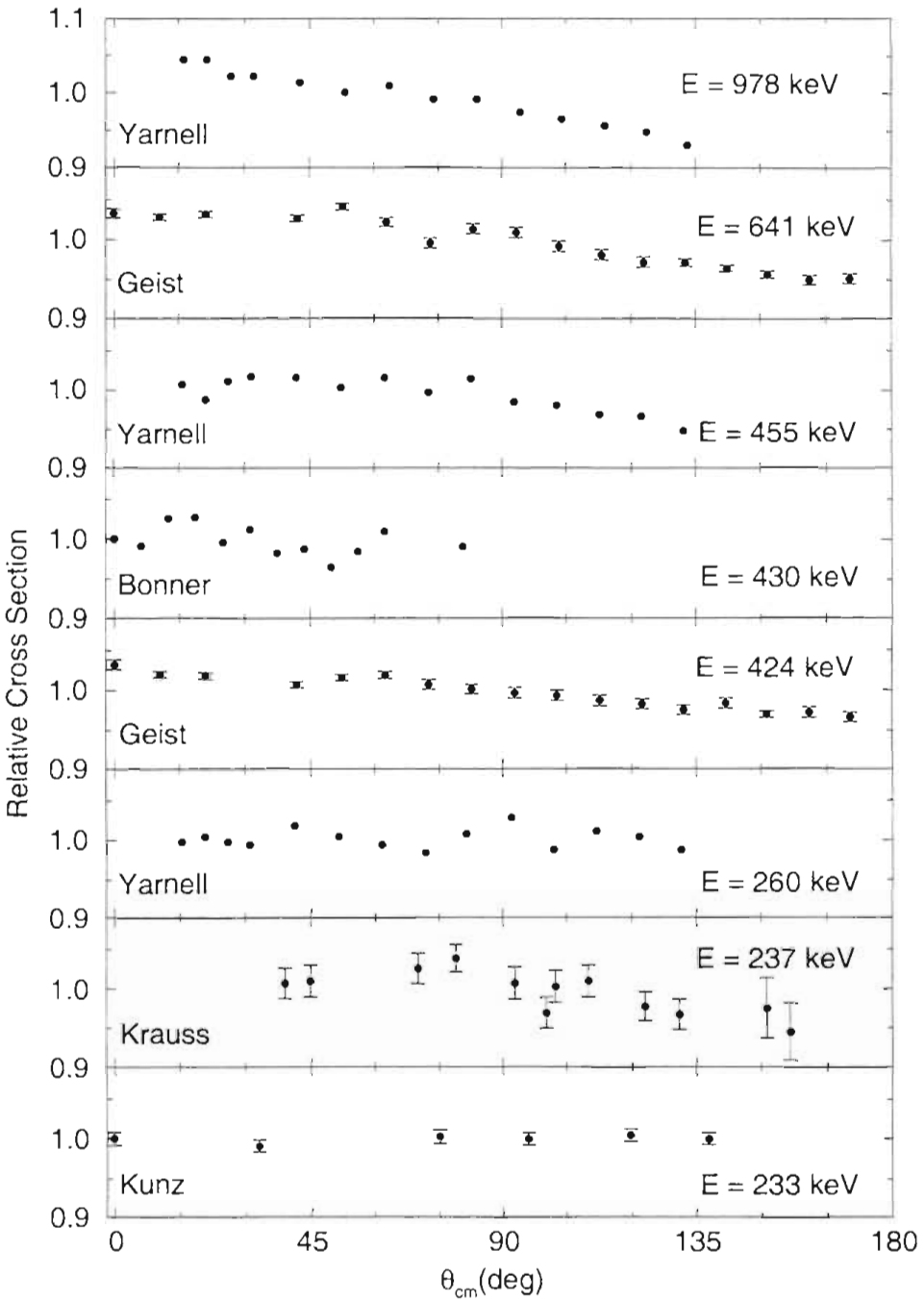

Figure 5.14: Comparison of the cross section angular distributions from 200 to 980 keV.

The shape of the excitation function data determined in the present work agrees with the most recent measurement by Möller and Besenbacher [Möl80]. Also, the lower-energy data overlap with the data of Krauss *et al.* [Kra87]. The absolute cross section result agrees within errors of the two most recent measurements by Möller and Besenbacher [Möl80] and Davies and Norton [Dav80], as seen in Table 1.2.

5.4 Legendre function fits

The analyzing powers were fit by the method of Seiler and Baumgartner [Sei70]. The quantities $C_{k,q}(\theta)$ are expanded as a sum of Legendre functions by

$$C_{k,q}(\theta, E) = \left(\frac{\lambda}{2\pi}\right)^2 \sum_L a_{k,q}(L, E) P_L^q(\cos\theta) \tag{5.1}$$

where the $P_L^q(\cos\theta)$ are associated Legendre functions as defined by Jahnke and Emde [Jah45] and the $a_{k,q}(L, E)$ are the expansion coefficients. The $\lambda/2\pi$ factor is the reduced de Broglie wavelength in the center of mass system

$$\frac{\lambda}{2\pi} = \frac{\hbar}{\sqrt{2\mu E_{cm}}} \tag{5.2}$$

where μ is the reduced mass. The $C_{k,q}(\theta)$ are related to the spherical tensor moments $T_{k,q}(\theta)$ by

$$C_{k,q}(\theta, E) = (2 - \delta_{q,0}) \begin{Bmatrix} 1 \\ -i \end{Bmatrix} \sigma_0(\theta, E) T_{k,q}(\theta, E) \quad \text{for } k = \begin{Bmatrix} \text{even} \\ \text{odd} \end{Bmatrix} \tag{5.3}$$

and the spherical analyzing powers are related to the Cartesian analyzing powers by

$$iT_{11} = \frac{\sqrt{3}}{2} A_y \tag{5.4}$$

$$T_{20} = \frac{1}{\sqrt{2}} A_{zz} \tag{5.5}$$

$$T_{21} = -\frac{1}{\sqrt{3}} A_{xz} \tag{5.6}$$

$$T_{22} = -\frac{1}{2\sqrt{3}} (A_{zz} + 2A_{yy}). \tag{5.7}$$

Fitting the analyzing powers in this fashion is useful because the expansion coefficients reveal information about the matrix elements contributing to the reaction [Sei70]. The matrix element in channel μ is defined as

$$R_\mu =< l'_\mu, S'_\mu, J^\pi_\mu | R | l_\mu, S_\mu, J^\pi_\mu > \tag{5.8}$$

where l_μ and S_μ correspond to the orbital angular momentum and channel spin in the entrance channel, l'_μ and S'_μ correspond to the exit channel, and J^π_μ is the total angular momentum and parity. The possible matrix elements including orbital angular momentum up to D waves are given in Table 1.1. The relation between the matrix elements and the expansion coefficients is given by

$$a_{k,q}(L,E) = \sum_{\mu,\nu \geq \mu} \alpha_{k,q}(L:\mu,\nu) \left\{ \begin{matrix} \mathrm{Re} \\ \mathrm{Im} \end{matrix} (R_\mu R^*_\nu) \right\} \quad \text{for } k = \left\{ \begin{matrix} \text{even} \\ \text{odd} \end{matrix} \right\} \tag{5.9}$$

where the coefficients $\alpha_{k,q}(L:\mu,\nu)$ are determined from angular momentum theory. These coefficients relate the incoming tensor moments to the outgoing tensor moments and some are given in [Sei70]. Around the resonance the matrix element that will contribute the most is the element that corresponds to the resonance, namely $R_1 =< 2, \frac{1}{2}, \frac{3}{2} | R | 0, \frac{3}{2}, \frac{3}{2} >$ and only interferences $(R_1 R^*_\nu)$ between this element and others need to be considered.

It is possible for a limited number of the quantities $U_\nu = \mathrm{Re}(R_1 R^*_\nu)$ and $V_\nu = \mathrm{Im}(R_1 R^*_\nu)$ to be determined from this type of analysis. A list of the matrix elements considered is given in Table 1.1. Assuming that only the matrix elements given in the table contribute to the reaction, a set of linear relationships between different $a_{k,q}(L,E)$ values can be obtained:

$$\frac{1}{2}\sqrt{6}a_{2,0}(2,E) + 2a_{2,1}(2,E) + a_{2,2}(2,E) = 0 \tag{5.10}$$

$$\sqrt{3}a_{2,0}(1,E) + \sqrt{2}a_{2,1}(1,E) = 0 \tag{5.11}$$

$$a_{2.0}(3,E) = -\frac{3}{4}\sqrt{6}a_{2.1}(3,E) = 3\sqrt{6}a_{2,2}(3,E). \tag{5.12}$$

Also, several of the real parts of the matrix elements, $U_\nu = \mathrm{Re}(R_1 R^*_\nu)$, can be explicitly solved for:

$$U_2 \;=\; 3\sqrt{2}a_{2,0}(2) + 6\sqrt{3}a_{2,1}(2) - 3a_{0,0}(0) \tag{5.13}$$

$$U_8 = \sqrt{3}[a_{2,1}(2) - 2a_{2,2}(2)] - \frac{3}{2}a_{0,0}(2) - \frac{3}{2}\sqrt{2}a_{2,0}(0) \quad (5.14)$$

$$U_{10} = -\sqrt{6}[a_{2,1}(2) + 2a_{2,2}(2)] - \frac{3}{2}\sqrt{2}a_{0,0}(2) - 3a_{2,0}(0) \quad (5.15)$$

$$U_{11} = \sqrt{3}[a_{2,1}(2) - 2a_{2,2}(2)] - \frac{3}{2}a_{0,0}(2) + \frac{3}{2}\sqrt{2}a_{2,0}(0) \quad (5.16)$$

$$U_3 + 2U_4 = 2\sqrt{3}a_{2,1}(1) + \frac{9}{2}\sqrt{3}a_{2,1}(3) - 3a_{0,0}(1) \quad (5.17)$$

$$U_3 - \sqrt{2}U_5 = 3a_{0,0}(1) - \frac{1}{2}\sqrt{3}a_{2,1}(3) - 3\sqrt{2}a_{2,0}(1). \quad (5.18)$$

The $U_{k,q}(\theta, E)$ values were determined from equation 5.3 by converting the Cartesian analyzing powers to spherical analyzing powers and using the relative cross section data along with the excitation function data. The Legendre functions fits were done as described in Bevington [Bev92] and the fit coefficients, $a_{k,q}(L, E)$, are given in Tables 5.1 and 5.2. The $a_{0,0}(L)$ coefficients[8] are obtained from fitting the cross-section data using $C_{0,0}(\theta) = \sigma_c(\theta)T_{0,0}(\theta)$, where $T_{0,0}(\theta) = 1$. As can be seen from the expansion coefficients, values of $L \leq 5$ were needed to fit the analyzing powers. As seen in the tables it is necessary to have odd L included in the fits. From the arguments given by Santos [San96], this is an indication that direct-reaction mechanisms may contribute to the reaction. This results from the fact that there is only one negative-parity level [Til98] located in ^{5}Li, a $\frac{3}{2}^-$ level located above the current energy range. P-wave contributions resulting from a channel with $J = \frac{1}{2}$ are likely to be the result of a direct process because there are no $\frac{1}{2}^-$ levels [Til98] in ^{5}Li in this energy range. The only possible way for these channels to contribute to the reaction would be through direct contributions interfering with the resonance contribution.

Using the fit coefficients, the relationships given in equations 5.10 to 5.12 can be compared at each energy. The overall agreement of the relationships was found to be fair, with the largest disagreement found to be at the highest energy, $E = 641$ keV. Agreement of the relationships is an indication that the assump-

[8]According to this definition the $a_{0,0}(0)$ coefficients are not equal to $\sigma_{tot}/4\pi$ as is often the case when fitting cross section angular distribution to Legendre functions.

	$E = 60$ keV	$E = 99$ keV
$a_{0,0}(0)$	3.101 ± 0.138	44.343 ± 1.925
$a_{0,0}(1)$	-0.034 ± 0.026	0.277 ± 0.209
$a_{0,0}(2)$	0.094 ± 0.040	0.221 ± 0.310
$a_{1,1}(1)$	-0.103 ± 0.007	-1.315 ± 0.049
$a_{1,1}(2)$	0.014 ± 0.004	0.374 ± 0.030
$a_{2,0}(0)$	-0.041 ± 0.014	0.135 ± 0.111
$a_{2,0}(1)$	0.027 ± 0.019	-0.487 ± 0.176
$a_{2,0}(2)$	-2.132 ± 0.026	-31.730 ± 0.234
$a_{2,0}(3)$	-0.166 ± 0.029	-2.600 ± 0.288
$a_{2,1}(1)$	-0.106 ± 0.032	-0.948 ± 0.190
$a_{2,1}(2)$	1.730 ± 0.022	25.204 ± 0.135
$a_{2,1}(3)$	0.114 ± 0.017	1.657 ± 0.098
$a_{2,1}(4)$	0.008 ± 0.016	0.125 ± 0.095
$a_{2,1}(5)$	0.001 ± 0.014	-0.114 ± 0.081
$a_{2,2}(2)$	-0.874 ± 0.007	-12.667 ± 0.045
$a_{2,2}(3)$	-0.020 ± 0.004	-0.289 ± 0.025
$a_{2,2}(4)$	-0.005 ± 0.003	0.039 ± 0.019

Table 5.1: Expansion coefficients for $C_{k,q}(\theta, E) = \lambda^2 \sum_L a_{k,q}(L, E) P_L^q(\cos\theta)$. Multiply all values by 10^{-3} for the cross section to be given in mb units.

tion of including only the matrix elements given in Table 1.1 is valid. The value of the real part of several matrix element combinations was calculated from equations 5.13 to 5.18 and are given in Table 5.3. The matrix element combination U_2 which includes the other possible S wave, the ${}^2S_{\frac{1}{2}}$ entrance channel, can be seen to be increasingly important at higher energies. The elements that include D waves in the entrance channel, U_8, U_{10}, and U_{11} can be seen to be small and close to zero at all energies. Information about the P waves can be obtained only through the combinations $U_3 + 2U_4$ and $U_3 - \sqrt{2}U_5$. Both of these indicate that

	$E = 199$ keV	$E = 424$ keV	$E = 641$ keV
$a_{0,0}(0)$	9.029 ± 0.389	76.005 ± 3.275	74.401 ± 3.206
$a_{0,0}(1)$	0.190 ± 0.017	2.047 ± 0.164	3.177 ± 0.185
$a_{0,0}(2)$	-0.034 ± 0.022	-0.265 ± 0.194	-0.797 ± 0.191
$a_{1,1}(1)$	-0.296 ± 0.005	-2.525 ± 0.050	-2.251 ± 0.050
$a_{1,1}(2)$	0.099 ± 0.003	0.882 ± 0.038	0.473 ± 0.034
$a_{2,0}(0)$	0.046 ± 0.061	0.379 ± 0.206	0.797 ± 0.190
$a_{2,0}(1)$	-0.097 ± 0.087	-1.669 ± 0.277	-3.258 ± 0.276
$a_{2,0}(2)$	-6.221 ± 0.104	-51.183 ± 0.347	-49.513 ± 0.344
$a_{2,0}(3)$	-0.450 ± 0.121	1.280 ± 0.393	7.192 ± 0.390
$a_{2,1}(1)$	-0.013 ± 0.034	1.235 ± 0.258	4.778 ± 0.281
$a_{2,1}(2)$	5.274 ± 0.023	41.324 ± 0.174	37.289 ± 0.213
$a_{2,1}(3)$	0.282 ± 0.019	-0.508 ± 0.141	-4.510 ± 0.163
$a_{2,1}(4)$	0.035 ± 0.015	0.814 ± 0.115	0.998 ± 0.139
$a_{2,1}(5)$	-0.007 ± 0.014	-0.471 ± 0.100	0.382 ± 0.127
$a_{2,2}(2)$	-2.546 ± 0.026	-21.143 ± 0.079	-19.167 ± 0.082
$a_{2,2}(3)$	-0.099 ± 0.016	0.149 ± 0.048	1.030 ± 0.050
$a_{2,2}(4)$	-0.006 ± 0.011	-0.135 ± 0.034	-0.133 ± 0.035

Table 5.2: Expansion coefficients for $C_{k,q}(\theta, E) = \lambda^2 \sum_L a_{k,q}(L, E) P_L^q(\cos\theta)$. Multiply all values by 10^{-3} for the cross section to be given in mb units.

elements formed with P waves in the entrance channel are negligible at the low energies and become increasing important at higher energies.

In general, the values for the matrix elements agree in magnitude with Garrett and Lindstrom [Gar74], but direct comparison is difficult because the cross sections used in [Gar74] are not known. Their matrix elements were recalculated using their analyzing power measurements along with cross sections calculated from the R-matrix parameterization described in Chapter 6 and were found to agree within the published errors. The largest disagreement between the present

Matrix element	$E = 60$ keV	$E = 99$ keV	
U_2	-0.37 ± 0.49	-5.72 ± 6.03	
U_8	-0.08 ± 0.08	-0.84 ± 0.59	
U_{10}	-0.03 ± 0.11	-0.56 ± 0.84	
U_{11}	-0.26 ± 0.08	-0.27 ± 0.59	
$U_3 + 2U_4$	0.63 ± 0.19	8.80 ± 1.19	
$U_3 - \sqrt{2}U_5$	-0.32 ± 0.11	1.46 ± 0.98	
	$E = 199$ keV	$E = 424$ keV	$E = 641$ keV
U_2	1.33 ± 1.27	-15.71 ± 10.10	-45.75 ± 9.98
U_8	0.27 ± 0.17	-2.07 ± 0.66	-2.31 ± 0.68
U_{10}	-0.51 ± 0.23	1.78 ± 0.94	1.86 ± 0.96
U_{11}	0.46 ± 0.17	-0.46 ± 0.66	1.08 ± 0.68
$U_3 + 2U_4$	1.59 ± 0.19	-5.82 ± 1.50	-28.14 ± 1.70
$U_3 - \sqrt{2}U_5$	0.73 ± 0.37	13.66 ± 1.28	27.26 ± 1.30

Table 5.3: Explicit values of matrix elements. Multiply the $E = 60$ and 99 keV values by 10^{-5} and the $E = 199$, 424, and 641 keV values by 10^{-3}.

calculations and those of [Gar74] is with the matrix element combination U_{11}. Garrett and Lindstrom report that this combination is significant near the resonance, reaching a value of $6.22 \pm 1.3 \times 10^{-3}$ at $E = 465$ keV and falling off above and below, while the present determination shows this value to be close to zero. A possible explanation for this discrepancy can be due to differences in the A_{zz} data, as seen in Figure 1.4. Note that element U_2, which becomes positive only at $E = 199$ keV, agrees with the results of [Gar74] where they find $U_2 = 4.5 \pm 2.7 \times 10^{-3}$ at $E = 344$ keV.

Chapter 6

R-matrix Calculations

A multichannel R-matrix calculation was used to describe the data presented in Chapter 5. This is a global parameterization because all available two-body channels that lead to the formation of the compound nucleus are used. The data set that is included in the parameterization contains cross sections and polarization observables, such as analyzing powers, polarization transfer coefficients, and spin correlation coefficients. Once all the data are parameterized, the R-matrix results can be used to predict a wide range of quantities at any energy. The R-matrix parameterization also gives information about the level scheme of the composite nucleus.

6.1 Theoretical description

The R-matrix formulation is very rigorous and is capable of parameterizing all types of reaction mechanisms. The theory is formulated through a complete set of states in the compound nucleus. Figure 6.1 shows some of the important features of the R-matrix formulation. The separation between the incoming particles is represented by the coordinate r_c. A boundary exists, for each reaction channel, at the channel radius $r = a_c$ where for $r_c > a_c$ the particles are assumed to be in pairs of clusters. The wave function in this area can be described by a combination of incoming and outgoing waves related by the collision matrix. For

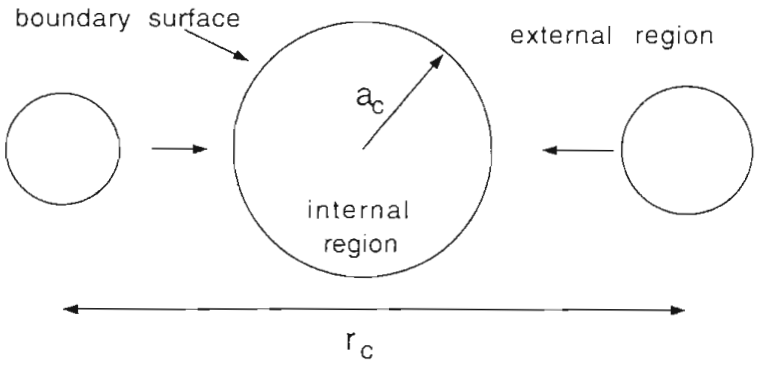

Figure 6.1: R-matrix description of the channels.

$r_c < a_c$ the nuclear force is present and the particles may redistribute themselves into new clusters. The wave function in the interior region is represented by a linear combination of eigenstates which can be related to the levels in the compound nucleus. The wave functions in the interior and exterior regions are related at the channel radius by the R-matrix. In the end, the collision matrix can be related through the R-matrix to the energies and reduced widths that describe the levels in the compound nucleus. To better understand the formalism, the simple case of elastic scattering is first considered and then the more complicated case of the many channel problem is discussed.

6.1.1 One-channel formulation

To get a better understanding of the basic principles of the R-matrix formalism, the simple case of elastic scattering of a spinless particle by a spherical potential is considered. This is also discussed in more detail in Lane and Thomas [Lan58]. In this case the R-matrix will simplify into a R-function.

Derivation of the R-function

Consider the radial part of the Schrödinger equation for two energies, E_1 and E_2:

$$\left(\frac{-\hbar^2}{2m}\frac{d^2}{dr^2}+V\right)\Psi_1 = E_1\Psi_1 \tag{6.1}$$

$$\left(\frac{-\hbar^2}{2m}\frac{d^2}{dr^2}+V\right)\Psi_2 = E_2\Psi_2. \tag{6.2}$$

Multiply equation 6.1 by Ψ_2 and subtract from it equation 6.2 multiplied by Ψ_1 and then integrating this quantity from $r = 0$ to $r = a$, the channel radius, to obtain

$$\left[\Psi_2\frac{d\Psi_1}{dr}-\Psi_1\frac{d\Psi_2}{dr}\right]_{r=a}+\frac{2m}{\hbar^2}(E_1-E_2)\int_0^a\Psi_1\Psi_2 dr = 0. \tag{6.3}$$

Note that this expression is independent of the potential. Assume that at certain values $E = E_\lambda$ the wave function has a slope B at $r = a$ which is independent of E.

$$\left[r\frac{d\Psi_\lambda}{dr}\right]_{r=a} = B[\Psi_\lambda]_{r=a} \tag{6.4}$$

where B is a real number. Substituting two different values of energy, E_1=E_λ and E_2=$E_{\lambda'}$, which satisfy the boundary conditions, equation 6.4, into equation 6.3 yields

$$\int_0^a\Psi_\lambda(r)\Psi_{\lambda'}(r)dr = 0 \qquad \text{for} \quad \lambda\neq\lambda'. \tag{6.5}$$

From this equation the eigenfunctions, $\Psi_\lambda(r)$, with corresponding eigenenergies, E_λ are orthogonal in the interval $0 \leq r \leq a$. As a result of this, the wave function, Ψ_E(r), can be expanded at any energy inside the channel radius in terms of the Ψ_λ(r) as

$$\Psi_E(r) = \sum_\lambda A_\lambda(E)\Psi_\lambda(r) \qquad \text{for} \quad 0 \leq r \leq a. \tag{6.6}$$

The expansion coefficients, A_λ, can be solved for by substituting equation 6.4 into equation 6.3 along with the expansion of $\Psi_E(r)$ to get

$$A_\lambda(E) = \frac{\hbar^2}{2m}\frac{\Psi_\lambda(a)}{E_\lambda-E}\left[\frac{d\Psi_E}{dr}-\frac{B}{r}\Psi_E\right]_{r=a} \tag{6.7}$$

Putting the solution of the expansion coefficients back into the expansion of $\Psi_E(r)$ yields

$$\Psi_E(r) = G(r,a)a\left[\frac{d\Psi_E}{dr} - \frac{B}{r}\Psi_e\right]_{r=a} \tag{6.8}$$

where

$$G(r,a) = \frac{\hbar^2}{2ma}\sum_\lambda \frac{\Psi_\lambda(r)\Psi_\lambda(a)}{E_\lambda - E} \tag{6.9}$$

is a Green's function for the Schrödinger equation. Note that equation 6.8 relates the wave function in the internal region to the wave function and its derivative at $r = a$. The R-function is defined by

$$R \equiv G(a,a) = \sum_\lambda \frac{\gamma_\lambda^2}{E_\lambda - E} \tag{6.10}$$

and the γ_λ^2 is the reduced-width amplitude defined as

$$\gamma_\lambda = \sqrt{\frac{\hbar^2}{2ma}}\Psi_\lambda(a). \tag{6.11}$$

The R-function can be related to the logarithmic derivative of the wave function at $r = a$ by

$$\left[\frac{r}{\Psi_E}\frac{d\Psi_E}{dr}\right]_{r=a} = R^{-1}(1 + RB) \tag{6.12}$$

The R-function can now be related to the logarithmic derivative of the external wave function at $r = a$ through a quantity called the collision function.

Relation of the R-function to the collision function

The wave function may be expressed in the external region as a combination of incoming and outgoing waves as

$$\Psi_l \approx I_l - U_l O_l \tag{6.13}$$

where I_l is the incoming wave, O_l is the outgoing wave, and U_l is the collision function. The collision function is the amplitude of unit-flux outgoing wave associated with unit-flux incoming wave. The collision function may be related

to the R-function by equating the logarithmic derivatives of the external and internal wave functions at $r = a$,

$$U_l = \frac{I_l}{O_l}\left(\frac{1 - L_l^* R_l}{1 - L_l R_l}\right) \tag{6.14}$$

where L_l is the logarithmic derivative of the outgoing wave. From the collision function many observables, such as the cross section and analyzing powers, can be determined.

6.1.2 Many-channel formulation

The situation becomes much more complicated when the interaction involves particles with spin which can undergo reactions with $L \geq 0$. The description of the reaction is similar to the single channel case except that now the R-function and collision function will become matrices. Again a region is defined at $r = a$ where in the external area the nuclear force does not act and the R-matrix is used to relate the internal region to the external region. The R-matrix parameterization done at LANL utilizes a Bloch operator in the formalism [Hal80]. For completeness, a brief description of the LANL R-matrix theory as described in [Hal80] is given below.

One starts off with the Schrödinger equation inside the channel surface,

$$(H - E)\Psi = 0. \tag{6.15}$$

The Bloch operator, $\mathcal{L}$, can be added to both sides

$$(H + \mathcal{L} - E)\Psi = \mathcal{L}\Psi. \tag{6.16}$$

The operator $\mathcal{L}$ is chosen so that it projects onto the channel surface and as a result Ψ everywhere in the interior region can be determined if its projection on the channel surface is known. Also, with the correct choice of $\mathcal{L}$ the quantity $(H + \mathcal{L} - E)^{-1}$ will be hermitian. The choice of $\mathcal{L}$ is [Hal80]

$$\mathcal{L} = \sum_c |c><c|(\frac{\partial}{\partial r_c} r_c - B_c) \tag{6.17}$$

where

$$|c>=\left(\frac{\hbar^2}{2m_c a_c}\right)^{\frac{1}{2}}\frac{\delta(r_c-a_c)}{a_c}Y_c(\hat{r}_c) \tag{6.18}$$

is the channel-surface function. One can see that the delta function ensures that the projection operator, $\mathcal{L}$, projects the wave function onto the channel surface, $r_c = a_c$, and this wave function will be defined in terms of the channel eigenfunctions $Y_c(\hat{r}_c)$. One can now take the projection of equation 6.16 to obtain

$$< c'|\Psi >= \sum_c < c'|G|c >< c|\frac{\partial}{\partial r_c}r_c - B_c|\Psi > \tag{6.19}$$

where G is the Green's function operator:

$$G = (H + \mathcal{L} - E)^{-1}. \tag{6.20}$$

Since $H + \mathcal{L}$ is hermitian, the eigenfunctions $|\lambda >$ which satisfy

$$(H + \mathcal{L})|\lambda >= E_\lambda|\lambda > \tag{6.21}$$

for the eigenvalues E_λ will form a complete orthogonal set in the internal region. The Green's function operator can be expanded as

$$G = \sum_\lambda \frac{|\lambda >< \lambda|}{E_\lambda - E} \tag{6.22}$$

and from this results the definition of the elements of the R-matrix,

$$R_{c'c} =< c'|G|c >= \sum_\lambda \frac{\gamma_{\lambda c'}\gamma_{\lambda c}}{E_\lambda - E} \tag{6.23}$$

where the $\gamma_{\lambda c}$ are the reduced width amplitudes for level λ and channel c.

As in the single channel case, in the exterior region the wave function at the boundary can be written as a combination of incoming and outgoing waves

$$< c'|\Psi >= I_{c'}(a_c)\delta_{c'c} - O_c(a_c)U_{c'c}. \tag{6.24}$$

The boundary condition was chosen to be the logarithmic derivative of the outgoing wave and is

$$L_c = \left(\frac{r_c \partial O_c}{\partial r_c}/O_c\right)_{r_c=r_a}. \tag{6.25}$$

This choice of the boundary condition differs from the Wigner R-matrix (see equation 6.4) choice, because the boundary is complex and depends on the energy and channel radius. This choice (called the outgoing-wave R-matrix, R_L) has more physical significance and simplifies the relation between the R-matrix and U-matrix. To relate the internal and external regions, equation 6.19 is evaluated at the channel surface with the known external wave functions. In matrix notation this is

$$\Psi = \mathbf{R_L}(\Psi' - \mathbf{L}\Psi) \tag{6.26}$$

Substituting the expression for the external wave function into this equation will result in an expression for the collision matrix

$$\mathbf{U} = \mathbf{O}^{-1}\mathbf{R_L}\mathbf{O}^{-1} - \mathbf{O}^{-1}\mathbf{I}. \tag{6.27}$$

From this relationship between the R-matrix and the U-matrix all types of observables can be calculated.

6.2 The LANL R-matrix analysis

In October of 1997, Dr. Hale and the author performed an R-matrix analysis for the ^{5}Li system. The analysis was done with the LANL code EDA (Energy-Dependent Analysis). The EDA code adjusted the R-matrix parameters (the reduced-width amplitudes $\gamma_{\lambda c}$ and the energies E_λ) to obtain the best fit to the data by minimizing the χ^2. An input file contains all of the published data for the ^{5}Li system, which includes the ^{4}He$(p,p)^4$He, ^{3}He$(d,d)^3$He, and ^{3}He$(d,p)^4$He reactions. The data contain cross sections, analyzing powers, and spin correlation coefficients.

The first task was to add the current data to the existing input file[9], which contained data up to about 28 MeV excitation in ^{5}Li. The EDA code was then

[9]The existing input file was used to calculate the R-matrix predictions shown in Figures 6.2 to 6.7, and was also used in the $A = 5$ level compilation [Til98]. The measurements that are contained in this data set are given in [Til98].

Reaction	Energy range (MeV)	No. observables	No. data points
^{3}He$(d,d)^3$He	$E_d = 0 - 1$	1	128
^{3}He$(d,p)^4$He	$E_d = 0 - 1$	10	1241
^{4}He$(p,p)^4$He	$E_p = 0 - 24$	3	562
Total		14	1931

Table 6.1: The data set for the R-matrix calculations.

run. It was realized quickly that the EDA code was having problems fitting the existing data. A decision was made to truncate the data set to include only data corresponding to energies up to $E_d = 1$ MeV in the ^{3}He$(d,p)^4$He reaction. This resulted in the removal of a large quantity of data and also several of the R-matrix parameters. The final data set used is given in Table 6.1. This includes the $d-^3$He differential cross section elastic scattering data of Kraus [Kra71] and Brown *et al.* [Bro54]. The $d - ^3$He reaction data contains the integrated cross sections of Krauss *et al.* [Kra87] and Möller and Besenbacher [Möl80]; differential cross sections of Krauss *et al.* [Kra87], Kunz [Kun55], Yarnell *et al.* [Yar53], and Bittcher *et al.* [Bit90]; analyzing power data of Rohrer *et al.* [Roh71], Garrett and Lindstrom [Gar74], Leemann *et al.* [Lee71], Ohlsen [Ohl98], Forssman [For98], and Bittcher *et al.* [Bit90]; and spin-correlation coefficients of Leemann *et al.* [Lee71]. The $p - \alpha$ data include differential cross sections by Barnard *et al.* [Bar64], Garreta *et al.* [Gar69], and Plattner *et al.* [Pla72]; and analyzing power data of Brown and Trächslin [Bro67], Garreta *et al.* [Gar69], and Plattner *et al.* [Pla72]. The present measurements included in the analysis consist of 349 data points and account for more than 25% of the data for the ^{3}He$(d,p)^4$He reaction.

The R-matrix calculations are shown with the data in Figures 6.2 to 6.7. The highest partial waves allowed in the entrance channel is $L = 2$, while for the exit channel up to $L = 4$ was allowed. The R-matrix parameterization reached a χ^2 of 1.8. A χ^2 of between 1 and 2 is considered a good parameterization of the data set [Hal98]. In the R-matrix calculation the data were allowed to be scaled

within their systematic errors. The data shown in the figures were renormalized by the value determined from the R-matrix code. Also included in the figures are the R-matrix predictions which used a data set described in [Til98] (Set A) and was made prior to including the current data. As expected based on the reduced chi squared[10] values (see Table 6.2) the R-matrix parameterization that include both the present data and the data listed previously (Set B) describes the data much better than the Set A calculations. For A_y at 641 keV the prediction is found to be very different from the data, in contrast to the lower energies. This disagreement can be understood by looking at the trend of the A_y data. At the low energies the angular distributions are backward peaked while at the higher energies ($E \approx 1\ MeV$) the distribution becomes forward peaked. This indicates that the parameters of the R-matrix prediction are poorly defined in this energy range because the change from a forward- to backward-peaked distribution occurs at too low an energy. As seen in Figure 6.2, the Set B R-matrix calculations agree very well with A_y. The Set B R-matrix parameterization also agrees much better than the predictions (Set A calculations) for the total cross section, as seen in Figure 6.7. In fact, these data have better defined the $\frac{3}{2}^+$ resonance in ^{5}Li.

The level structure of ^{5}Li can be obtained from the R-matrix analysis. The level scheme is shown in Table 6.3 for the current calculations, along with the level scheme from the $A = 5$ level compilation [Til98]. The levels were obtained from the "extended" R-matrix method [Hal87, Csó97] and uses the complex poles and residues of the S-matrix. This prescription results in resonance parameters that are free from the geometric parameters of the R-matrix theory, such as the channel radii and boundary conditions.

The $\frac{3}{2}^+$ level can be seen to have shifted to a slightly lower energy compared to the value reported in [Til98]. This value is based on an R-matrix parame-

[10]The reduced chi squared values are defined by $\chi^2 = \frac{1}{N}\sum_i (x_i - x_c)^2/\Delta x_i^2$ where x_i is the experimentally measured value with error Δx_i, x_c is the R-matrix calculation, and N is the number of data points.

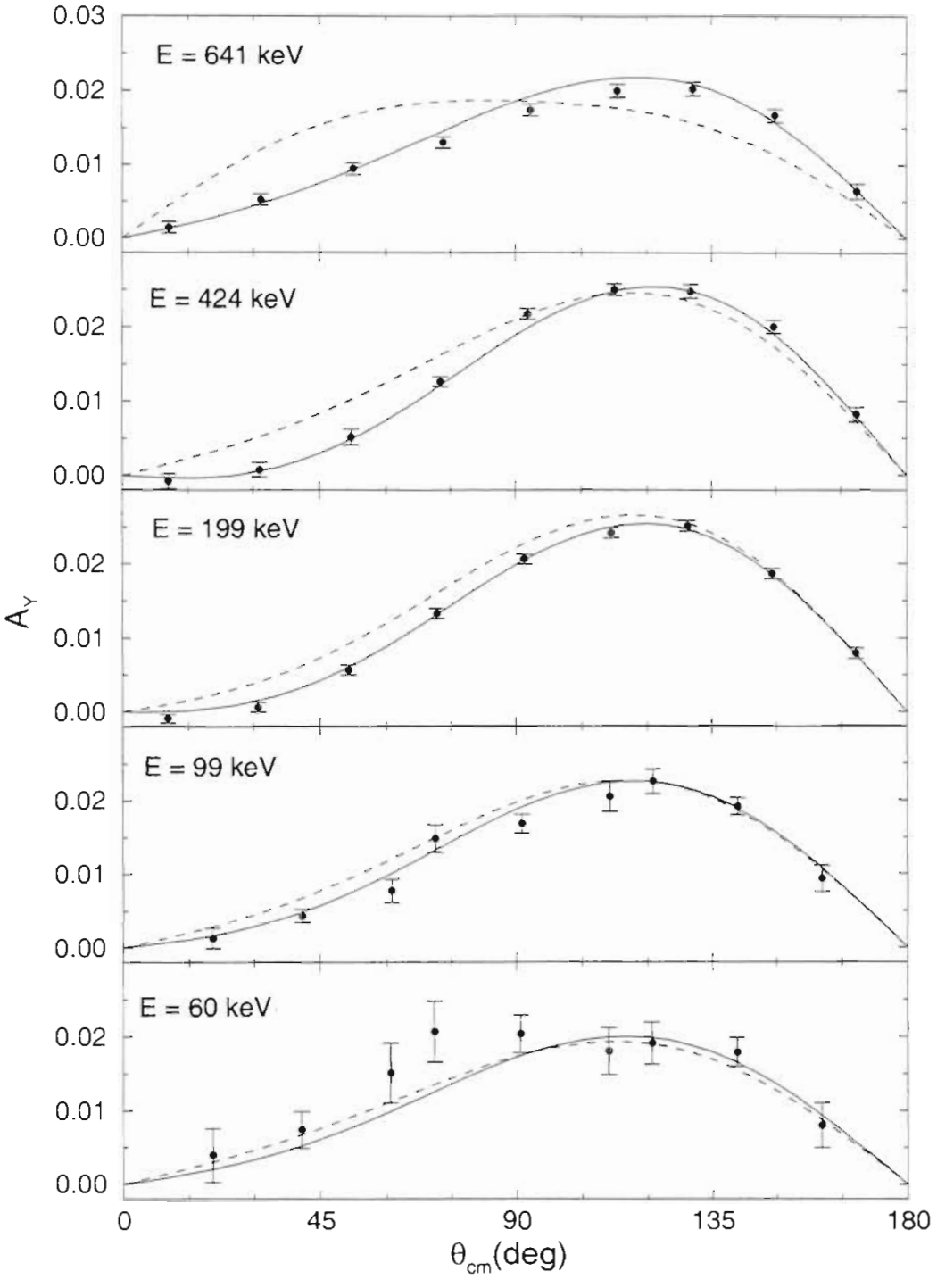

Figure 6.2: Comparison of the A_y data with the R-matrix calculations. The dashed lines are the R-matrix predictions obtained using Set A. The solid lines are the new R-matrix calculation obtained using Set B.

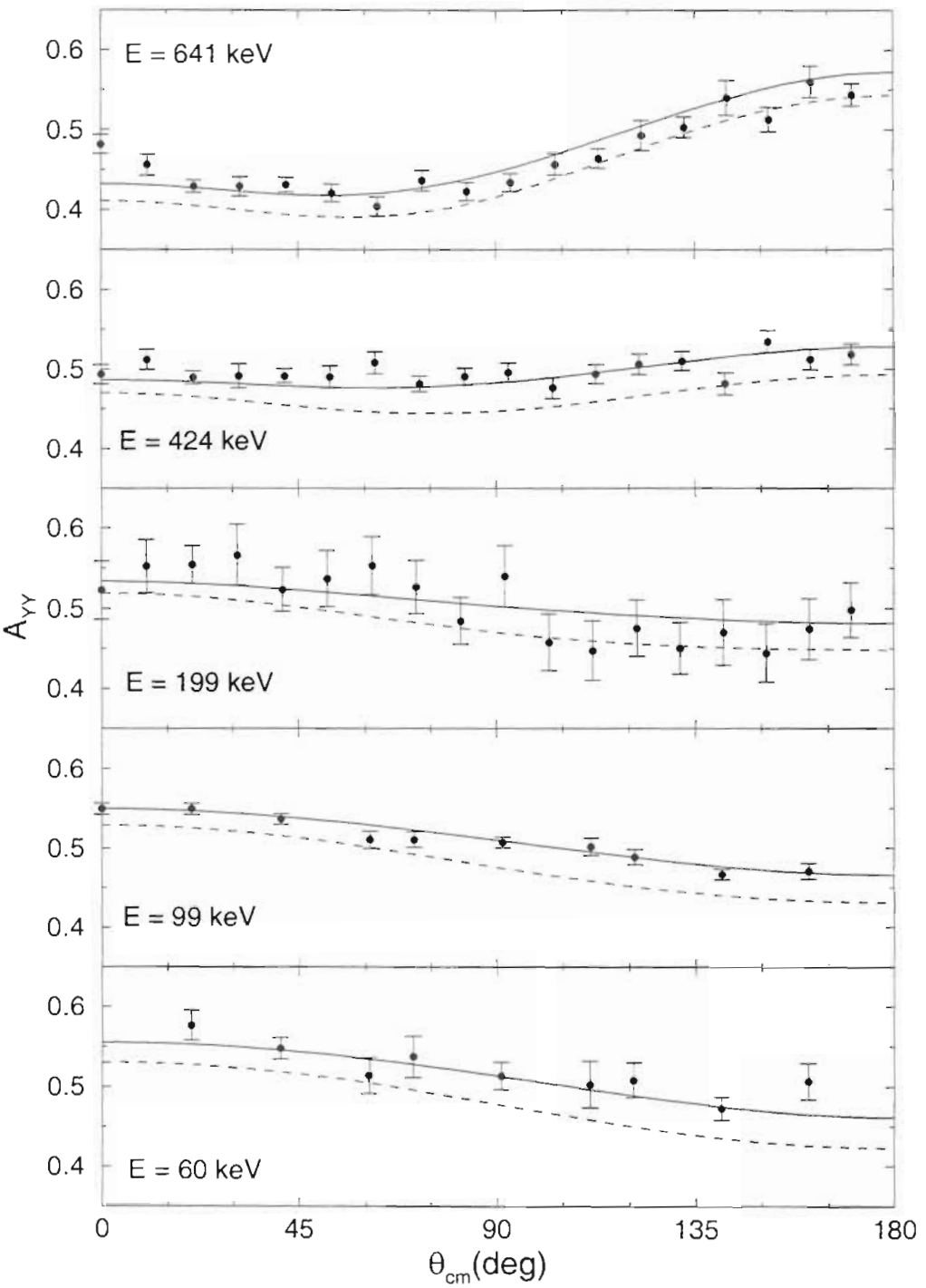

Figure 6.3: Comparison of the A_{yy} data with the R-matrix calculations. The dashed lines are the R-matrix predictions obtained using Set A. The solid lines are the new R-matrix calculation obtained using Set B.

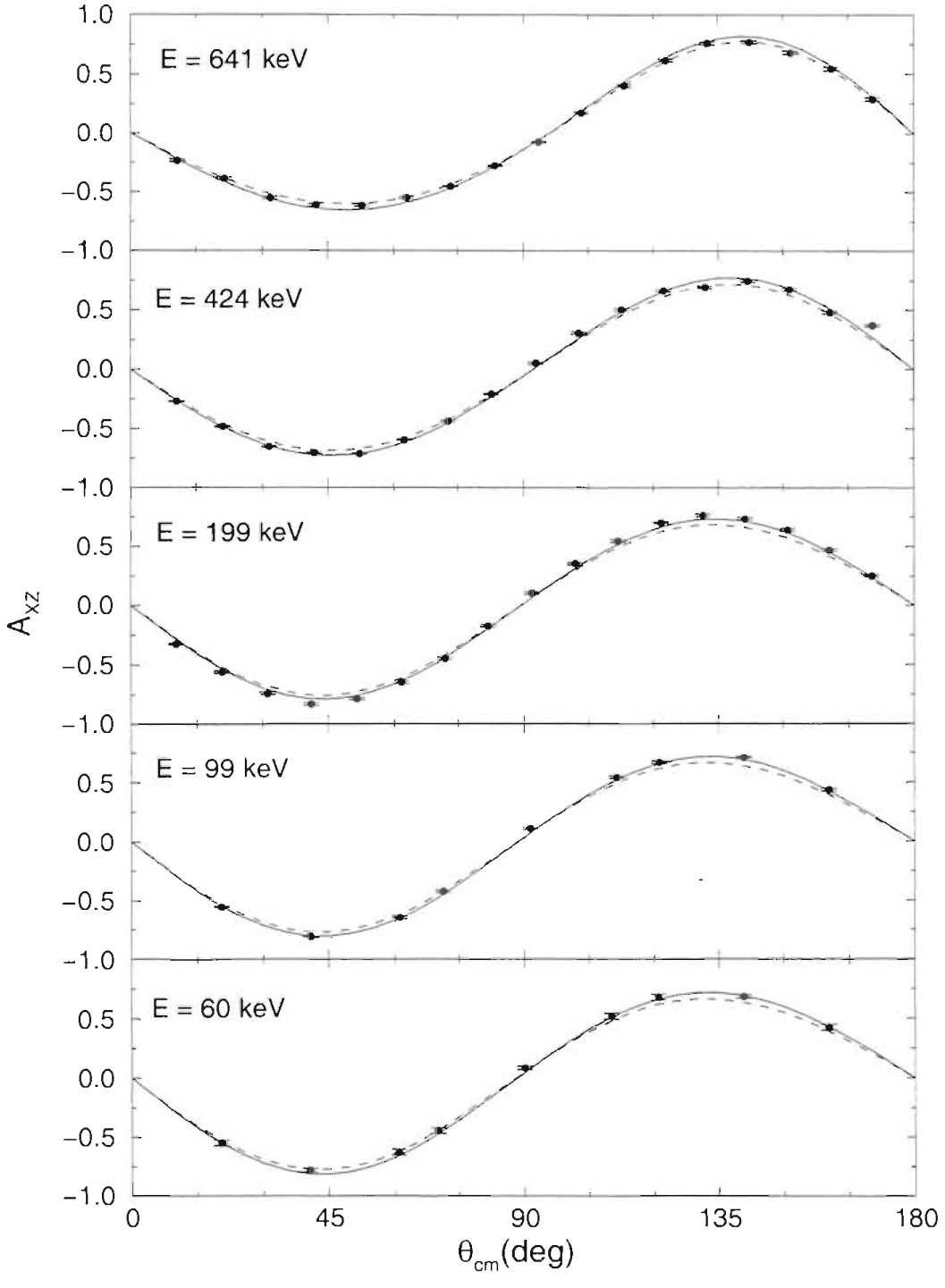

Figure 6.4: Comparison of the A_{xz} data with the R-matrix calculations. The dashed lines are the R-matrix predictions obtained using Set A. The solid lines are the new R-matrix calculation obtained using Set B.

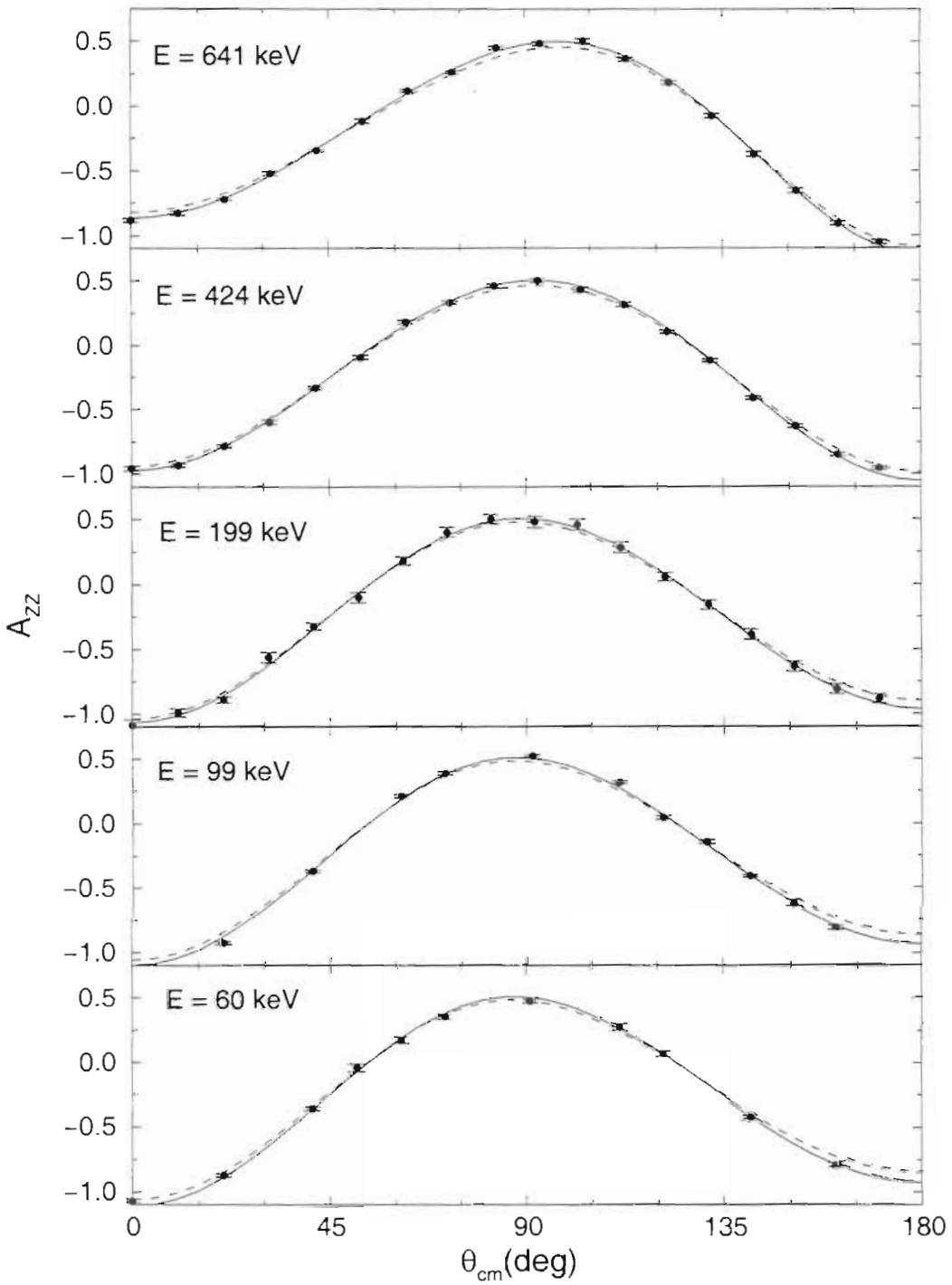

Figure 6.5: Comparison of the A_{zz} data with the R-matrix calculations. The dashed lines are the R-matrix predictions obtained using Set A. The solid lines are the new R-matrix calculation obtained using Set B.

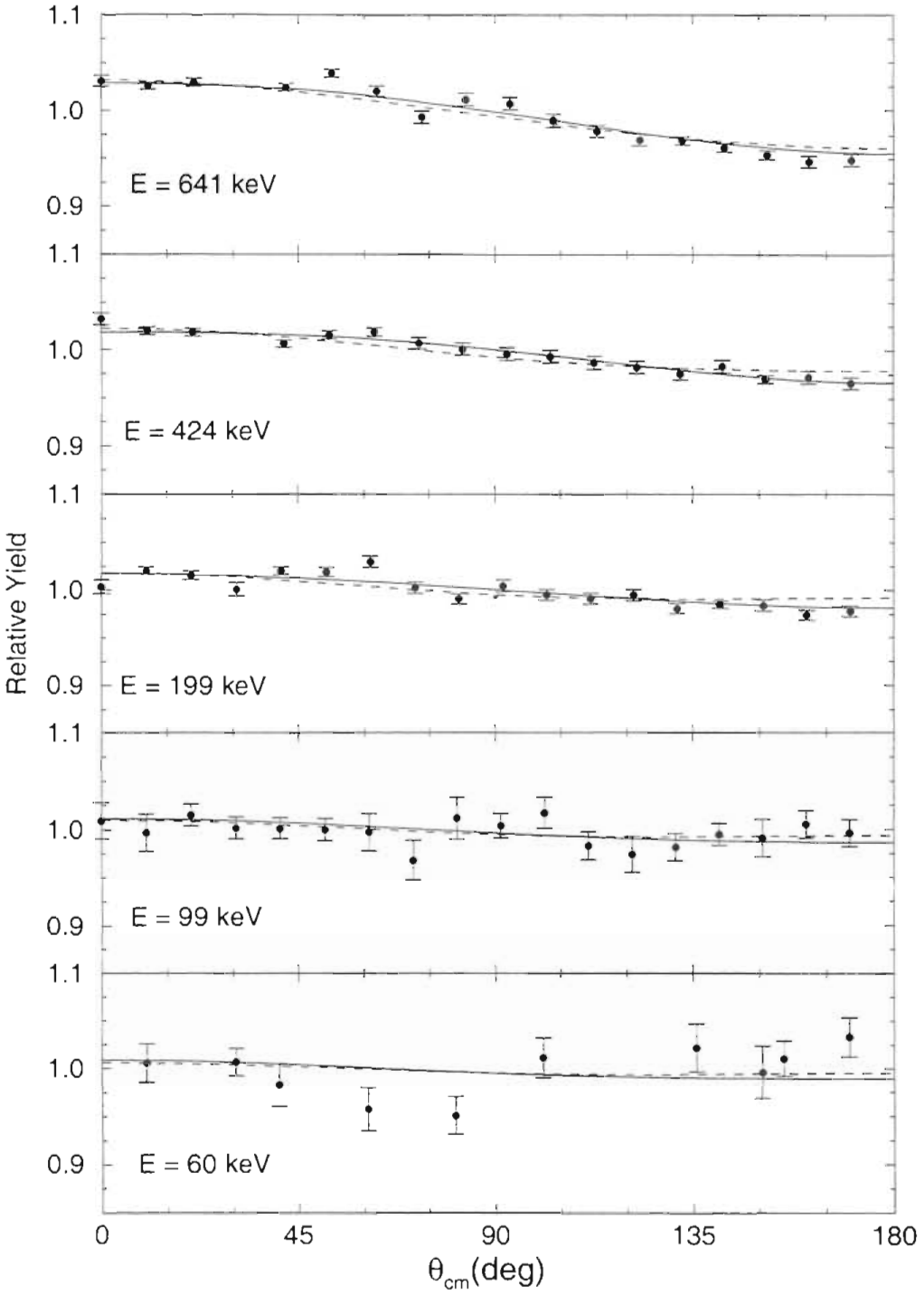

Figure 6.6: Comparison of the $\sigma(\theta)$ data with the R-matrix calculations. The dashed lines are the R-matrix predictions obtained using Set A. The solid lines are the new R-matrix calculation obtained using Set B.

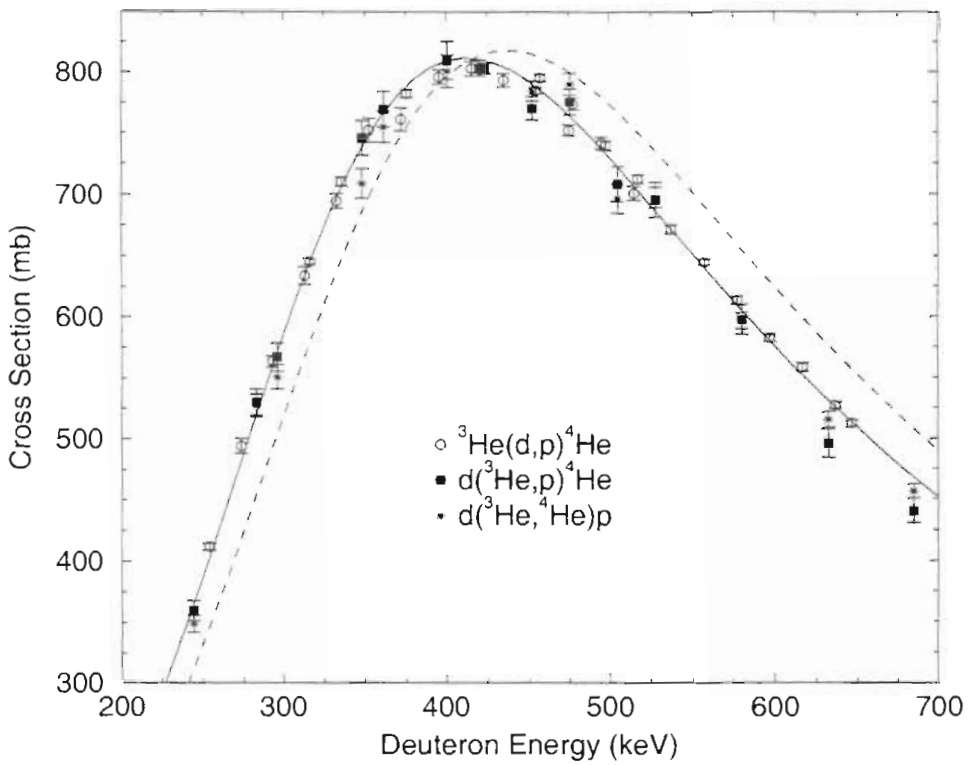

Figure 6.7: Comparison of the $\sigma(E)$ data with the R-matrix calculations. The dashed lines are the R-matrix predictions obtained using Set A. The solid lines are the new R-matrix calculation obtained using Set B.

terization using Set A. As seen in Figure 6.7, the R-matrix prediction has the cross section peaking at about 10 keV higher than the data and in the new R-matrix parameterization this level is shifted down by 10 keV. The first two levels in ^{5}Li are seen to agree well between the two parameterizations. This result is expected because these levels are defined mainly by the $p-\alpha$ channel which includes the same data for both of the R-matrix parameterizations. One major difference between the current and previous level scheme is a $\frac{1}{2}^+$ level located below the ^{3}He$+d$ threshold in the current level scheme. One should note that for a $\frac{1}{2}^+$ S-wave resonance interfering with a $\frac{3}{2}^+$ S-wave resonance, the cross section would be isotropic and the analyzing powers would only differ by a scale factor

E	A_y		A_{yy}		A_{xz}		A_{zz}		σ		total	
(keV)	χ^2_B	χ^2_A	χ^2_B	χ^2_A	χ^2_B	χ^2_A	χ^2_B	χ^2_A	χ^2_B	χ^2_A	χ^2_B	χ^2_A
60	0.9	0.7	0.7	5.0	1.5	2.8	1.6	2.8	1.8	1.6	1.3	2.6
99	0.9	2.4	0.7	11.3	5.9	23.0	3.8	13.5	0.6	0.5	2.1	8.9
199	0.7	10.2	0.6	1.0	8.6	29.6	0.5	1.0	2.1	3.7	2.6	8.7
424	1.0	8.9	1.3	9.0	13.7	23.6	2.3	3.4	1.0	2.0	4.1	9.3
641	1.6	30.5	2.5	5.7	6.8	2.4	1.3	7.2	2.6	4.1	3.1	7.8
total	1.0	10.6	1.3	6.0	8.1	17.1	1.8	5.2	1.6	2.4	2.8	7.8

Table 6.2: Reduced chi squared values for the analyzing power and cross section data. The subscripts A and B refer to the R-matrix calculation with Set A and Set B, respectively.

from that for a pure $\frac{3}{2}^+$ S-wave resonance. Since the previous level scheme was derived from a data set that contained very little analyzing power data below 1 MeV (Set A), it would not be as sensitive to a $\frac{1}{2}^+$ level as the current scheme. The data of Set A did have cross section distributions, but it is likely that this level is the result of the low-energy analyzing power measurements.

In addition to the levels listed in Table 6.3, there is evidence for several other very weak levels. These have $J^\pi = \frac{1}{2}^+$, $\frac{3}{2}^-$, and $\frac{7}{2}^+$. The $\frac{1}{2}^+$ level is located within the energy range of this analysis, while the $\frac{3}{2}^-$ and $\frac{7}{2}^+$ levels are located at higher energies. All three of these weak resonances most likely correspond to previously observed resonances [Til98] located in ^{5}Li at higher energies than determined from this analysis. These levels are very poorly defined in this analysis because the data set is truncated at an energy below the "real" location of these levels. In previous work (see Section 1.2), there has been considerable discussion about a possible $\frac{1}{2}^+$ resonant state in ^{5}Li at $E_d \approx 1-3$ MeV. From the current analysis evidence of a weak $\frac{1}{2}^+$ level is seen, but is not well defined due to the energy range that was parameterized. One should note however, that the most recent level assignment of ^{5}Li does include a $\frac{1}{2}^+$ state in this energy range.

Previous scheme			Current scheme		
E_x (MeV)	J^π	Γ_{cm} (MeV)	E_x (MeV)	J^π	Γ_{cm} (MeV)
g.s	$\frac{3}{2}^-$	1.23	g.s	$\frac{3}{2}^-$	1.25
1.49	$\frac{1}{2}^-$	6.60	1.44	$\frac{1}{2}^-$	6.08
			15.86	$\frac{1}{2}^+$	0.58
16.87	$\frac{3}{2}^+$	0.27	16.86	$\frac{3}{2}^+$	0.25
19.28	$\frac{3}{2}^-$	0.96			
19.45	$\frac{7}{2}^+$	3.82			

Table 6.3: The level scheme of ^{5}Li. The previous scheme is obtained from an R-matrix analysis using Set A [Til98] and the current scheme is from the new R-matrix analysis with Set B.

The R-matrix analysis can reveal information about the matrix elements that contribute to the $^3\mathrm{He}(d,p)^4\mathrm{He}$ reaction. For the channels that proceed through a resonant process, the levels in ^{5}Li give an indication which matrix elements will be important. One would expect that the channels that have the same total angular momentum and parity as resonances in ^{5}Li and are located within the energy range of interest would contribute to the reaction more than others. While this assumption includes only channels that proceed through a resonance process, the R-matrix analysis is also able to reveal information about direct processes. This is done by mimicking a direct process with a very broad resonance, which is often located at a high energy.

To get an idea of the size of contributions from individual channels, the contribution to the cross section for each channel is shown in Figures 6.8 to 6.10. As expected, the $^4S_{\frac{3}{2}}$ entrance channel which corresponds to the $\frac{3}{2}^+$ resonance is the most dominating contribution to the cross section, as seen in Figure 6.8. The contribution of this channel to the cross section is at least an order of magnitude greater than any of the other channels and it is also responsible for the dominating features of the analyzing powers. The other S-wave channel, the $^2S_{\frac{1}{2}}$ channel, can

be seen to have a dip near $E_d = 380$ keV. This is most likely due the $\frac{1}{2}^+$ level in ^{5}Li destructively interfering with underlying background contributions [Hal98]. Since this effect is so small, it would not show up in the integrated cross section, which means that it must be coming from the polarization data. The polarization observables may indicate a possible phase crossing around the energy of this dip. For example, the A_{yy} data change from being backward peaked above this energy to forward peaked below this energy. The A_{zz} data also display a forward tilt above this energy and a backward tilt below this energy. This is suggestive that some interference term crosses through zero around this energy. One should also note that it is possible that there may exist another R-matrix solution that produces just as good a fit, but does not have this destructive interference [Hal98]. For example, the previous R-matrix solution did not have any evidence for this effect, but it also did not contain the low-energy analyzing power data.

For the P waves involved, the $^2P_{\frac{3}{2}}$ channel is the most important, as seen in Figure 6.9. Also from the figure one can see that all the P waves are increasing in importance at the higher energies. The $^4D_{\frac{3}{2}}$ wave appears to be the most important D wave in the vicinity of the resonance, while the $^4D_{\frac{5}{2}}$ channel becomes increasingly important at higher energies as seen in Figure 6.10. As seen in Figure 6.11, the shape of the $^4D_{\frac{3}{2}}$ channel is different from the other D-wave channels. The fact that the cross section rapidly increases up to the energy of the $\frac{3}{2}^+$ resonance is indicative that this channel also proceeds at least partly through this resonance in ^{5}Li.

The new R-matrix analysis was very successful in reproducing the low-energy measurements. From this analysis, any observable within the energy range of this analysis can be predicted to a greater accuracy than from the previous R-matrix solution. The analysis also demonstrated that P and D waves are important at low energies. Among the P waves the $^2P_{\frac{3}{2}}$ entrance channel in found to be most important and even more important than D waves in the entrance channel. The $^4D_{\frac{3}{2}}$ entrance channel is found to proceed through the resonance and is most

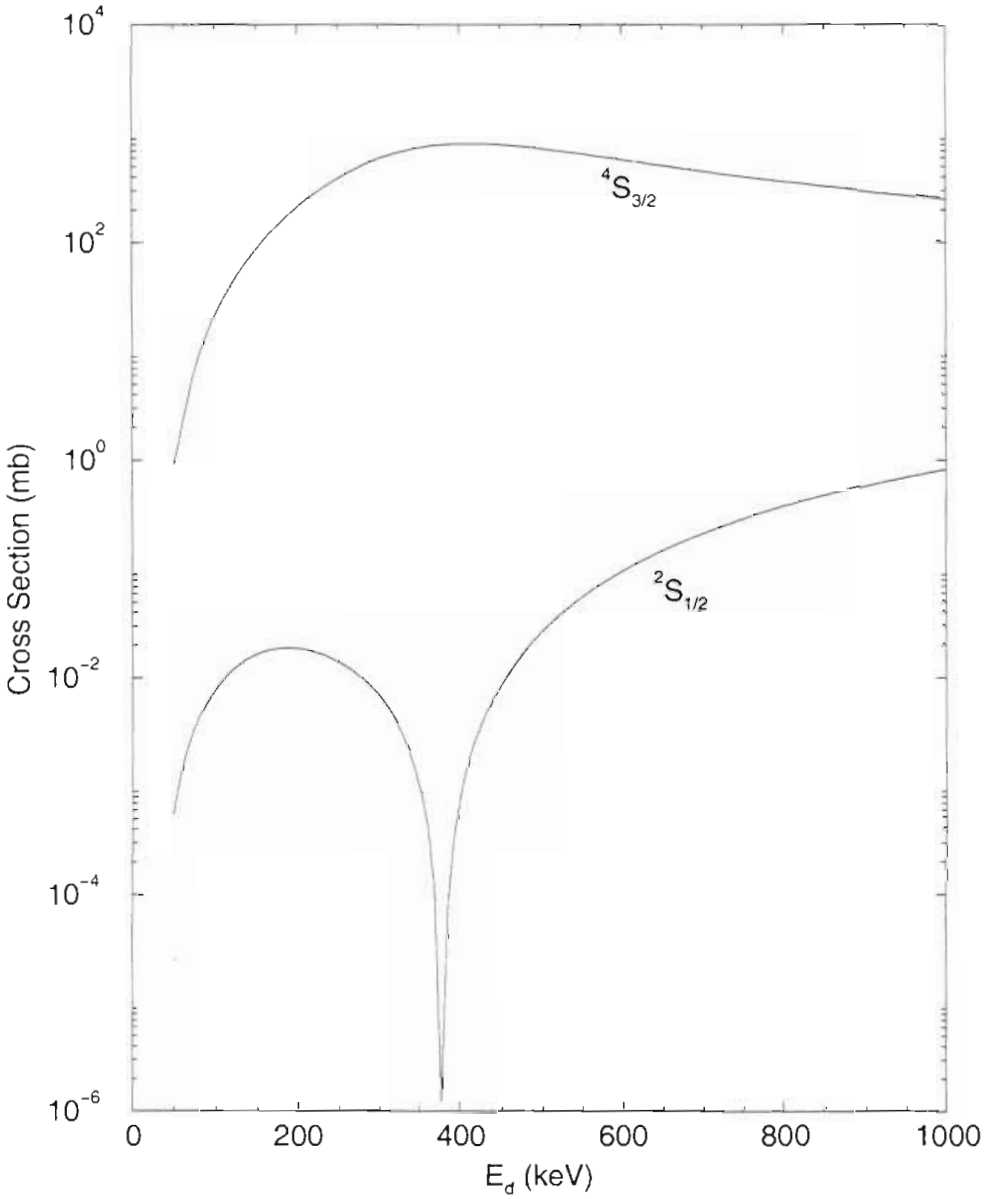

Figure 6.8: The contribution to the cross section for different S-wave channels. The entrance channel is listed next to the curve in the graph.

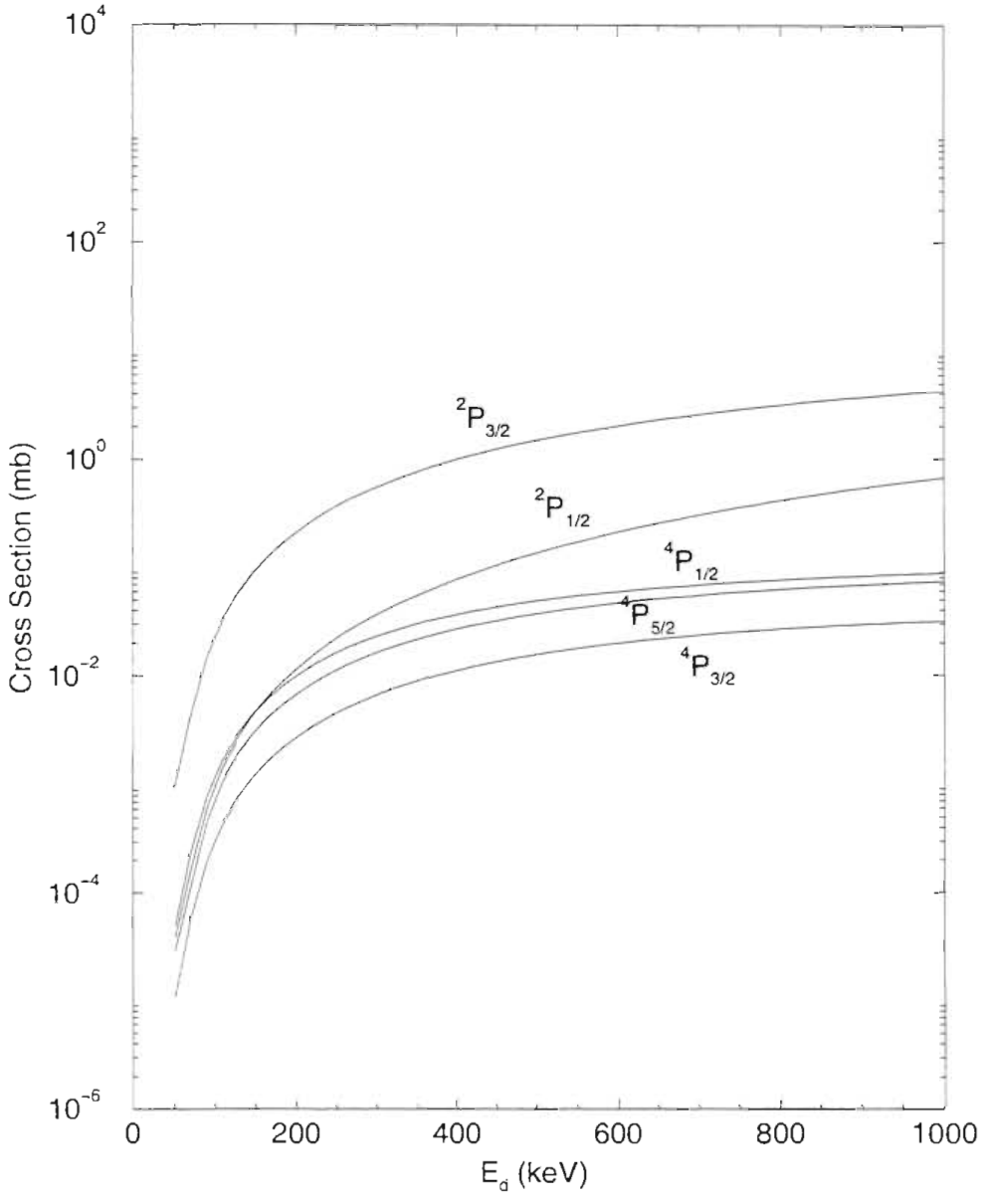

Figure 6.9: The contribution to the cross section for different P-wave channels. The entrance channel is listed next to the curve in the graph.

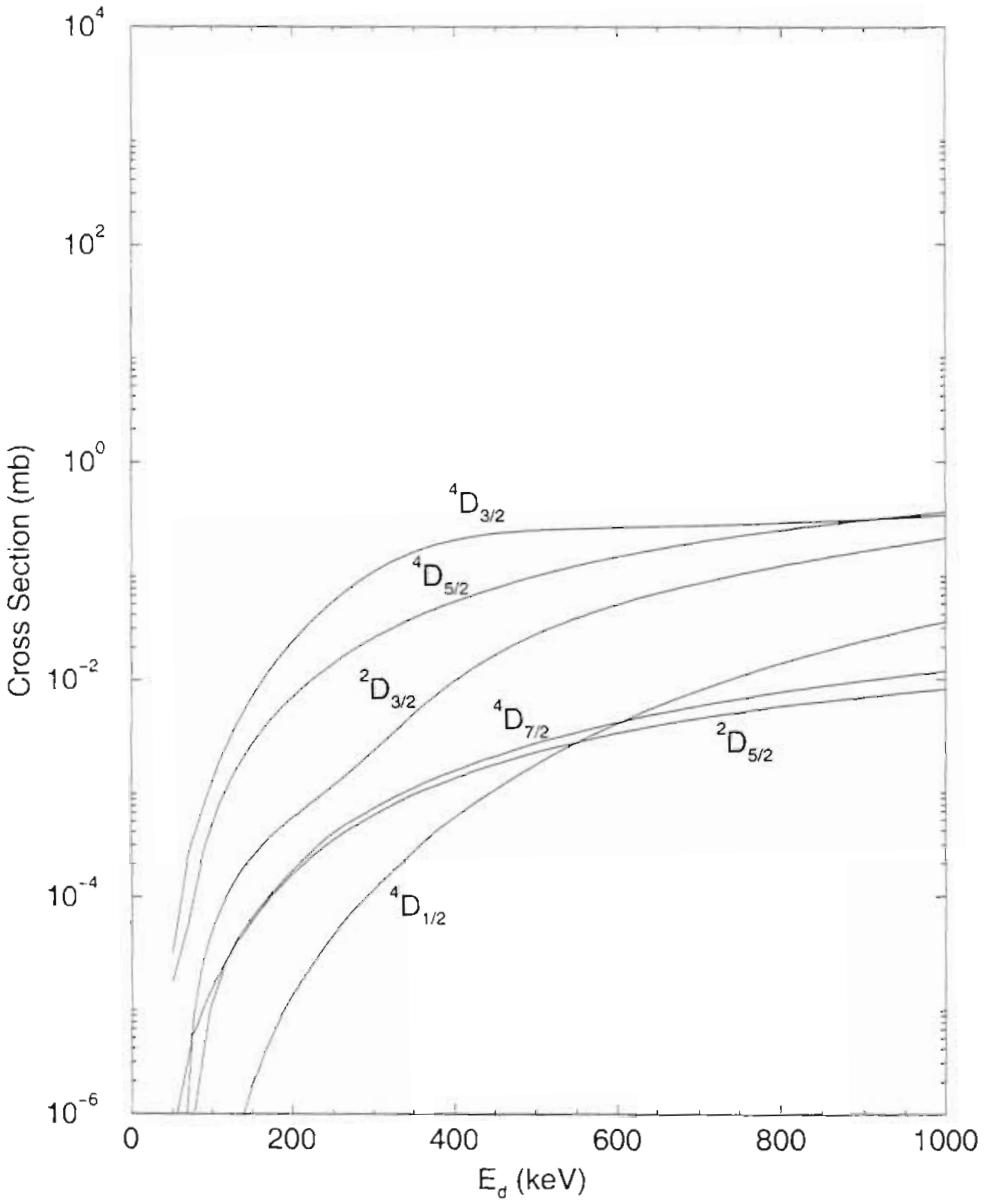

Figure 6.10: The contribution to the cross section for different D-wave channels. The entrance channel is listed next to the curve in the graph.

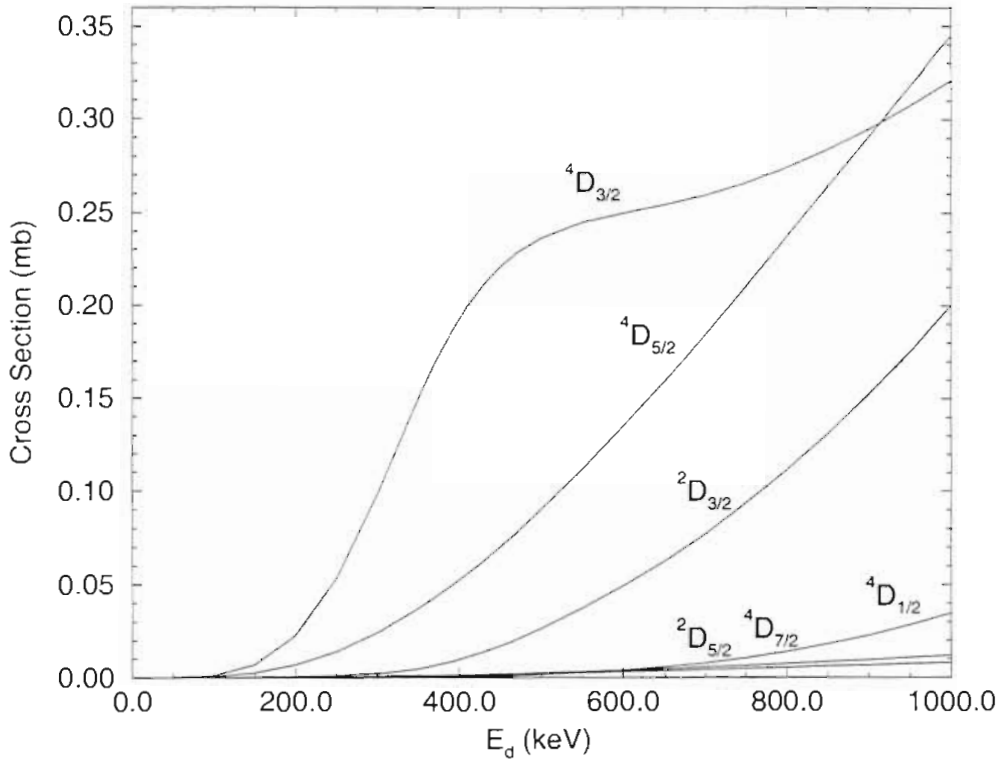

Figure 6.11: The contribution to the cross section for different D-wave channels, shown on a linear scale. The entrance channel is listed next to the curve in the graph. Notice that the ${}^4D_{\frac{3}{2}}$ channel exhibits an energy dependence that is suggestive that it proceeds through the $\frac{3}{2}^-$ resonance in ^{5}Li.

important around the resonance, while the ${}^4D_{\frac{5}{2}}$ entrance channel becomes more important at higher energies.

6.3 Electron screening using R-matrix results

To calculate a screening potential, the bare nuclear cross section needs to be known to zero energy and it is often determined from an extrapolation of the higher energy data to the energy range of interest. To do this, the cross section is often transformed to an astrophysical S-factor which is usually nearly

constant and smoothly varying at low energies in contrast to the cross section which drops exponentially with decreasing energy due to the Coulomb barrier. The $S(E)$ factor is defined by

$$\sigma(E) = \frac{S(E)}{E} \exp(-2\pi\eta(E)) \tag{6.28}$$

where the Sommerfeld parameter, $2\pi\eta(E) \approx 31.29 Z_1 Z_2 \sqrt{\mu/E}$, Z_1 and Z_2 are the charges of the interacting particles in the entrance channel, μ is the reduced mass in units of amu, and E is the center-of-mass energy in keV. Recall from Section 1.1.2 that the enhancement factor due to the electrons in the target is defined as

$$f(E) = \frac{\sigma_{exp}(E)}{\sigma_{bn}(E)} = \frac{\sigma(E + U_e)}{\sigma(E)} \tag{6.29}$$

where U_e is the screening potential. For the case of $U_e \ll E$ and approximating $S(E)/E = S(E + U_e)/(E + U_e)$ one finds that

$$f(E) \approx \exp(\pi\eta(E)\frac{U_e}{E}). \tag{6.30}$$

From the new R-matrix parameterization the cross section can be calculated down to this energy range and a screening factor can be calculated. The astrophysical S-factor obtained from the R-matrix parameterization is shown in Figure 6.12 along with several previously determined extrapolations. All of the previous extrapolations were done by fitting the higher-energy cross section data and then extending the fit to lower energies. The extrapolation by Chulick *et al.* [Chu93] which is used in the most recent screening calculations [Lan96] was done by fitting all of the existing data which includes data sets that in some cases are in very large disagreement with each other. The present S-factor determination, that is used to determine an electron-screening potential, is the first calculation of the S-factor that did not originate from an extrapolation of data.

There have been several theoretical calculations of the screening potential for the ^{3}He$(d,p)^4$He reaction [Bra90, Sho93, Lan92]. A simple model to calculate this potential assumes that the classical turning radius of a projectile for a bare

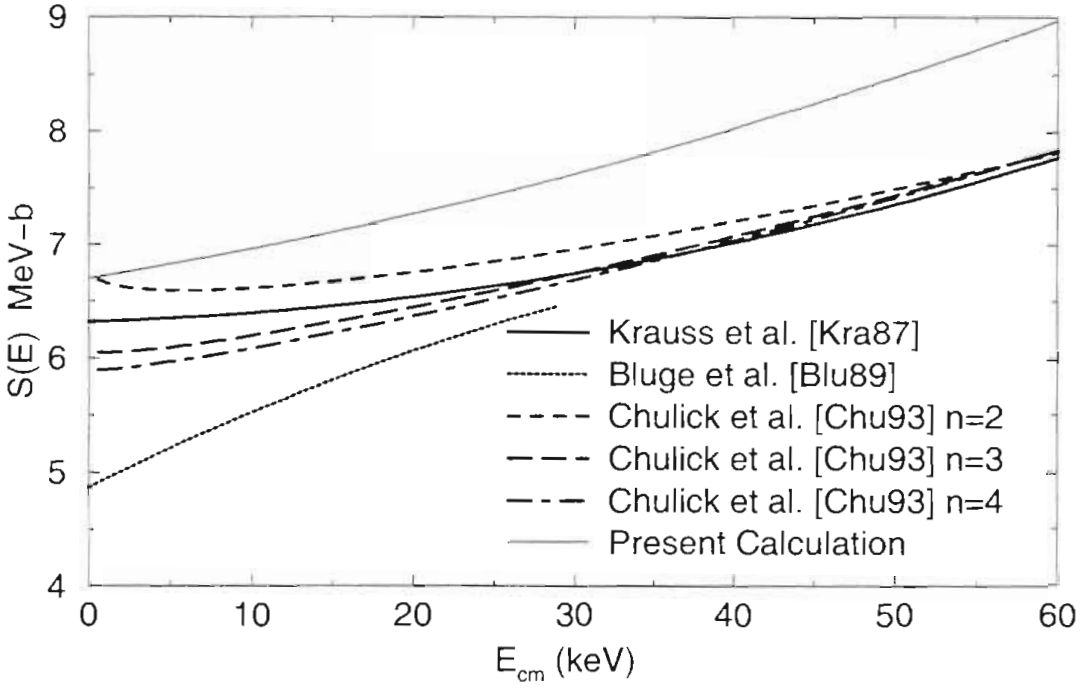

Figure 6.12: Comparison of the astrophysical S-factors for the ^{3}He$(d,p)^4$He reaction. In the extrapolations of Chulick *et al.* [Chu93] the parameter n corresponds to the highest-order polynomial used in the fit to the data.

nucleus is larger than the atomic radius, then $U_e \approx Z_1 Z_2 e^2/R_a$ where R_a is the radius of the inner electrons of the target atom. In this case $U_e \approx 110$ eV depending on R_a [Eng88]. The currently accepted maximum value for U_e is calculated from the adiabatic limit [Bra90]. In this case U_e is equal to the difference in electron binding energy between the target and the combined projectile-target system and is calculated to be 119 eV for the ^{3}He$(d,p)^4$He reaction. At present there are no other models that predict a higher value for the screening potential.

The screening potential was calculated from the R-matrix cross sections using the following procedure. The astrophysical S-factor was determined from equation 6.28 and then parameterized by the expression

$$S(E) = 6.70 + 2.43 \times 10^{-2} E + 2.06 \times 10^{-4} E^2 \qquad (6.31)$$

where E is the center-of-mass energy in keV and $S(E)$ is in units of MeV-b.

The experimental $S(E)$ data reported in [Lan96][11] were used and the data were allowed to scale because the S-factor calculated from the R-matrix parameterization is noticeably larger than the data. The screening potential was found using equation 6.30 by varying both U_e and a scale factor to the experimental data until the reduced chi squared was minimized. It was found that $U_e = 164 \pm 30$ eV along with a scale factor of 1.17 produced a reduced chi squared of 4.5. The error is defined as the difference in the screening potential when the chi squared increased by one from the best fit value. This screening potential is much larger than the adiabatic limit of 119 eV. Making the agreement worse is that the approximations used to derive equation 6.30 leads to an underprediction of the screening potential [Lan96]. To correct this determination, the screening potential was calculated from equation 6.29 resulting in $U_e = 177 \pm 29$ eV with a scale factor of 1.165 and a reduced χ^2 of 4.5, as shown in Figure 6.13.

The value of the screening potential is found to be larger than the adiabatic limit and also larger than the determination of 130 ± 8 eV by [Lan96]. The determination by [Lan96] differed from the present calculation in two ways, first the data were not normalized and second a systematic error of 3.8% due to calorimeter and pressure measurements was added in quadrature to the statistical error. This calculation can be repeated using the present procedure by using the bare nuclear cross section extrapolation by [Chu93] in place of the R-matrix calculation. The value of U_e in this case was found to be 170 ± 28 eV[12] using a scale factor of 1.03 and resulting in a reduced χ^2 of 4.7, as shown in Figure 6.14.

[11]These data were originally reported in [Eng88] and corrected in [Lan96] to take into account new stopping-power measurements [Gol91]. The data used in the present calculation had only statistical errors included.

[12]The screening value was also calculated using the errors assumed in [Lan96] and allowing only a scale factor. It was found in this case that a much better fit was obtained by scaling the data by 1.03 with $U_e = 165$ eV and a reduced χ^2 of 0.3.

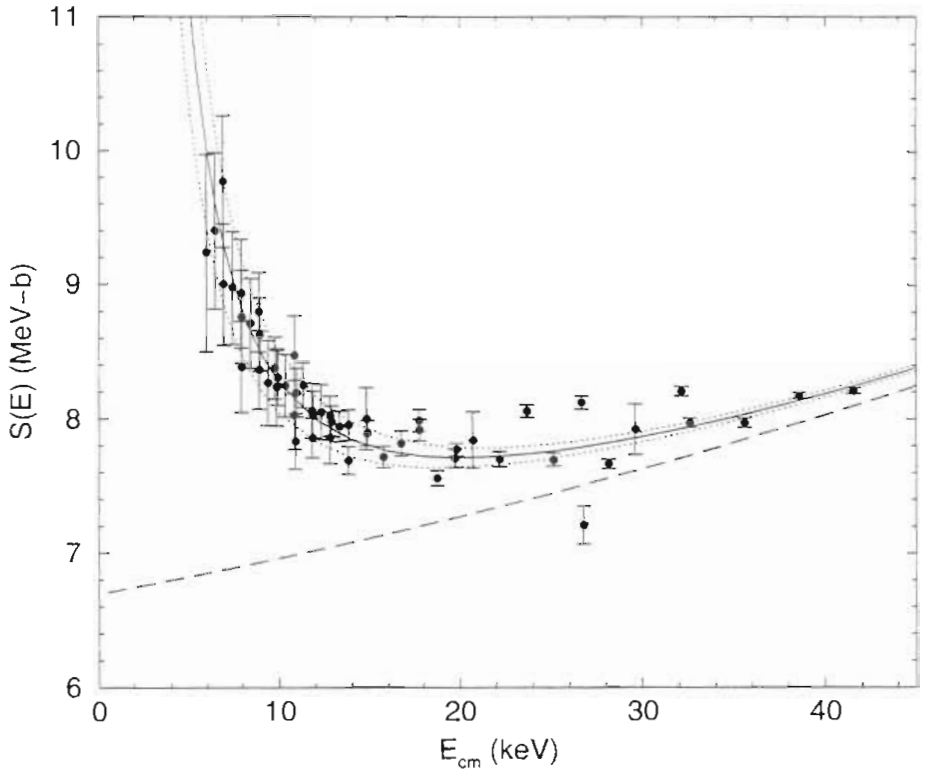

Figure 6.13: Electron screening calculations using R-matrix calculations for the bare nuclear cross section (dashed line) and the data from [Lan96] (solid circles). The data were scaled up by 16.5% resulting in $U_e = 177 \pm 29$ eV with a reduced χ^2 of 4.5. The solid line is the calculated enhancement for a screening potential of $U_e = 177$ eV while the dotted lines show the error.

The present calculations show that the screening values are larger than the adiabatic limit with both the extrapolation by [Chu93] and the R-matrix calculations of the bare nuclear cross section. One may question if scaling the data in these calculations is a valid procedure. There is a 7.1% overall uncertainty is the experimental data as quoted in [Eng88]. Certainly scaling the data by 3% as needed with the bare nuclear cross section of [Chu93] is justified. The 16.5% normalization needed with the R-matrix calculation is larger than the uncertainty but is not unreasonable considering that at the peak of the resonance

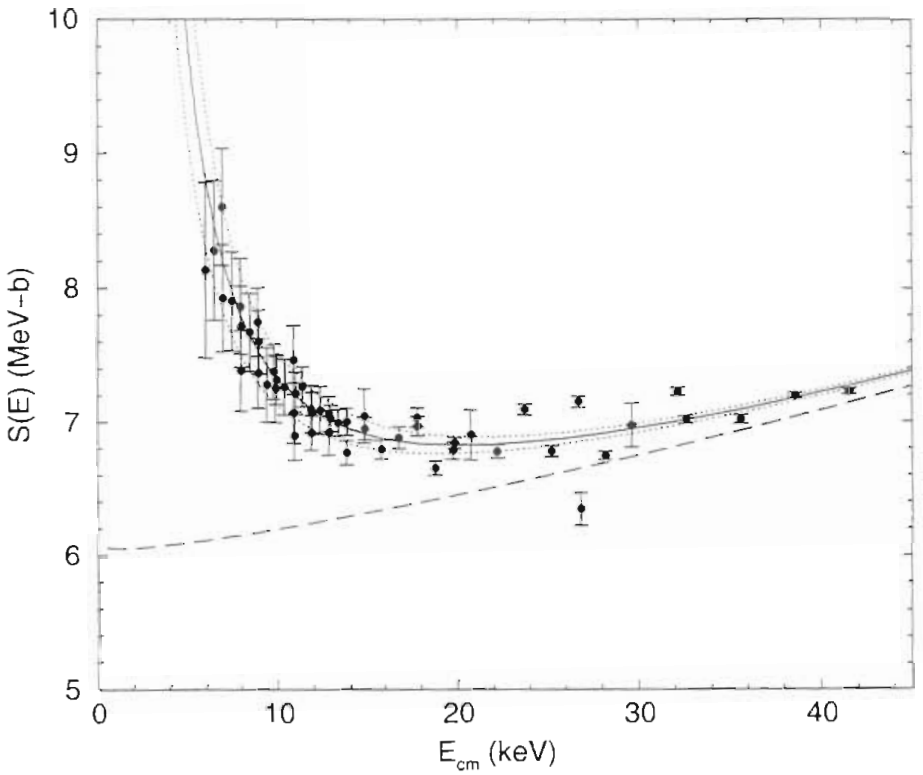

Figure 6.14: Electron screening calculations using the extrapolation from [Chu93] for the bare nuclear cross section (dashed line) and the data from [Lan96] (solid circles). The data were scaled up by 3% resulting in $U_e = 170 \pm 28$ eV with a reduced χ^2 of 4.4. The solid line is the calculated enhancement for a screening potential of $U_e = 170$ eV while the dotted lines show the error.

the experimental data conflict by as much as 30%, see Table 1.2.

In light of the present calculations, it appears that current theoretical calculations underpredict the screening potential. This underprediction of the screening potential is not new and is seen in several other reactions [Rol95]. A better understanding of screening effects requires additional efforts in theory as well as experiment.

Chapter 7

Summary and Future Work

A brief summary of the work is given along with a discussion of possible future work.

7.1 Conclusions

Angular distribution measurements of complete sets of analyzing powers and cross sections have been measured at very low energies ($60 \leq E \leq 641$ keV). Also an excitation function and an absolute determination of the cross section were completed. These data are the lowest-energy and highest-precision analyzing powers measured for the $^3\mathrm{He}(\vec{d},p)^4\mathrm{He}$ reaction. The higher-energy data are in fair agreement with the data of Gar74 but there are some minor discrepancies, especially among the A_{zz} data. The absolute cross section was measured to be 777 ± 33 mb at $E_d = 426$ keV. This result agrees with previous measurements and the new R-matrix parameterization.

The success of the measurements was possible because of several developmental projects. Target production using ion-implanted ^{3}He targets was developed. Also, the upgrade of the minitandem and completion of the high-voltage chamber was instrumental in achieving the higher energies or greater beam currents necessary to make the measurements possible. Two polarimeters, one to measure vector and the other tensor polarizations, were calibrated.

The data was used in an R-matrix analysis of the ^{5}Li system. This better defined the $J^\pi = \frac{3}{2}^+$ level located at $E_x = 16.86$ MeV in ^{5}Li (the level has shifted down by about $E_{cm} = 10$ keV). Also, the new R-matrix parameterization resulted in a solution that includes a new $\frac{1}{2}^+$ level located slightly below the $^3\mathrm{He} + d$ threshold. This level was not present in the previous R-matrix parameterization [Til98]. The R-matrix analysis provided evidence that at least up to D waves in the entrance channel are needed to describe the $^3\mathrm{He}(d,p)^4\mathrm{He}$ reaction. The $^2P_{\frac{3}{2}}$ entrance channel is most important for the P waves while the $^4D_{\frac{3}{2}}$ is most important for the D waves. The analyzing power data have also revealed a possible destructive interference in the $^2S_{\frac{1}{2}}$ channel involving a $J^\pi = \frac{1}{2}^-$ level in ^{5}Li.

Electron screening calculations using the bare nuclear cross section calculated from the new R-matrix analysis yield a U_e value of 177 ± 29 eV. This value is in disagreement with the theoretical calculation [Bra90] of 120 eV and a previously determined value [Lan96] of 130 ± 8 eV. Although, if the previously determined value of [Lan96] is recalculated in procedure consistent with the present analysis (as discussed in Section 6.3) a value of 170 ± 28 eV is calculated.

7.2 Possible future work

On the experimental side, there seems little reason to measure more analyzing powers for the $^3\mathrm{He}(d,p)^4\mathrm{He}$ reaction. More than one set of measurements measured by different groups exist at energies greater than 300 keV. Continuing the measurements to lower energies would require considerable effort because the cross section drops very rapidly with decreasing energy. One case where measurement of the analyzing powers at lower energies might be useful would be for developing polarimetry, but since other reactions are more efficient in this energy range this is not a good justification.

Measurements of other polarization observables, although very difficult, would

be useful. In particular, a measurement of the polarization transfer coefficient, K_y^y, at zero degrees along with other previously measured observables would allow a complete determination of the matrix elements [San96] at zero degrees. This is possible because at zero degrees several of the matrix elements vanish allowing the remaining ones to be determined. Knowledge of these matrix elements would put very strong constraints on the reaction models [San96]. Steps have been taken at TUNL to calibrate a very high efficiency polarimeter that is capable of measuring K_y^y.

Continuation of the R-matrix analysis is needed to better understand the $\frac{1}{2}^+$ level slightly below the $^3\mathrm{He} + d$ threshold. Also, extending the R-matrix parameterization to even higher energies is desirable in order to gain more information about higher energy levels in ^{5}Li.

Calculations of the effect on the analyzing powers of direct verses resonant processes is currently being undertaken by Santos *et al.* [San96]. If an understanding of this process is developed, it can be used in other reactions that have astrophysical significance.

Finally, more work needs to be done to understand the differences between the measured electron screening potential and the theoretically predicted values. On the experimental side this requires accurate measurements of cross sections at extremely low energies and also an excellent ability to determine accurately the reaction energy. Theoretically, more complex models need to be developed that take into account the atomic physics effects more accurately.

Appendix A

Polarimetry

Two polarimeters were calibrated for use in the high-voltage chamber to measure the polarization of deuteron beams. One polarimeter uses the ^{3}He$(d,p)^4$He reaction for measurement of the tensor polarization [Gei95] and the other polarimeter uses the D(d,p)T reaction to measure the vector polarization.

A.1 Polarimeter design

The deuteron tensor polarimeter uses an ion-implanted ^{3}He target, as described in section 2.3.1. The protons are detected by two 600-mm^2 silicon solid-state detectors fixed at a mean angle of 17.5° to the right and left of the incoming beam. A tantalum foil was placed on a 0.42-cm-diameter circular collimator in front of the detector to prevent scattered particles from entering the detector and to slow the protons down so that they will stop in the detector. The detectors have an angular opening of ±9° and a solid angle of 0.087 sr. A diagram of the scattering chamber with the polarimeter inserted is shown in Figure A.1. Due to the fact that the protons emerge from the ^{3}He$(d,p)^4$He reaction with a large energy, $E_p > 12$ MeV, the proton peak is the only particle detected, as shown in Figure A.2.

The deuteron vector polarimeter uses a deuterated carbon foil for the target as described in Section 2.3.2. This polarimeter is a modified version of one used

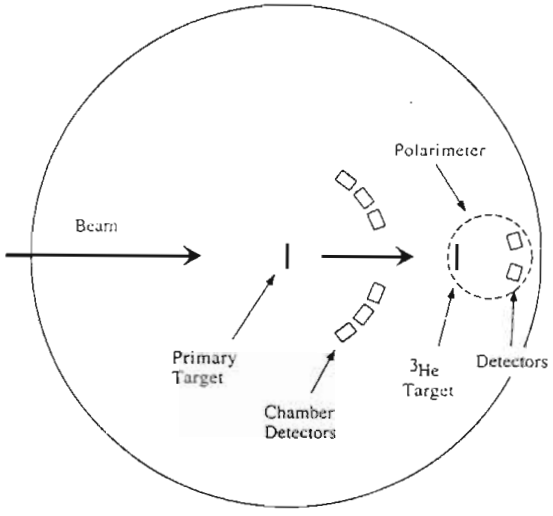

Figure A.1: Schematic view of the high-voltage chamber containing the deuteron tensor polarimeter.

to measure proton polarization [Bru97] by using a different target and a different thickness foil in front of the detectors. The reaction products were detected with two 100-mm^2 silicon detectors placed at 90° to the right and left of the beam. Several deuterated targets were placed on a target ladder that was rotated 30° relative to the beam to allow the reaction products to enter the detectors. A 5-μm mylar foil was placed on a 0.098 × 0.197-cm-oval collimator in front of the detectors to prevent elastically scattered deuterons from entering the detectors. The detectors have an angular acceptance of ±3.7° and a solid angle of 0.10 sr. The vector polarimeter is placed in the back of the high-voltage chamber similarly as shown by Figure A.1, for the tensor polarimeter.

As seen in a typical polarimeter spectra, Figure A.3, one peak from each of the D(d,p)T, D(d,t)p, and ^{12}C$(d,p)^{13}$C reactions are detected. This is advantageous at most energies because polarization information can be obtained from all the peaks. At energies above 550 keV this becomes a problem because the D(d,p)T peak and the ^{12}C$(d,p)^{13}$C peak start to merge into each other, as seen in the reaction kinematics, Figure A.4.

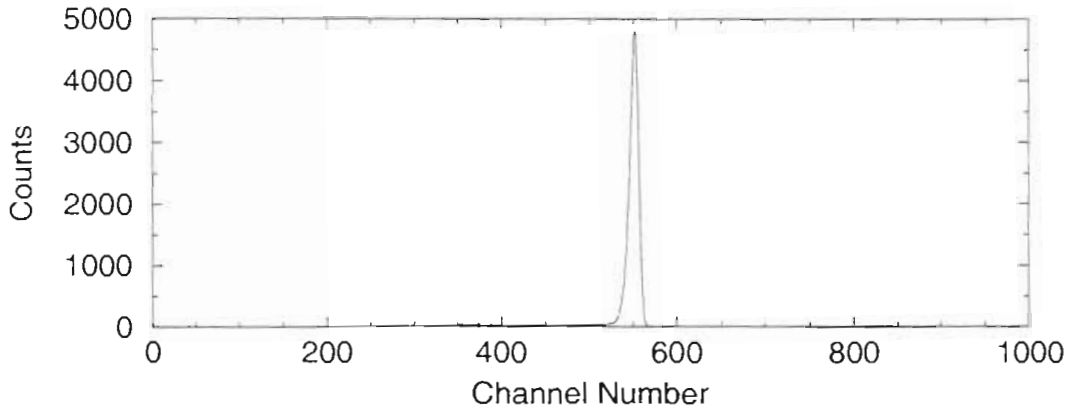

Figure A.2: Typical spectrum for the ^{3}He$(d,p)^4$He reaction in the deuteron tensor polarimeter. The energy of the deuteron beam was 265 keV.

A.2 Calibration

The absolute calibration of the polarimeters was accomplished by accelerating a deuteron beam to high energies through the TUNL FN Tandem accelerator into a well calibrated ^{3}He$(d,p)^4$He polarimeter [Ton81] to determine the beam polarization. The beam was then redirected through the low-energy bay into the high-voltage chamber where the polarimeters were calibrated. There is a possibility that the polarization of the beam at high energies may be different than that used in LEBF. For example, different tuning between the two energies may result in the sampling of different portions of the beam that have different polarizations. From experience. this effect should be small because the beam is well collimated by slits at the entrance of the scattering chambers and care is taken to reach a good tune every time. There may also be different depolarization effects between the two energies. For example, the charge exchange process between the stripper foils takes place at different energies and when the minitandem is grounded no stripper foil is used. Again from experience, this effect is expected to be small because measurements of the polarization with both negative and positive beam in the high-voltage chamber give same results within errors. The

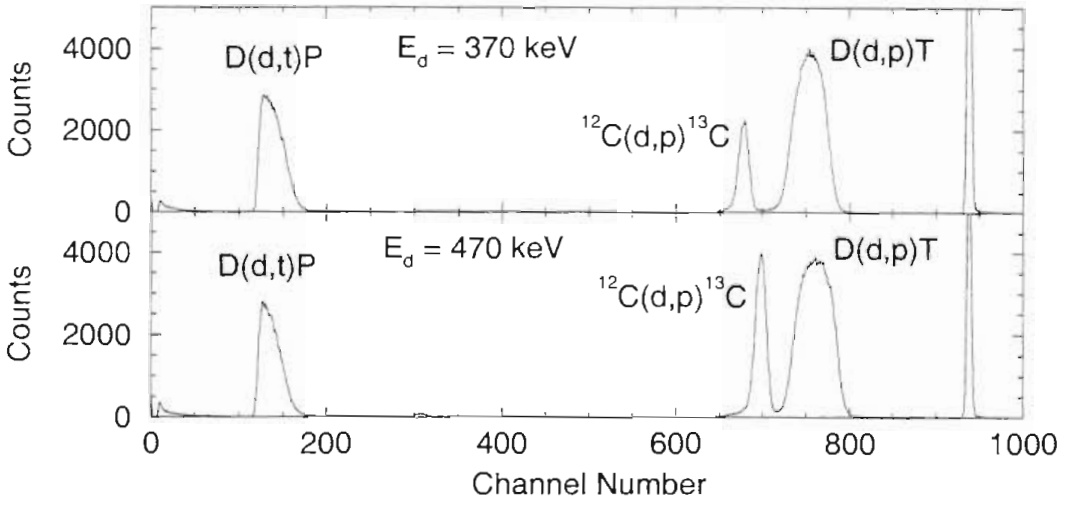

Figure A.3: Typical spectrum for the deuteron vector polarimeter taken at E_d = 370 keV and at E_d = 470 keV. The three reaction peaks are resolved and the peak near channel 940 is due to the pulser.

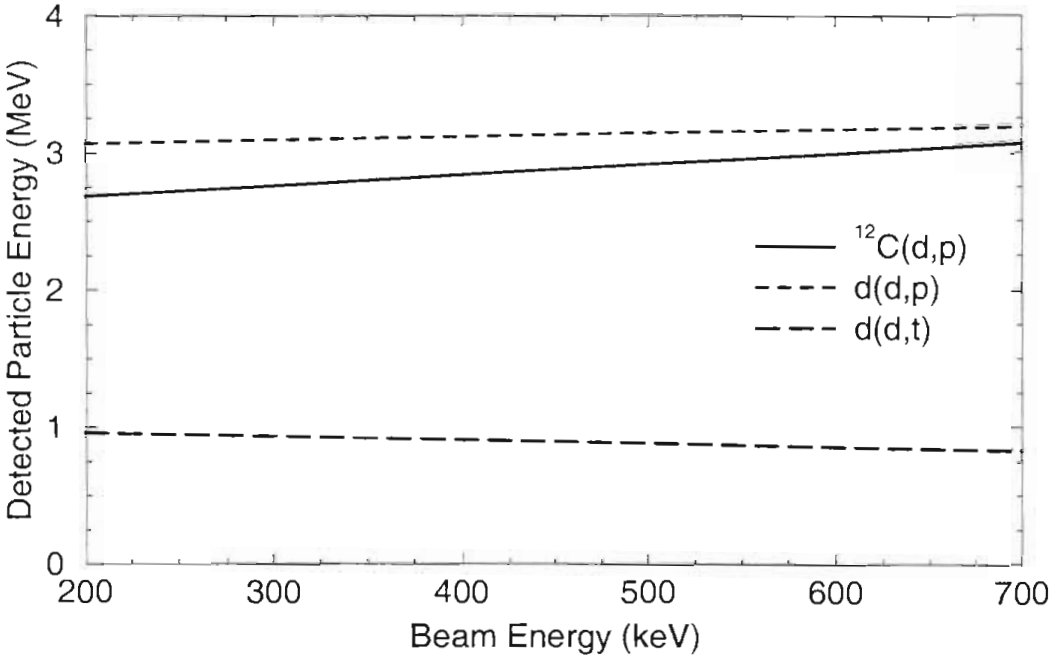

Figure A.4: Kinematics for the three different reactions that occur in the deuteron vector polarimeter.

polarization of the beam is therefore assumed to be the same at both the high and low energies.

In the calibration of the tensor polarimeter, the beam was first accelerated into a ^{3}He$(d,p)^4$He polarimeter at $E_d = 7$ MeV in an A_{yy} configuration to measure the beam polarization. Then the beam was directed into the high-voltage chamber and A_{yy} was measured at $E_d = 318$ keV. Next the Wien filter was adjusted to measure A_{zz} in the high-voltage chamber. The Wien filter was then adjusted again for measurement of the polarization in the high-energy ^{3}He$(d,p)^4$He polarimeter at $E_d = 7\ MeV$ in an A_{zz} configuration. The other calibration points were obtained by retuning the beam to $E_d = 318$ keV in order to determine the beam polarization. The average tensor polarization was measured to be -0.74 and 0.78 for the two polarized states. For the calibration of the A_{xz} points the beam polarization was first determined in the high-voltage chamber in an A_{zz} configuration. The Wien filter was then adjusted and A_{xz} for the polarimeter was calibrated at $E_d = 424$ keV. The A_{xz} calibration point at $E_d = 200$ keV was measured with positive beam from the source and the polarization was determined from an A_{zz} configuration.

The procedure for calibrating the vector polarimeter is very similar to the tensor polarimeter. The beam was accelerated into the high-energy ^{3}He$(d,p)^4$He polarimeter at 10 MeV to determine the vector polarization. The beam was then redirected onto the vector polarimeter in the high-voltage chamber where the analyzing powers for the three reactions was measured for several beam energies. After the analyzing powers were measured, the beam polarization was checked with the high-energy ^{3}He$(d,p)^4$He polarimeter. The average vector polarizations were -0.56 and 0.50 for the two polarized states while the tensor polarizations were found to be no more than 0.05 for both polarization states.

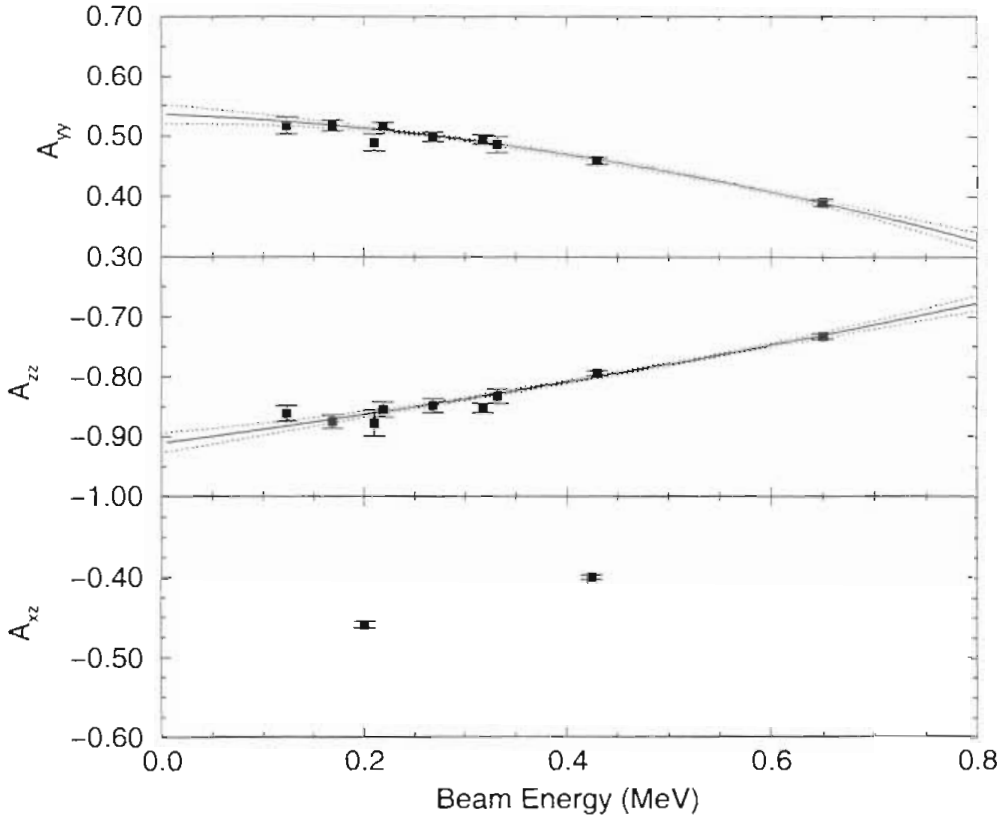

Figure A.5: Energy dependence of the tensor analyzing powers. The solid line shows the results of the second order polynomial fit and the dotted lines show the error in the fit.

A.3 Results

A.3.1 Data

All the analyzing powers were calibrated over a wide range of energies, except for A_{xz} which was only calibrated at two energies. The data are given in Table A.1 and are graphed in Figures A.5 and A.6.

Polarimeter tensor analyzing powers						
$E_d(keV)$	A_{yy}	$\Delta\ A_{yy}$	A_{zz}	$\Delta\ A_{zz}$	A_{xz}	$\Delta\ A_{xz}$
123	0.517	0.014	−0.862	0.013		
169	0.517	0.009	−0.875	0.011		
200					−0.459	0.004
210	0.489	0.014	−0.878	0.022		
219	0.516	0.006	−0.855	0.013		
269	0.498	0.008	−0.849	0.012		
318	0.494	0.008	−0.853	0.008		
332	0.486	0.013	−0.833	0.012		
424					−0.400	0.003
430	0.459	0.006	−0.794	0.004		
650	0.390	0.005	−0.732	0.005		

Polarimeter vector analyzing powers						
	$\mathrm{D}(d,p)\mathrm{T}$		$^{12}\mathrm{C}(d,p)^{13}\mathrm{C}$		$D(d,t)P$	
$E_d(keV)$	A_y	$\Delta\ A_y$	A_y	$\Delta\ A_y$	A_y	$\Delta\ A_y$
270	0.249	0.007	−0.049	0.036	−0.154	0.010
370	0.255	0.004	−0.273	0.007	−0.134	0.006
380	0.252	0.005	−0.266	0.015		
430	0.259	0.003	−0.361	0.006	−0.129	0.007
470	0.258	0.004	−0.406	0.006	−0.116	0.007
480	0.255	0.005	−0.410	0.008		
530	0.250	0.005	−0.441	0.007		

Table A.1: Analyzing powers for the vector and tensor polarimeters. The error listed in the table includes only statistical errors.

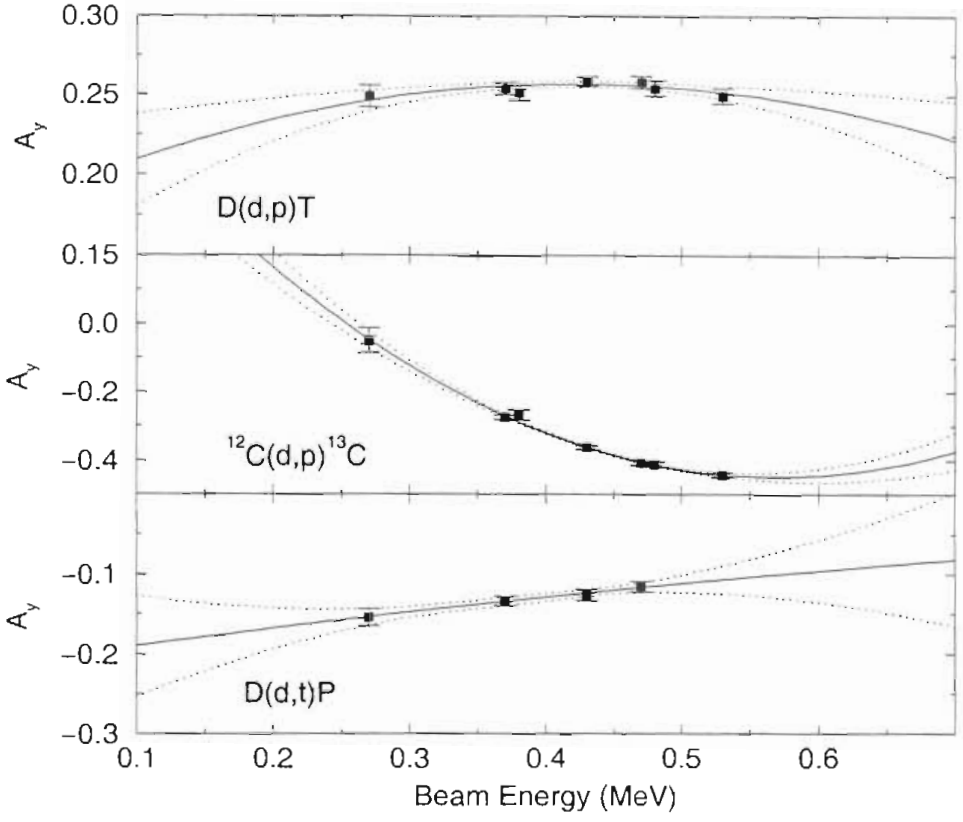

Figure A.6: Energy dependence of the vector analyzing powers. The solid line shows the results of the second order polynomial fit and the dotted lines show the error in the fit.

A.3.2 Polynomial fits

The polarimeter analyzing powers were found to be smoothly varying with energy. This smooth energy dependence allows the analyzing powers to be described by a second order polynomial fit. The analyzing powers were fit to $A(E) = a_1 + a_2 E + a_3 E^2$ where the energy, E, is in MeV and A is one of the analyzing powers. The fitting procedure used is described in [Bev92]. The fit coefficients are shown in Table A.2.

The error associated with the polynomial fit is determined from the error

Analyzing power		a_1	a_2	a_3
A_{yy}		0.5358	−0.0680	−0.2416
A_{zz}		−0.9107	0.2172	0.0934
A_y	$D(d,p)$	0.1749	0.3890	−0.4589
A_y	$^{12}C(d,p)$	1.0062	−5.1036	4.4759
A_y	$D(d,t)$	−0.2129	0.2396	−0.0747

Table A.2: Second-order polynomial fit coefficients to the polarimeter analyzing powers.

A	ϵ_{11}	ϵ_{12}	ϵ_{13}	ϵ_{22}	ϵ_{23}	ϵ_{33}
A_{yy}	2.720e-4	-1.462e-3	1.642e-3	8.316e-3	-9.610e-3	1.138e-2
A_{zz}	2.765e-4	-1.317e-3	1.410e-3	6.791e-3	-7.633e-3	8.921e-3
A_y D(d,p)	2.481e-3	-1.201e-2	1.422e-2	5.900e-2	-7.081e-2	8.598e-2
A_y ^{12}C(d,p)	2.546e-2	-1.154e-1	1.289e-1	5.266e-1	-5.918e-1	6.689e-1
A_y D(d,t)	1.388e-2	-7.407e-2	9.611e-2	4.000e-1	-5.239e-1	6.919e-1

Table A.3: Error matrix for the second order polynomial fit to the polarimeter analyzing powers, A.

matrix by

$$\Delta A = \epsilon_{11} + \epsilon_{22}E^2 + \epsilon_{33}E^4 + 2(\epsilon_{12}E + \epsilon_{13}E^2 + \epsilon_{23}E^3), \qquad \text{(A.1)}$$

where the energy, E, is in MeV and the ϵ are the error matrix coefficients given in Table A.3. The fits and their associated error are shown in Figures A.5 and A.6.

The absolute accuracy of the polarimeters depends on the accuracy quoted for the high-energy polarimeter [Ton81]. For the tensor polarimeter this is 3.1% and for the vector polarimeter it is 2.1%. Added in quadrature to this value is a 3% error estimated from uncertainties associated with the calibration process. The total error for tensor polarimeter is 4.3% and for the vector polarimeter is 3.7%.

Appendix B

Data Tables

The analyzing powers, A_y, A_{yy}, A_{xz}, and A_{zz} for the ^{3}He$(d,p)^4$He reaction are listed in the Tables B.1 through B.5. The errors listed in these tables include only statistical errors. The data are also subjected to a systematic error of 4.3% for the tensor analyzing powers and 3.7% for the vector analyzing power, as described in Section 4.2. The five reaction energies are determined as described in Section 4.4. The relative cross section data are shown in Tables B.6 and B.7. These data points contain statistical errors only. Listed at the bottom of each table is a value obtained from the new R-matrix parameterization to scale the data to absolute cross section values. The excitation function data is listed in Tables B.8 and B.9 and contains only statistical errors. A scale error of 4.3%, as discussed in Section 4.3.3, has to be added to the data.

$E = 60$ keV								
Θ_{cm}	A_y	ΔA_y	A_{yy}	ΔA_{yy}	A_{zz}	ΔA_{zz}	A_{xz}	ΔA_{xz}
0.0					−1.031	0.014		
20.4	0.0038	0.0037	0.561	0.019	−0.847	0.012	−0.529	0.023
40.7	0.0072	0.0025	0.533	0.013	−0.351	0.013	−0.750	0.016
50.8					−0.043	0.031		
60.9	0.0147	0.0041	0.500	0.022	0.165	0.024	−0.604	0.026
70.0							−0.429	0.024
71.0	0.0201	0.0041	0.523	0.026	0.341	0.019		
90.0							0.082	0.016
91.0	0.0199	0.0025	0.500	0.017	0.460	0.017		
110.0							0.501	0.025
111.0	0.0176	0.0031	0.490	0.029	0.261	0.026		
120.9	0.0187	0.0028	0.495	0.022	0.062	0.022	0.654	0.023
140.7	0.0175	0.0020	0.461	0.015	−0.412	0.014	0.656	0.016
160.4	0.0078	0.0030	0.494	0.023	−0.760	0.019	0.407	0.024

Table B.1: Analyzing power data for the ^{3}He$(d,p)^4$He reaction at 60 keV.

$E = 99$ keV								
Θ_{cm}	A_y	ΔA_y	A_{yy}	ΔA_{yy}	A_{zz}	ΔA_{zz}	A_{xz}	ΔA_{xz}
0.0			0.535	0.007	−1.081	0.017		
20.5	0.0012	0.0014	0.535	0.007	−0.895	0.011	−0.529	0.007
40.9	0.0042	0.0009	0.523	0.007	−0.355	0.010	−0.776	0.006
61.2	0.0075	0.0016	0.497	0.011	0.202	0.015	−0.616	0.011
71.3	0.0144	0.0019	0.498	0.010	0.373	0.011	−0.405	0.009
91.4	0.0164	0.0013	0.494	0.007	0.502	0.008	0.108	0.006
111.3	0.0200	0.0021	0.489	0.011	0.306	0.011	0.526	0.010
121.2	0.0220	0.0017	0.476	0.010	0.042	0.012	0.646	0.011
131.0					−0.138	0.013		
140.9	0.0187	0.0015	0.455	0.007	−0.393	0.010	0.684	0.007
150.7					−0.600	0.022		
160.5	0.0091	0.0018	0.459	0.010	−0.775	0.017	0.420	0.012

Table B.2: Analyzing power data for the ^{3}He$(d,p)^4$He reaction at 99 keV.

$E = 199$ keV								
Θ_{cm}	A_y	ΔA_y	A_{yy}	ΔA_{yy}	A_{zz}	ΔA_{zz}	A_{xz}	ΔA_{xz}
0.0			0.509	0.036	−1.050	0.042		
10.3	−0.0009	0.0006	0.538	0.033	−0.956	0.032	−0.313	0.009
20.7			0.540	0.024	−0.859	0.023	−0.540	0.010
31.0	0.0006	0.0007	0.552	0.038	−0.543	0.040	−0.714	0.009
41.3			0.510	0.027	−0.312	0.027	−0.798	0.010
51.5	0.0055	0.0007	0.523	0.035	−0.097	0.040	−0.755	0.009
61.7			0.539	0.036	0.172	0.031	−0.623	0.011
71.8	0.0129	0.0007	0.513	0.033	0.387	0.036	−0.430	0.009
81.9			0.472	0.029	0.482	0.035	−0.168	0.009
92.0	0.0201	0.0007	0.526	0.038	0.463	0.043	0.098	0.010
101.9			0.446	0.035	0.443	0.042	0.339	0.009
111.8	0.0236	0.0007	0.436	0.037	0.274	0.042	0.523	0.011
121.7			0.463	0.035	0.054	0.033	0.670	0.008
129.5	0.0245	0.0007						
131.5			0.439	0.032	−0.151	0.036	0.730	0.011
141.3			0.458	0.041	−0.372	0.041	0.704	0.009
149.0	0.0182	0.0007						
151.0			0.433	0.036	−0.610	0.040	0.613	0.011
160.7			0.462	0.038	−0.779	0.037	0.449	0.009
168.4	0.0077	0.0007						
170.3			0.485	0.034	−0.853	0.036	0.241	0.010

Table B.3: Analyzing power data for the ^{3}He$(d,p)^4$He reaction at 199 keV.

$E = 424$ keV								
Θ_{cm}	A_y	ΔA_y	A_{yy}	ΔA_{yy}	A_{zz}	ΔA_{zz}	A_{xz}	ΔA_{xz}
0.0			0.481	0.012	−0.923	0.017		
10.5	−0.0008	0.0010	0.499	0.013	−0.900	0.014	−0.258	0.006
21.0			0.477	0.008	−0.756	0.010	−0.463	0.008
31.4	0.0007	0.0010	0.479	0.015	−0.576	0.016	−0.628	0.007
41.8			0.479	0.009	−0.320	0.011	−0.677	0.008
52.1	0.0050	0.0011	0.477	0.014	−0.093	0.016	−0.686	0.007
62.4			0.495	0.014	0.173	0.014	−0.572	0.006
72.6	0.0123	0.0007	0.469	0.010	0.318	0.015	−0.420	0.009
82.8			0.478	0.011	0.441	0.016	−0.201	0.008
92.8	0.0212	0.0007	0.483	0.012	0.482	0.016	0.049	0.009
102.8			0.464	0.013	0.414	0.019	0.296	0.008
112.6	0.0244	0.0008	0.481	0.012	0.303	0.016	0.487	0.011
122.4			0.493	0.013	0.098	0.012	0.641	0.011
130.2	0.0242	0.0009						
132.1			0.497	0.012	−0.119	0.011	0.667	0.009
141.8			0.469	0.014	−0.398	0.015	0.719	0.011
149.5	0.0195	0.0009						
151.4			0.521	0.014	−0.608	0.013	0.652	0.009
161.0			0.499	0.013	−0.821	0.014	0.465	0.011
168.6	0.0080	0.0010						
170.5			0.505	0.013	−0.921	0.012	0.359	0.010

Table B.4: Analyzing power data for the ^{3}He$(d,p)^4$He reaction at 424 keV.

$E = 641$ keV								
Θ_{cm}	A_y	ΔA_y	A_{yy}	ΔA_{yy}	A_{zz}	ΔA_{zz}	A_{xz}	ΔA_{xz}
0.0			0.469	0.012	−0.852	0.015		
10.6	0.0014	0.0008	0.444	0.013	−0.798	0.018	−0.226	0.011
21.2			0.418	0.008	−0.695	0.008	−0.375	0.011
31.7	0.0051	0.0008	0.418	0.012	−0.504	0.016	−0.533	0.011
42.2			0.420	0.009	−0.328	0.008	−0.589	0.010
52.6	0.0092	0.0008	0.410	0.011	−0.112	0.016	−0.592	0.012
63.0			0.394	0.012	0.114	0.010	−0.529	0.010
73.2	0.0127	0.0008	0.425	0.013	0.254	0.013	−0.436	0.008
83.4			0.412	0.011	0.432	0.013	−0.266	0.008
93.4	0.0170	0.0008	0.423	0.011	0.466	0.016	−0.072	0.008
103.4			0.445	0.013	0.483	0.016	0.164	0.008
113.2	0.0195	0.0009	0.452	0.012	0.352	0.016	0.386	0.010
123.0			0.480	0.019	0.176	0.013	0.592	0.012
130.7	0.0197	0.0009						
132.2			0.490	0.013	−0.074	0.017	0.730	0.012
142.2			0.526	0.022	−0.358	0.019	0.740	0.013
149.8	0.0162	0.0009						
151.7			0.500	0.015	−0.631	0.018	0.653	0.013
161.2			0.546	0.020	−0.874	0.017	0.521	0.013
168.7	0.0063	0.0010						
170.6			0.530	0.014	−1.016	0.017	0.276	0.013

Table B.5: Analyzing power data for the $^3\mathrm{He}(d,p)^4\mathrm{He}$ reaction at 641 keV.

$E = 60$ keV		
Θ_{cm}	σ	$\Delta\sigma$
10.2	1.021	0.020
30.5	1.022	0.015
40.7	0.998	0.023
60.9	0.973	0.023
81.1	0.966	0.020
101.1	1.027	0.021
135.8	1.038	0.026
150.5	1.011	0.028
155.5	1.026	0.019
170.2	1.049	0.021

Multiply by 0.18 mb/sr

$E = 99$ keV		
Θ_{cm}	σ	$\Delta\sigma$
0.0	1.019	0.019
10.2	1.007	0.019
20.5	1.026	0.011
30.7	1.012	0.011
40.9	1.012	0.011
51.1	1.010	0.011
61.2	1.007	0.020
71.3	0.978	0.021
81.4	1.022	0.022
91.4	1.014	0.013
101.4	1.028	0.016
111.3	0.993	0.015
121.2	0.984	0.019
131.1	0.992	0.014
140.9	1.005	0.011
150.7	1.001	0.020
160.5	1.015	0.014
170.2	1.006	0.014

Multiply by 1.59 mb/sr

Table B.6: Cross section angular distribution data for the ^{3}He$(d,p)^4$He reaction at 60 and 99 keV. To convert to absolute cross section multiply the relative cross sections by the value given at the bottom of each table.

$E = 199$ keV			$E = 424$ keV			$E = 641$ keV		
Θ_{cm}	σ	$\Delta\sigma$	Θ_{cm}	σ	$\Delta\sigma$	Θ_{cm}	σ	$\Delta\sigma$
0.0	1.0136	0.0074	0.0	1.0075	0.0061	0.0	0.9822	0.0055
10.3	1.0306	0.0041	10.5	0.9953	0.0041	10.6	0.9773	0.0035
20.6	1.0259	0.0043	20.9	0.9939	0.0040	21.2	0.9809	0.0038
30.9	1.0108	0.0074						
41.2	1.0306	0.0040	41.8	0.9822	0.0039	42.2	0.9761	0.0037
51.5	1.0297	0.0047	52.1	0.9910	0.0043	52.6	0.9903	0.0041
61.6	1.0401	0.0060	62.4	0.9941	0.0043	62.9	0.9719	0.0052
71.8	1.0130	0.0060	72.6	0.9828	0.0060	73.2	0.9464	0.0062
81.9	1.0010	0.0057	82.7	0.9766	0.0060	83.3	0.9635	0.0062
91.9	1.0150	0.0064	92.8	0.9720	0.0064	93.4	0.9594	0.0062
101.9	1.0055	0.0057	102.7	0.9690	0.0064	103.3	0.9427	0.0062
111.8	1.0013	0.0057	112.6	0.9631	0.0067	113.2	0.9324	0.0059
121.6	1.0048	0.0059	122.4	0.9585	0.0064	122.9	0.9238	0.0060
131.5	0.9911	0.0056	132.1	0.9517	0.0059	132.6	0.9232	0.0043
141.2	0.9951	0.0039	141.8	0.9596	0.0065	142.2	0.9162	0.0042
150.9	0.9943	0.0058	151.4	0.9463	0.0042	151.7	0.9089	0.0043
160.6	0.9839	0.0052	160.9	0.9485	0.0065	161.2	0.9023	0.0057
170.3	0.9879	0.0057	170.5	0.9426	0.0060	170.6	0.9041	0.0058
Multiply by 16.2 mb/sr			Multiply by 66.2 mb/sr			Multiply by 43.6 mb/sr		

Table B.7: Cross section angular distribution data for the ^{3}He$(d,p)^4$He reaction at 199, 424, and 641 keV. To convert to absolute cross section multiply the relative cross sections by the value given at the bottom of each table.

^{3}He$(d,p)^4$He Excitation Data					
E_d (keV)	σ (mb)	$\Delta\sigma$	E_d (keV)	σ (mb)	$\Delta\sigma$
254.5	398.6	2.9	457.7	769.6	3.0
274.1	478.2	5.9	475.2	727.9	4.6
293.7	545.1	4.4	477.6	748.7	5.0
313.4	613.1	7.2	495.1	717.7	4.9
316.5	624.3	2.4	497.5	715.4	4.0
333.1	671.9	6.0	514.9	678.0	5.8
336.1	687.1	3.7	517.5	689.3	3.6
352.9	727.7	9.7	537.4	649.8	3.6
372.6	736.4	9.3	557.3	624.0	2.3
375.8	757.1	3.2	577.2	593.6	3.3
395.6	770.3	6.0	597.1	563.8	3.0
415.5	777.0	6.1	617.0	540.5	3.4
435.4	767.6	5.5	636.9	510.2	2.9
455.3	759.6	2.6	646.7	495.5	2.8

Table B.8: Excitation function for the ^{3}He$(d,p)^4$He reaction.

	$D(^3He, p)^4He$		$D(^3He, ^4He)p$	
E_d (keV)	σ (mb)	$\Delta\sigma$	σ (mb)	$\Delta\sigma$
244.7	347.9	7.9	337.5	6.9
283.6	513.0	10.5	510.3	9.2
296.6	548.7	11.6	532.9	10.0
348.6	721.7	14.2	685.6	12.0
361.6	744.5	14.7	730.5	12.6
400.7	783.7	15.9	774.9	13.6
420.3	777.3	6.5	778.7	5.6
423.7	777.0	4.8	777.3	4.1
452.9	745.3	9.7	759.2	8.3
475.9	750.6	10.6	764.6	9.1
504.9	685.6	14.2	674.0	11.8
528.1	673.2	14.1	674.8	8.2
580.3	578.3	12.0	577.2	6.9
632.6	480.0	11.3	498.7	6.6
684.7	426.5	9.9	441.7	5.7

Table B.9: Excitation function for the $D(^3He, p)^4He$ and $D(^3He, ^4He)p$ reactions.

REFERENCES

[Ajz88] F. Ajzemberg-Selove, Nucl. Phys. **A490**, 1 (1988).

[Alm61] O. Almen and G. Bruce, Nucl. Instr. Meth. **11**, 257 (1961).

[And77] H. H. Anderson and J. F. Ziegler, *The Stopping and Ranges of Ions in Matter. III.* Pergamon Press, New York, 1977.

[And81] H. H. Anderson and H. L. Bay, in *Sputtering by Particle Bombardment I*, edited by R. Behrisch, page 145, Springer, Heidelberg, 1981.

[Ang93] C. Angulo, S. Engstler, G. Raimann, C. Rolfs, W. H. Schulte, and E. Somorjai, Z. Phys. **A345**, 231 (1993).

[Ass87] H. J. Assenbaum, K. Langanke, and C. Rolfs, Z. Phys. **A327**, 461 (1987).

[Bar64] A. C. L. Barnard, C. M. Jones, and J. L. Weil, Nucl. Phys. **50**, 604 (1964).

[Bev92] P. R. Bevington and D. K. Robinson, *Data Reduction and Error Analysis for the Physical Sciences*, McGraw-Hill, New York, second edition, 1992.

[Bie80] J. P. Biersack and L. G. Haggmark, Nucl. Instr. Meth. **174**, 257 (1980).

[Bit90] M. Bittcher, W. Grüebler, V. König, P. A. Schmelzbach, B. Vuaridel, and L. Ulbricht, Few Body Systems **9**, 165 (1990).

[Bla93] T. C. Black, B. E. Hendrix, E. R. Crosson, K. A. Fletcher, H. J. Karwowski, and E. J. Ludwig, Nucl. Instr. Meth. **A333**, 239 (1993).

[Bla95] T. C. Black, Ph.D. thesis, University of North Carolina at Chapel Hill, 1995, Available from University Microfilms, Ann Arbor, Michigan.

[Blü89] G. Blüge, K. Langanke, H. G. Reusch, and C. Rolfs, Z. Phys. **A333**, 219 (1989).

[Blü90a] G. Blüge and K. Langanke, Phys. Rev. **C41**, 1191 (1990).

[Blü90b] G. Blüge, K. Langanke, M. Plagge, K. R. Nyga, and H. P. gen. Schieck, Phys. Lett. **B238**, 137 (1990).

[Bon52] T. W. Bonner, J. P. Conner, and A. B. Lillie, Phys. Rev. **88**, 473 (1952).

[Bra90] L. Bracci, G. Fiorentini, V. S. Melezhik, G. Mezzorani, and P. Quarati, Nucl. Phys. **A513**, 316 (1990).

[Bro54] R. J. S. Brown, K. F. Famularo, H. D. Holmgren, D. Rankin, and T. F. Stratton, Phys. Rev. **96**, 80 (1954).

[Bro66] L. Brown, H. A. Christ, and H. Rudin, Nucl. Phys. **79**, 459 (1966).

[Bro67] L. Brown and W. Trächslin, Nucl. Phys. **A90**, 334 (1967).

[Bro90] R. E. Brown and N. Jarmie, Phys. Rev. **C41**, 1391 (1990).

[Bru95a] C. R. Brune, "New energy calibration of the minitandem", TUNL internal report, 1995.

[Bru95b] C. R. Brune, "Energy calibration of the high-voltage scattering chamber", TUNL internal report, 1995.

[Bru97] C. R. Brune, H. J. Karwowski, and E. J. Ludwig, Nucl. Instr. Meth. **A389**, 421 (1997).

[Chu93] G. S. Chulick, Y. E. Kim, R. A. Rice, and M. Rabinowitz, Nucl. Phys. **A551**, 255 (1993).

[Cla73] J. F. Clare, Nucl. Phys. **A217**, 342 (1973).

[Cle95a] T. B. Clegg, H. J. Karwowski, S. K. Lemieux, R. W. Sayer, E. R. Crosson, W. M. Hooke, C. R. Howell, H. W. Lewis, A. W. Lovette, H. J. Pfutzner, K. A. Sweeton, and W. S. Wilburn, Nucl. Instr. Meth. **A357**, 200 (1995).

[Cle95b] T. B. Clegg, W. M. Hooke, E. R. Crosson, A. W. Lovette, H. L. Middleton, H. G. Pfutzner, and K. A. Sweeton, Nucl. Instr. Meth. **A357**, 212 (1995).

[Con84] H. E. Conzett, in *Few Body Problems in Physics*, edited by B. Zeitnitz, volume II, page 539, 1984.

[Con85] H. E. Conzett, in *6th International Symposium on Polarization Phenoma in Nuclear Physics*, page 98, 1985.

[Csó97] A. Csótó and G. M. Hale, Phys. Rev. **C55**, 536 (1997).

[Cze97] K. Czerski, A. Huke, H. Bucka, P. Heide, G. Ruprecht, and B. Unrau, Phys. Rev. **C55**, 1517 (1997).

[Dab88] A. E. Dabiri, Nucl. Instr. Meth. **A271**, 71 (1988).

[Dav80] J. A. Davies and P. R. Norton, Nucl. Instr. Meth. **168**, 611 (1980).

[Din95] D. C. Dinge, T. B. Clegg, E. R. Crosson, and H. W. Lewis, Nucl. Instr. Meth. **A357**, 195 (1995).

[Dri80] L. J. Dries, H. W. Clark, R. Detomo, Jr., L. Regner, and T. R. Donoghue, Phys. Rev. **C21**, 475 (1980).

[Eng88] S. Engstler, A. Krauss, K. Neldner, C. Rolfs, U. Schröder, and K. Langanke, Phys. Lett. **B202**, 179 (1988).

[Eng92] S. Engstler, G. Raimann, C. Angulo, U. Greife, C. Rolfs, U. Schröder, E. Somorjai, B. Kirch, and K. Langanke, Z. Phys. **A342**, 471 (1992).

[Fal95] M. Falvo, 1995, private communication.

[Fle92] K. A. Fletcher, Ph.D. thesis, Universtiy of North Carolina at Chapel Hill, 1992, Available from University Microfilms, Ann Arbor, Michigan.

[For98] Forssman, 1998. This are unpublished data contained in the input file.

[Fre54] G. Freier and H. Holmgren, Phys. Rev. **93**, 825 (1954).

[Gar69] D. Garreta, J. Sure, and A. Tarrats, Nucl. Phys. **A132**, 204 (1969).

[Gar74] R. Garrett and W. W. Lindstrom, Nucl. Phys. **A224**, 186 (1974).

[Gei95] W. Geist, Z. Ayer, A. C. Hird, H. J. Karwowski, and E. J. Ludwig, Nucl. Instr. Meth. **A365**, 36 (1995).

[Gei96] W. H. Geist, Z. Ayer, A. C. Hird, E. J. Ludwig, M. Wood, and K. A. Fletcher, Nucl. Instr. Meth. **B111**, 176 (1996).

[Gen] General Ionex, *Sputterbell Model 1080, Duoplasmatron Model 358.*

[Gol91] R. Golser and D. Semrad, Phys. Rev. Lett. **66**, 1831 (1991).

[Gre95] U. Greife, F. Gorris, M. Junker, C. Rolfs, and D. Zahnow, Z. Phys. **A351**, 107 (1995).

[Grü71a] W. Grüebler, V. König, A. Ruh, P. A. Schmelzbach, R. E. White, and P. Marmier, Nucl. Phys. **A176**, 631 (1971).

[Grü71b] W. Grüebler, V. König, A. Ruh, R. E. White, P. A. Schmelzbach, R. Risler, and P. Marmier, Nucl. Phys. **A165**, 505 (1971).

[Hal80] G. M. Hale and D. C. Dodder, in *Proc. Int. Conf. on Nucl. Cross Sections for Technology*, volume 594, page 650, Knoxville, 1979, 1980, NBS Special Publication.

[Hal87] G. M. Hale, R. E. Brown, and N. Jarmie, Phys. Rev. Lett. **59**, 763 (1987).

[Hal98] G. M. Hale, 1998, private communication.

[Har73] R. A. Hardekopf, D. D. Armstrong, W. Grüebler, P. W. Keaton, Jr., and U. Meyer-Berkhout, Phys. Rev. C **8**, 1629 (1973).

[Jah45] E. Jahnke and F. Emde, *Tables of Functions*, Dover, New York, 1945.

[Jun98] M. Junker, A. D'Alessandro, S. Zavatarelli, C. Arpesella, E. Bellotti, C. Broggini, P. Corvisiero, G. Fiorentini, A. Fubini, G. Gervino, U. Greife, C. Gustavino, J. Lambert, P. Prati, W. S. Rodney, C. Rolfs, F. Strieder, H. P. Trautvetter, and D. Zahnow, Phys. Rev. **C57**, 2700 (1998).

[Kli71] W. Klinger, F. Dusch, and R. Fleischmann, Nucl. Phys. **A166**, 253 (1971).

[Kön71] V. König, W. Grüebler, A. Ruh, R. E. White, P. A. Schmelzbach, R. Risler, and P. Marmier, Nucl. Phys. **A166**, 393 (1971).

[Kra71] L. Kraus, Ph.D. thesis, Université Louis Pasteur, Strasbourg, 1971, Thèse No. 681.

[Kra87] A. Krauss, H. W. Becker, H. P. Trautvetter, C. Rolfs, and K. Brand, Nucl. Phys. **A465**, 150 (1987).

[Kun55] W. E. Kunz, Phys. Rev. **97**, 456 (1955).

[Lan58] A. M. Lane and R. G. Thomas, Rev. Mod. Phys. **30**, 257 (1958).

[Lan92] K. Langanke and D. Lukas, Ann. Phys. **1**, 332 (1992).

[Lan96] K. Langanke, T. D. Shoppa, C. A. Barnes, and C. Rolfs, Phys. Lett. **369B**, 211 (1996).

[Lee71] C. Leemann, H. Bürgisser, P. Huber, U. Rohrer, H. P. gen. Schieck, and F. Seiler, Phys. Acta **44**, 141 (1971).

[Lud97] E. J. Ludwig, T. C. Black, C. R. Brune, W. H. Geist, and H. J. Karwowski, Nucl. Instr. Meth. **A388**, 37 (1997).

[Mad71] in *Proc. of the Third Int. Symp. on Polarization Phenomena in Nuclear Reactions*, edited by H. H. Barschall and W. Haeberli, page xxv, Madison, Wisconsin, 1971.

[McI67] L. C. McIntyre and W. Haeberli, Nucl. Phys. **A91**, 369 (1967).

[Men96] A. J. Mendez, C. D. Roper, J. D. Dunham, and T. B. Clegg, Rev. Sci. Instrum. **67**, 3073 (1996).

[Mil88] G. H. Miley, Nucl. Instr. Meth. **A271**, 197 (1988).

[Möl80] W. Möller and F. Besenbacher, Nucl. Instr. Meth. **168**, 111 (1980).

[Mom88] H. Momota, M. Okamato, Y. Nomura, M. Ohnishi, H. L. Berk, and T. Tajima, Nucl. Instr. Meth. **A271**, 7 (1988).

[Ohl73] G. G. Ohlsen and P. W. Keaton, Jr., Nucl. Instr. Meth. **109**, 41 (1973).

[Ohl98] Ohlsen, 1998. This are unpublished data contained in the input file taken in 1971.

[Pla72] G. R. Plattner, A. D. Bacher, and H. E. Conzett, Phys. Rev. **C5**, 1158 (1972).

[Pra94] P. Prati, C. Arpesella, F. Bartolucci, H. W. Becker, E. Bellotti, C. Broggini, P. Corvisiero, G. Fiorentini, A. Fubini, G. Gervino, F. Gorris, U. Greife, C. Gustavino, M. Junker, C. Rolfs, W. H. Schulte, H. P. Trautvetter, and D. Zahnow, Z. Phys. **A350**, 171 (1994).

[Ric95] B. Ricci, S. Degl'Innocenti, and G. Fiorentini, Phys. Rev. **C52**, 1095 (1995).

[Roh71] U. Rohrer, P. Huber, C. Leemann, H. Meiner, and F. Seiler, Phys. Acta **44**, 846 (1971).

[Rol95] C. Rolfs and E. Somorjai, Nucl. Instr. Meth. **B99**, 297 (1995).

[San96] F. D. Santos, 1996, private communication.

[Sch76] P. A. Schmelzbach, W. Grüebler, V. König, R. Risler, D. O. Boerma, and B. Jenny, Nucl. Phys. **A264**, 45 (1976).

[Sch83] B. M. Scherzer, in *Sputtering by Particle Bombardment II*, edited by R. Behrisch, page 271, Springer, Heidelberg, 1983.

[Sei70] F. Seiler and E. Baumgartner, Nucl. Phys. **A153**, 193 (1970).

[Sho93] T. D. Shoppa, S. E. Koonin, K. Langanke, and R. Seki, Phys. Rev. **C48**, 837 (1993).

[Sig81] P. Sigmund, in *Sputtering by Particle Bombardment I*, edited by R. Behrisch, page 9, Springer, Heidelberg, 1981.

[Smi93] M. S. Smith, L. H. Kawano, and R. A. Malaney, Astrophys. J., Suppl. Ser. **85**, 219 (1993).

[Til98] D. R. Tilley, C. M. Cheves, and G. M. Hale, 1998, to be submitted to Nucl. Phys. **A**.

[Ton81] T. A. Tonsfeldt, Ph.D. thesis, University of North Carolina at Chapel Hill, 1981, Available from University Microfilms, Ann Arbor, Michigan, order #8022515.

[Yar53] J. L. Yarnell, R. H. Lovberg, and W. R. Stratton, Phys. Rev. **90**, 292 (1953).